UNIVERSITY OF CALIFORNIA
RIVERSIDE

Transverse Single-spin Asymmetry for Diffractive Electromagnetic Jets at Forward Rapidity using $p^{\uparrow} + p$ Collisions at $\sqrt{s} = 200$ and 510 GeV at STAR

A Dissertation submitted in partial satisfaction
of the requirements for the degree of

Doctor of Philosophy

in

Physics

by

Xilin Liang

September 2025

Dissertation Committee:
Professor Kenneth Barish, Chairperson
Professor Richard Seto
Professor Miguel Arratia

The Dissertation of Xilin Liang is approved:

Committee Chairperson

University of California, Riverside

Acknowledgments

First of all, I am grateful to my advisor, Prof. Kenneth Barish. He supported me in my seven-year graduate study. He encouraged me to try out various ideas to complete the analysis. Additionally, he was willing to provide me with opportunities to present my studies to audiences in high-energy physics / nuclear physics, and interact with experts. Without his support, I would not be able to complete the analysis myself. Then, I would like to thank all the UCR Spin and Heavy Ion group members including: Prof. Richard Seto, Dr. Latif Kabir, Dr. Bishnu Karki, Dr. Weibin Zhang, Dr. David Kapukchyan, Dr. Cameron Racz, Ding Chen, Erik Loyd, Ananya Paul, Borna Maghoul (Kumar), Michael Gordon, and other previous group members. During the weekly group meetings, I received plenty of comments and suggestions for my studies.

Related to my dissertation analysis, I would like to thank all the PAs for the upcoming published papers on this analysis: Dr. Carl Gagliardi, Dr. Kenneth Barish, Dr. Latif Kabir, Dr. David Kapukchyan, Dr. Mriganka Mondal, and Dr. Christopher Dilks. Without their help, it would have been challenging to complete the analysis and process the paper for publication. Especially, I appreciate Dr. Carl Gagliardi, who is always willing to provide ideas for my analysis. Additionally, I would like to thank all the STAR cold QCD physics working group members for their support of my dissertation analysis and for providing valuable comments and suggestions. Furthermore, I would like to thank the STAR Roman Pot team experts who provided instructions and suggestions regarding the simulation and data analysis using the Roman Pot detectors. During my graduate study at the STAR experiment, I would like to thank the STAR Forward Upgrade team,

especially Dr. Elke Aschenauer, Dr. Akio Ogawa, Dr. Oleg Tsai, and Dr. Oleg Eyser, for providing numerous comments and suggestions on the π^0 reconstruction study for the FCS. Lastly, I would like to thank Dr. Miguel Arratia and his group. They provide me with several opportunities to work on the EIC detector simulation study and prototype detector experiments. With the help of experts and students, I have completed my graduate studies, gaining a deeper understanding of high-energy physics and nuclear physics.

Since most of my graduate studies were conducted at Brookhaven National Laboratory, I would like to thank all the faculty, postdoctoral researchers, and visitors I met there. Additionally, I would like to thank my roommates as well. We shared fun and they helped me a lot during my visit to Long Island.

Last but not least, I would like to express my sincere appreciation to my parents, Xiaoyong Liang and Fufen Zhou. They have supported me during my graduate study in the United States. Without their support and encouragement, I would not be able to complete the study successfully.

ABSTRACT OF THE DISSERTATION

Transverse Single-spin Asymmetry for Diffractive Electromagnetic Jets at Forward Rapidity using $p^{\uparrow} + p$ Collisions at $\sqrt{s} = 200$ and 510 GeV at STAR

by

Xilin Liang

Doctor of Philosophy, Graduate Program in Physics
University of California, Riverside, September 2025
Professor Kenneth Barish, Chairperson

Transverse single-spin asymmetry, denoted as A_N, is the azimuthal asymmetry for final-state productions with respect to the polarized beam direction and the momentum direction. In polarized proton-proton collisions, the A_N is considered a powerful observable in proton spin structure studies. Initially, the A_N is predicted to be small. However, more experiments show the unexpectedly large A_N in proton-proton collisions, which raises great interest in understanding the origin of the large A_N. Recent studies indicate that the large A_N might originate from diffractive events, which motivates this study to explore the A_N for diffractive events in polarized proton-proton collisions and to investigate their contributions to the large A_N observed in inclusive events.

The Relativistic Heavy Ion Collider (RHIC) is the only collider capable of providing polarized proton beams. The Solenoidal Tracker at RHIC (STAR) experiment takes advantage of RHIC and provides ideal opportunities to study the A_N for diffractive events. Two transversely polarized proton-proton collision datasets taken in 2015 and 2017, with the center-of-mass energies of 200 GeV and 510 GeV, respectively, are used for this study.

In this dissertation, the A_N for electromagnetic jets (EM-jets) in single diffractive events, rapidity gap events, and semi-exclusive events are studied. The A_N for single diffractive events and rapidity gap events is explored as a function of Feynman-x (x_F) and as a function of photon multiplicity (the number of photons inside the EM-jet) for the two datasets. It shows that the A_N for single diffractive events and rapidity gap events are consistent with the A_N for inclusive events within uncertainty. The fraction of the cross-section in single diffractive events to inclusive events is studied. These provide essential information on the contributions for the A_N in single diffractive events to the large A_N observed in inclusive events. The A_N for semi-exclusive events is also studied for the 200 GeV dataset. These interesting results provide evidence to understand the origin of the large A_N.

Contents

List of Figures **x**

List of Tables **xvii**

1 Introduction **1**
1.1 Proton Structure . . . 1
1.1.1 History of Proton Structure . . . 1
1.1.2 Proton Spin Puzzle . . . 4
1.2 Transverse Single-spin Asymmetry . . . 5
1.2.1 Transverse Momentum Dependent Factorization framework (TMD) . . . 7
1.2.2 Higher-Twist Collinear Factorization framework (Twist-3) . . . 11
1.3 Diffractive Processes . . . 12
1.3.1 Physics for diffractive processes . . . 12
1.3.2 Indication of large TSSA originating from the diffractive processes . . . 14
1.4 Structure of this dissertation . . . 17

2 Experiment **18**
2.1 Relativistic Heavy Ion Collider (RHIC) . . . 18
2.2 The STAR Experiment . . . 22
2.2.1 Forward Meson Spectrometer (FMS) . . . 24
2.2.2 Roman Pot (RP) . . . 27
2.2.3 Beam-Beam Counter (BBC) . . . 29
2.3 Dataset . . . 30
2.3.1 Information for the Dataset . . . 30
2.3.2 Quality Assurance . . . 31

3 Transverse Single-spin Asymmetry for Single Diffractive Events **34**
3.1 Event Selection . . . 34
3.1.1 Event Property Cuts . . . 35
3.1.2 EM-jet Reconstruction . . . 36
3.1.3 BBC East Veto Cuts . . . 41
3.1.4 East Roman Pot (RP) Track Cuts . . . 44
3.2 Background Study . . . 49

3.3 Cross-ratio Method . . . 51
3.4 Systematic Uncertainty . . . 54
3.4.1 Systematic uncertainty for the BBC East veto cuts . . . 55
3.4.2 Ring of Fire . . . 56
3.4.3 Polarization Uncertainty . . . 57
3.5 Cross-section Fraction Study . . . 59
3.6 Transverse Single-spin Asymmetry for Single Diffractive Events in $\sqrt{s} = 200$ GeV and 510 GeV . . . 63

4 Transverse Single-spin Asymmetry for Rapidity Gap Events 69
4.1 Introduction . . . 69
4.2 Single Diffractive Fraction in the Rapidity Gap Events . . . 70
4.3 Results . . . 72
4.3.1 Transverse Single-spin Asymmetry for Rapidity Gap Events in $\sqrt{s} =$ 200 GeV and 510 GeV . . . 72
4.3.2 Direct Comparison among Inclusive Events, Rapidity Gap Events, and Single Diffractive Events . . . 77

5 Transverse Single-spin Asymmetry for Semi-exclusive Events 80
5.1 Event Selection . . . 80
5.1.1 Event Property and EM-jet Reconstruction . . . 81
5.1.2 BBC West Veto Cuts . . . 82
5.1.3 West Roman Pot (RP) Track Cuts . . . 86
5.1.4 Energy Sum Cut . . . 95
5.2 Background Study . . . 97
5.3 Systematic Uncertainty Study . . . 102
5.3.1 Systematic Uncertainty for the BBC West Veto cuts . . . 103
5.3.2 Systematic Uncertainty for the Energy Sum cut . . . 104
5.4 Transverse Single-spin Asymmetry for Semi-exclusive Events in $\sqrt{s} = 200$ GeV 104

6 Conclusions and Outlook 106

Bibliography 109

A π^0 Reconstruction for STAR Forward Upgrade Electromagnetic Calorimeter 116
A.1 Introduction . . . 116
A.2 Gain Factor Study for the Prototype FCS ECal . . . 117
A.3 Calibration for the Full FCS ECal . . . 119

List of Figures

1.1 Evolution of proton internal (spin) structure. (a) Proton internal (spin) structure from the quark model. (b) Modern proton internal (spin) structure, which includes the valence quarks, sea quarks, and gluons. 3

1.2 Transverse single-spin asymmetry for charged- and neutral-pions at different center-of-mass energies as a function of x_F. 6

1.3 The leading-order of the TMD PDFs for quarks, classified according to the polarizations of the quark and the polarization of the nucleon. 8

1.4 A schematic picture showing the Sivers effect in proton-proton collision. . . 9

1.5 A schematic picture showing the Collins effect in proton-proton collision. . . 10

1.6 Left panel: The diffractive pattern of light on a circular obstacle in wave optics. Right panel: The diffractive cross-section in high-energy scattering. The solid line shows the elastic differential cross-section, while the dashed line shows the differential cross-section for the situation where either the projectile or the target breaks up. The elastic cross-section is analogous to the diffractive pattern in the left panel if identifying $|t| \approx k^2\theta^2$ 13

1.7 Schematic diagrams of (a) single diffractive process and (b) double diffractive process. 14

1.8 Transverse single-spin asymmetry for inclusive π^0 at forward rapidity using $p^\uparrow + p$ collisions at $\sqrt{s} = 200$ and 500 GeV at STAR. The isolated π^0 A_N are shown in solid points, while the non-isolated π^0 A_N are shown in empty points. 15

1.9 Transverse single-spin asymmetry for inclusive EM-jets at forward rapidity using $p^\uparrow + p$ collisions at $\sqrt{s} = 200$ GeV at STAR. Three cases of photon multiplicity (n_γ) are mentioned for extracting A_N: $n_\gamma = 1, 2$, $n_\gamma = 3$, $n_\gamma = 4, 5$. 16

2.1 The general layout of the RHIC facility, focusing on the polarized proton operation. 19

2.2 The setup for RHIC pC-polarimeter. 22

2.3 Schematic layout of RHIC H-jet polarimeter. 23

2.4 Schematic layout of the major STAR detectors in 2017. The abbreviations of the STAR sub-detectors are explained in the main contents. 24

2.5 The schematic layout of the FMS. All the cells are displayed in the cartoon. The green lines split the FMS small cell region and the FMS large cell region. 25

2.6 (Top) The schematic layout of the STAR RP system (not to scale). The blue points indicate the two RP stations on the west side of STAR, and the yellow points indicate the two RP stations on the east side of STAR. (Bottom) The schematic layout for displaying RP stations on the side view. Each RP station consists of two RP vessels, housing four SSD planes (represented by black solid lines) and one scintillation counter (represented by a green solid box). 28

2.7 Schematic layout for BBC detector on the front view. The tiles in the large BBC region are shown in red, while the tiles in the small BBC region are shown in grey. 30

2.8 Example of the EM-jet distribution for an entire fill. The numbers are the FMS cell ID. The left plot shows the distribution before the additional hot channel masking. The red spots are considered the hot channels, which are manually masked out. The right plot shows the distribution after the additional hot channel masking. The red spots are mostly gone, and the EM-jet distribution is closer to evenly distributed. 33

3.1 A schematic cartoon describing the single diffractive events used for this analysis. 35

3.2 Quality insurance plots for EM-jet after the EM-jet reconstruction and p_T cuts for the Run 15 dataset. The left plot is the number of EM-jets in each event. The right plot is the EM-jet p_T vs energy distribution. 38

3.3 Quality insurance plots for EM-jet after the EM-jet reconstruction and p_T cuts for the Run 17 dataset. The left plot is the number of EM-jets in each event. The right plot is the EM-jet p_T vs energy distribution. 39

3.4 The schematic cartoon for the Underlying Event contribution estimation using the off-axis cone method. 40

3.5 (left) The 2D plot for the distribution of particle-level FMS EM-jet energy vs the matched detector-level EM-jet energy in the simulation. (right) The 2D profile plot between the EM-jet energy at the detector level and the particle level, with polynomial fits. 41

3.6 East RP θ_X and θ_Y distributions for three different East RP track ξ ranges ($0 < \xi < 0.05$ (left); $0.05 < \xi < 0.1$ (middle); $0.1 < \xi < 0.15$ (right)) with only applying BBC East ADC sum < 150. 43

3.7 The small (left) and large (right) BBC East ADC sum distribution after the rough East RP θ_X and θ_Y cuts for the Run 15 dataset. 43

3.8 The small BBC East ADC sum distribution (left) and the large BBC East earliest TDC distribution (right) after the rough East RP θ_X and θ_Y cuts for the Run 17 dataset. 44

3.9 East RP track θ_X and θ_Y distributions for three East RP track ξ ranges ($0 < \xi < 0.05$ (left); $0.05 < \xi < 0.1$ (middle); $0.1 < \xi < 0.15$ (right)) for the Run 15 dataset. 46

3.10 East RP track p_X and p_Y distributions for three East RP track ξ ranges ($0 < \xi < 0.05$ (left); $0.05 < \xi < 0.1$ (middle); $0.1 < \xi < 0.15$ (right)) for the Run 15 dataset. The black curves indicate the ranges of accepted East RP track p_X and p_Y cuts. 46

3.11 East RP track θ_X and θ_Y distributions for three East RP track ξ ranges ($0 < \xi < 0.05$ (left); $0.05 < \xi < 0.1$ (middle); $0.1 < \xi < 0.15$ (right)) for the Run 17 dataset. 48

3.12 East RP track p_X and p_Y distributions for three East RP track ξ ranges ($0 < \xi < 0.05$ (left); $0.05 < \xi < 0.1$ (middle); $0.1 < \xi < 0.15$ (right)) for the Run 17 dataset. The black curves indicate the ranges of accepted East RP track p_X and p_Y cuts. 48

3.13 Schematic diagram for defining the x- and y-coordinates (left), as well as the ϕ regions (right) with respect to two different polarized proton beam directions: blue beam (blue color) and yellow beam (yellow color). 52

3.14 Example of the raw asymmetry extraction with the cosine fit. It is the fit for calculating the raw asymmetry for single diffractive EM-jet A_N with all photon multiplicity at the EM-jet $0.25 < x_F < 0.30$. 53

3.15 χ^2 distribution for all the fits with Run 15 dataset (left) and with Run 17 dataset (right). The χ^2 probability distribution with degrees of freedom equal to 6 is also shown in the curve. 54

3.16 Cross-section fraction of the single diffractive process (σ_{SD}) to the inclusive process (σ_{inc}) as a function of x_F for the Run 15 dataset. 62

3.17 Transverse single-spin asymmetry for single diffractive events as a function of x_F with $p^{\uparrow} + p$ collisions at $\sqrt{s} = 200$ GeV for three different photon multiplicity cases: all photon multiplicity (top), one- or two-photon multiplicity (middle), and three- or more-photon multiplicity (bottom). The A_N for $x_F > 0$ are shown in blue points. The A_N for $x_F < 0$ (red points) shifts -0.013 along the x-axis. 64

3.18 Transverse single-spin asymmetry for single diffractive events as a function of x_F with $p^{\uparrow} + p$ collisions at $\sqrt{s} = 510$ GeV for three different photon multiplicity cases: all photon multiplicity (top), one- or two-photon multiplicity (middle), and three- or more-photon multiplicity (bottom). The A_N for $x_F > 0$ are shown in blue points. The A_N for $x_F < 0$ (red points) shifts -0.013 along the x-axis. 66

3.19 Comparison for the single diffractive EM-jet A_N for $\sqrt{s} = 200$ GeV (brown) and 510 GeV (blue). The single diffractive EM-jet A_N for $\sqrt{s} = 200$ GeV (brown points) shifts -0.013 along the x-axis. 68

4.1 A schematic cartoon describing the rapidity gap event used for this analysis. 70

4.2 A_N for the EM-jet of rapidity gap events as a function of x_F using $p^{\uparrow} + p$ at $\sqrt{s} = 200$ GeV dataset for three different photon multiplicity cases: all photon multiplicity (top), one- or two-photon multiplicity (middle), and three- or more-photon multiplicity (bottom). The A_N for $x_F < 0$ (red points) shifts -0.013 along the x-axis. 74

4.3 A_N for the EM-jet of rapidity gap events as a function of x_F $p^{\uparrow} + p$ at $\sqrt{s} = 510$ GeV for three different photon multiplicity cases: all photon multiplicity (top), one- or two-photon multiplicity (middle), and three- or more-photon multiplicity (bottom). The A_N for $x_F < 0$ (red points) shifts -0.013 along the x-axis. 75

4.4 Comparison for the rapidity gap event EM-jet A_N for $\sqrt{s} = 200$ GeV (brown) and 510 GeV (blue). The rapidity gap event EM-jet A_N for $\sqrt{s} = 200$ GeV (brown points) shifts -0.013 along the x-axis. 76

4.5 A_N for inclusive events (red), rapidity gap events (purple), and single diffractive events (blue) as a function of x_F in $p^{\uparrow} + p$ at $\sqrt{s} = 200$ GeV for one- or two-photon multiplicity case (top panel) and three- or more-photon multiplicity (bottom panel). The A_N for single diffractive process shifts -0.008 along the x-axis, and the A_N for rapidity gap events shifts +0.008 along the x-axis. 78

4.6 A_N for inclusive events (red), rapidity gap events (purple), and single diffractive events (blue) as a function of x_F in $p^{\uparrow} + p$ at $\sqrt{s} = 510$ GeV for one- or two-photon multiplicity case (top panel) and three- or more-photon multiplicity (bottom panel). The A_N for single diffractive process shifts -0.008 along the x-axis, and the A_N for rapidity gap events shifts +0.008 along the x-axis. 79

5.1 A schematic cartoon describing the semi-exclusive event used for this analysis. 81

5.2 West RP θ_X and θ_Y distributions for nine different west RP track ξ ranges ($0 < \xi < 0.05$ (top left); $0.05 < \xi < 0.1$ (top middle); $0.1 < \xi < 0.15$ (top right); $0.15 < \xi < 0.2$ (middle left); $0.2 < \xi < 0.25$ (middle middle); $0.25 < \xi < 0.3$ (middle right); $0.3 < \xi < 0.35$ (bottom left); $0.35 < \xi < 0.4$ (bottom middle); $0.4 < \xi < 0.45$ (bottom right)) with only applying small BBC West ADC sum < 150 for the Run 15 dataset. 84

5.3 Small BBC west ADC sum distribution (left) and large BBC west ADC sum distribution (right) after the rough west RP cuts for the Run 15 dataset. . . 84

5.4 Small BBC west ADC sum distribution (left) and large BBC west earliest TDC distribution (right) after the rough west RP cuts for the Run 17 dataset. 86

5.5 West RP θ_X and θ_Y distributions after the BBC west veto cuts for nine different west RP track ξ ranges ($0 < \xi < 0.05$ (top left); $0.05 < \xi < 0.1$ (top middle); $0.1 < \xi < 0.15$ (top right); $0.15 < \xi < 0.2$ (middle left); $0.2 < \xi < 0.25$ (middle middle); $0.25 < \xi < 0.3$ (middle right); $0.3 < \xi < 0.35$ (bottom left); $0.35 < \xi < 0.4$ (bottom middle); $0.4 < \xi < 0.45$ (bottom right)) for the Run 15 dataset. 87

5.6 West RP track p_X and p_Y distributions for nine west RP track ξ ranges ($0 < \xi < 0.05$ (top left); $0.05 < \xi < 0.1$ (top middle); $0.1 < \xi < 0.15$ (top right); $0.15 < \xi < 0.2$ (middle left); $0.2 < \xi < 0.25$ (middle middle); $0.25 < \xi < 0.3$ (middle right); $0.3 < \xi < 0.35$ (bottom left); $0.35 < \xi < 0.4$ (bottom middle); $0.4 < \xi < 0.45$ (bottom right)) for the Run 15 dataset. The black curves indicate the ranges of accepted west RP track p_X and p_Y cuts. 89

5.7 West RP θ_X and θ_Y distributions after the BBC west veto cuts for nine different west RP track ξ ranges ($0 < \xi < 0.05$ (top left); $0.05 < \xi < 0.1$ (top middle); $0.1 < \xi < 0.15$ (top right); $0.15 < \xi < 0.2$ (middle left); $0.2 < \xi < 0.25$ (middle middle); $0.25 < \xi < 0.3$ (middle right); $0.3 < \xi < 0.35$ (bottom left); $0.35 < \xi < 0.4$ (bottom middle); $0.4 < \xi < 0.45$ (bottom right)) for the Run 17 dataset. 91

5.8 West RP track p_X and p_Y distributions for nine west RP track ξ ranges ($0 < \xi < 0.05$ (top left); $0.05 < \xi < 0.1$ (top middle); $0.1 < \xi < 0.15$ (top right); $0.15 < \xi < 0.2$ (middle left); $0.2 < \xi < 0.25$ (middle middle); $0.25 < \xi < 0.3$ (middle right); $0.3 < \xi < 0.35$ (bottom left); $0.35 < \xi < 0.4$ (bottom middle); $0.4 < \xi < 0.45$ (bottom right)) for the Run 17 dataset. The black curves indicate the ranges of accepted west RP track p_X and p_Y cuts. 93

5.9 Energy sum distributions for five EM-jet x_F regions ($0.2 < x_F < 0.25$ (top left); $0.25 < x_F < 0.3$ (top right); $0.3 < x_F < 0.35$ (bottom left); $0.35 < x_F < 0.4$ (bottom middle); $0.4 < x_F < 0.45$ (bottom right)) for the Run 15 dataset. 96

5.10 Energy sum distributions for six EM-jet x_F regions ($0.1 < x_F < 0.15$ (top left); $0.15 < x_F < 0.2$ (top middle); $0.2 < x_F < 0.25$ (top right); $0.25 < x_F < 0.3$ (bottom left); $0.3 < x_F < 0.35$ (bottom middle); $0.35 < x_F < 0.4$ (bottom right)) for the Run 17 dataset. 97

5.11 Example for mixed event energy sum background distribution for EM-jet with $0.2 < x_F < 0.25$ in the Run 15 dataset. 99

5.12 Mixed event energy sum background study results for each EM-jet x_F regions ($0.2 < x_F < 0.25$ (top left); $0.25 < x_F < 0.3$ (top right); $0.3 < x_F < 0.35$ (bottom left); $0.35 < x_F < 0.4$ (bottom middle); $0.4 < x_F < 0.45$ (bottom right)) for the Run 15 dataset. 100

5.13 Mixed event energy sum background study results for six EM-jet x_F regions ($0.1 < x_F < 0.15$ (top left); $0.15 < x_F < 0.2$ (top middle); $0.2 < x_F < 0.25$ (top right); $0.25 < x_F < 0.3$ (bottom left); $0.3 < x_F < 0.35$ (bottom middle); $0.35 < x_F < 0.4$ (bottom right)) for the Run 17 dataset. 101

5.14 A_N for semi-exclusive events with one- or two-photon multiplicity EM-jets as a function of x_F in $p^{\uparrow} + p$ collisions at $\sqrt{s} = 200$ GeV. The blue points are for $x_F > 0$, while the red points are for $x_F < 0$, with shifting -0.005 along the x-axis. 105

A.1 Invariant mass plot for the data taken with the prototype FCS ECal. The vertical red line indicates the position of the π^0 invariant mass. 119

A.2 Example of the tower invariant mass spectrum. The black points are the invariant mass spectrum. The magenta curve is the fit for the signal peak. The blue curve is the fit for the background. The red curve is the overall fit. 121

A.3 Example of the invariant mass peak status plot for the north side FCS ECal tower before the π^0 reconstruction iteration (left) and after the π^0 reconstruction iteration for two iterations (right). 123

A.4 Invariant mass plot before π^0 reconstruction iteration (left) and after (right) π^0 reconstruction iteration for two iterations. 123

List of Tables

2.1 FMS trigger threshold for the major triggers used in this analysis. Some of the trigger thresholds were adjusted during the RHIC proton-proton collision period. Therefore, multiple trigger threshold values were shown for those triggers. 27

3.1 Four acceptable 4-bit spin patterns 36

3.2 Final cuts for East RP track θ_X by three ξ regions for the Run 15 dataset. 46

3.3 East RP track p_X and p_Y final cuts for the Run 15 dataset 47

3.4 Final cuts for East RP track θ_X by three ξ regions for the Run 17 dataset. 48

3.5 East RP track p_X and p_Y final cuts for the Run 17 dataset. 49

3.6 n-σ significant for each photon multiplicity case for $x_F > 0$ for single diffractive events in $\sqrt{s} = 200$ GeV 65

3.7 n-σ significant for each photon multiplicity case for $x_F > 0$ for single diffractive events in $\sqrt{s} = 510$ GeV 65

5.1 Rough west RP θ_X cuts with ξ dependent for the Run 15 dataset. 85

5.2 Final west RP θ_X cuts for the Run 15 dataset 88

5.3 Final west RP p_X and p_Y cuts for each west RP ξ region of the Run 15 dataset. 90

5.4 Final west RP θ_X cuts for the Run 17 dataset 92

5.5 Final west RP p_X and p_Y cuts for each west RP ξ region of the Run 17 dataset. 94

5.6 Energy sum cuts for semi-exclusive process for five EM-jet x_F regions for the Run 15 dataset. 96

5.7 Energy sum cuts for semi-exclusive process for six EM-jet x_F regions for the Run 17 dataset. 98

5.8 Fraction of the accidental coincidence events (background) for each EM-jet x_F region for the Run 15 dataset. 101

5.9 Fraction of the accidental coincidence events (background) for each EM-jet x_F region for the Run 17 dataset. 102

5.10 Energy sum cuts for semi-exclusive events in studying the systematic uncertainty for the Run 15 dataset. 104

Chapter 1

Introduction

1.1 Proton Structure

1.1.1 History of Proton Structure

Over the past few decades, scientists have been trying to answer an ambitious question: what the world is made of. In 1803, J. Dalton proposed that all elements are composed of small indivisible particles called atoms. The atoms are identical and cannot be created or destroyed. This notion was later revised following J. J. Thomson's cathode ray experiments in the late 19th century showed the existence of the electron, a particle significantly lighter than the lightest known atom. This discovery implied that atoms possess internal structure. Thomson introduced the "plum pudding" model, describing the atom as a positively charged sphere with electrons embedded throughout. Soon, in 1909, the famous gold foil experiment conducted by Rutherford's group showed that most alpha particles passed straight through the foil, but only a small fraction were deflected or bounced. These observations led to the nuclear model of the atom: a dense, positively charged nucleus

occupies the center, with electrons surrounding at relatively large distances. Later, in 1920, Rutherford named the hydrogen nucleus a "proton". With the discovery of neutrons in 1932, it became clear that the proton, neutron, and electron were the fundamental building blocks that form the atom [1, 2].

In the mid-20th century, an increasing number of particles were discovered. These particles can be categorized into two groups: hadrons and leptons. Hadrons participate in the strong interaction and are further classified into two families: baryons, which are fermions, and mesons, which are bosons. Hadrons process spin quantum number of $J = n(\hbar/2)$, where n is an odd number for a Fermion and an even number for a boson. The proton is a fermion with spin $J = \hbar/2$. Leptons do not undergo strong interactions and instead interact only via the weak force, as well as the electromagnetic force if they are charged. The electron, mentioned above, belongs to the lepton [1, 2].

In 1964, the quark model was proposed by Murray Gell-Mann and George Zweig independently [3, 4]. In this model, quarks are assumed to be the constituents of hadrons. The baryon is the bound state of three quarks, while mesons are composed of a quark and anti-quark pair. The quark model was considered a valid and effective classification of hadrons during the 1960s. Figure 1.1 (a) shows the schematic cartoon of the proton structure based on the quark model. The proton is a bound state of two up quarks and one down quark. The up quark carries $+\frac{2}{3}e$ charge and the down quark carries $-\frac{1}{3}e$ charge, where e is the charge equal to the elementary charge. Both kinds of quarks have spin $\frac{1}{2}$, but their spins are aligned in opposite directions. Therefore, they make up the proton with a total spin of $\frac{1}{2}$ and charge of $+1e$ [3].

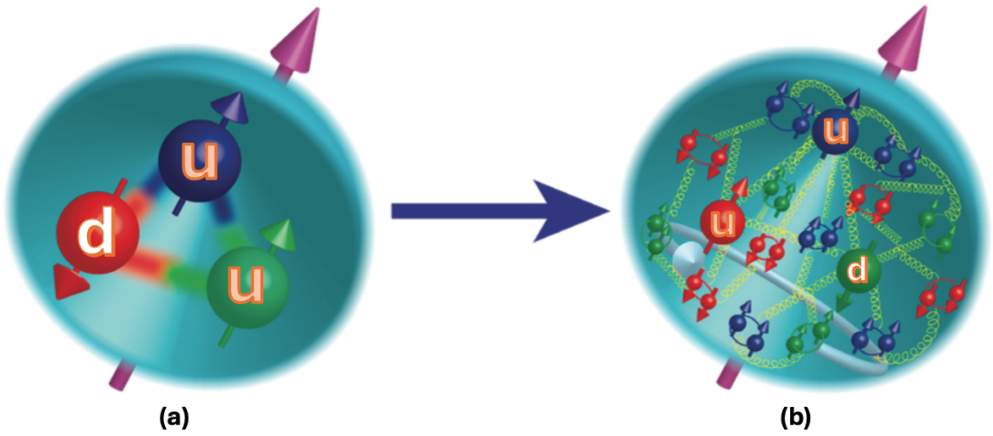

Figure 1.1: Evolution of proton internal (spin) structure. (a) Proton internal (spin) structure from the quark model. (b) Modern proton internal (spin) structure, which includes the valence quarks, sea quarks, and gluons.

In the late 1960s, deep inelastic scattering (DIS) experiments performed at the Stanford Linear Accelerator Center (SLAC) demonstrated that the proton is not fundamental. Since then, further experiments have investigated such substructures of protons and confirmed that quarks are the constituents of the proton, thereby proving the existence of quarks. Moreover, DIS data indicated that, in addition to the three valence quarks (two up quarks and one down quark), the proton also contains a dynamic "sea" of quark–antiquark pairs [5]. At the same time, the Quantum Chromodynamics (QCD) theory was raised [6, 7]. QCD describes the interactions of quarks mediated by the exchange of massless gauge bosons, known as gluons. Within this framework, the proton internal structure consists of three valence quarks, a sea of quark–antiquark pairs, and gluons, as illustrated schematically in Fig. 1.1(b). The quark and antiquark pairs can annihilate into gluons, while gluons can in turn generate new quark–antiquark pairs. Such a picture is generally considered a parton model of the proton [8].

The parton model is a conceptual framework to describe the internal structure of hadrons, including protons, in high-energy interactions. In DIS experiments, it serves as an intuitive way to understand the distribution of the quarks and gluons. The functions that describe the distribution of partons are called the parton distribution functions (PDFs). PDFs quantify the probability of finding the parton in a hadron as a function of the parton momentum fraction (x) of the proton at a fixed energy scale (Q^2). The quark and gluon PDFs are required to satisfy specific flavor and momentum sum rules:

$$\Sigma \int x f_a(x, Q^2) dx = 1 \tag{1.1}$$

where f_a is the PDFs of quarks and gluons, and $a = g, u, \bar{u}, d, \bar{d}, s, \bar{s}$ [9]. Studying the quark and gluon PDFs allows us to understand the internal structure of hadrons.

1.1.2 Proton Spin Puzzle

The proton, a spin-$\frac{1}{2}$ particle, was initially thought to derive its spin entirely from the three valence quarks, as illustrated in Fig. 1.1(a). However, in 1988, the European Muon Collaboration (EMC) performed a deep inelastic scattering experiment to determine how the proton's spin was distributed among its quark constituents. The results revealed that quarks account for only about 30% of the total spin [10]. This surprising result, known as the "proton spin puzzle", has since motivated extensive experimental and theoretical efforts to understand the origin of the proton's spin.

One theoretical framework proposed to resolve the proton spin puzzle is the Jaffe–Manohar sum rule [11], shown in Eq. 1.2,

$$\frac{1}{2} = \frac{1}{2}\Delta\Sigma + \Delta G + L_q + L_g \tag{1.2}$$

where the proton spin arises from four major contributions: quarks ($\frac{1}{2}\Delta\Sigma$), gluons (ΔG), and the orbital angular momentum from quarks (L_q) and gluons (L_g). Current studies focus on quantifying the quark and gluon spin terms, $\frac{1}{2}\Delta\Sigma$ and ΔG terms. In particular, the longitudinal spin program at the Relativistic Heavy Ion Collider (RHIC) has provided crucial experimental constraints on the quark and gluon contributions through polarized proton–proton collisions [12, 13], in connection with the theoretical studies [14]. However, the contributions from the orbital angular momentum of quarks and gluons are poorly understood and require further investigation through experiments. Transverse spin physics offers a potential avenue to probe orbital angular momentum contributions [15], making it an essential component in the broader effort to resolve the origin of the proton's spin.

1.2 Transverse Single-spin Asymmetry

In transverse spin physics, one of the key observables is the transverse single-spin asymmetry, commonly denoted as TSSA or A_N. It quantifies the azimuthal asymmetry of the final state productions with respect to the polarized beam direction and its momentum direction in the polarized scattering experiments. Measurements on the A_N can be performed in various experiments, including Deep Inelastic Scattering, proton-proton collisions, and proton-nucleon collisions, associated with different underlying processes. The general formula can be written in Eq. 1.3,

$$A_N = \frac{\sigma^{\uparrow} - \sigma^{\downarrow}}{\sigma^{\uparrow} + \sigma^{\downarrow}} \tag{1.3}$$

where $\sigma^{\uparrow(\downarrow)}$ refers to the cross section of two different spin states.

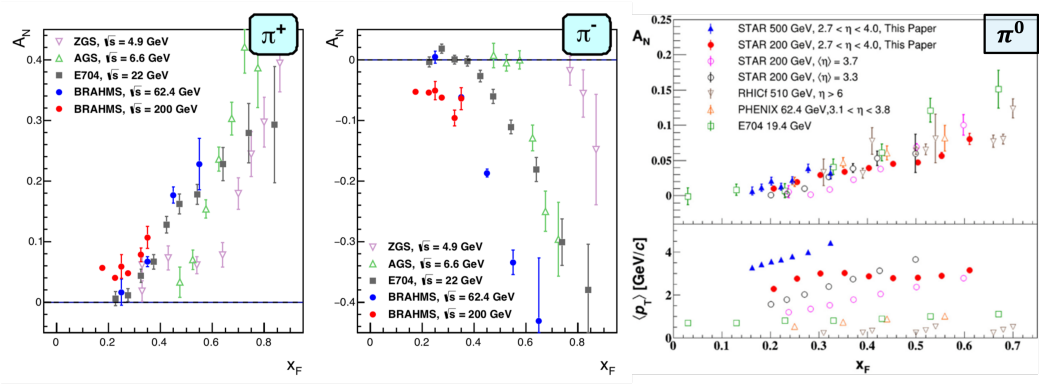

Figure 1.2: Transverse single-spin asymmetry for charged- and neutral-pions at different center-of-mass energies as a function of x_F.

Initially, the TSSA was predicted to be close to zero according to the perturbative Quantum Chromodynamics theory (pQCD) [16]. However, unexpectedly large TSSAs were observed in various experiments with different kinds of final-state productions at different center-of-mass energies ($\sqrt{s}$). The first experiment to observe the large TSSA value is the inclusive pion production in polarized proton-proton collisions at $\sqrt{s} = 6$ and 11.8 GeV at Argonne Zero-Gradient Synchrotron [17].

Furthermore, various experiments are being performed to measure the TSSA in charged- and neutral-hadron productions more precisely. They include the measurements of TSSA in charged- and neutral-pion productions at Fermi National Accelerator Laboratory (FNAL) and RHIC [17, 18, 19, 20, 21, 22]. Figure 1.2 shows the TSSA for π^+, π^- and π^0 in proton-proton collisions in different experiments with $\sqrt{s}$ over very wide ranges from about 4.9 GeV to about 500 GeV [19, 23]. They all show the large TSSA at x_F (Feynman-x, the longitudinal momentum fraction of the hadron production to the maximum possible longitudinal momentum, calculated as $x_F = \frac{p_L}{p_L^{max}}$) regardless of the $\sqrt{s}$. Recent experimental

studies at RHIC on TSSA aim to provide evidence for investigating the potential sources of the large TSSA at forward regions. At STAR, these measurements have been performed recently using π^0 or electromagnetic jets collected with the Forward Meson Spectrometer (FMS) for different physics processes, such as inclusive processes, diffractive processes, and the Drell-Yan process. The STAR Forward Upgrade program [24] will allow TSSA measurements for full jets, direct photons, and charged hadrons at the forward regions. These results generated significant interest in both experimental and theoretical studies aimed at understanding the underlying mechanisms of such sizable asymmetries. Despite decades of progress, the precise origin of the observed TSSA remains an open question.

On the theory side, two major frameworks are commonly accepted as the potential explanations of the large TSSA: the Transverse Momentum Dependent Factorization framework (TMD, detailed in Sec. 1.2.1) and the Higher-Twist Collinear Factorization framework (Twist-3, detailed in Sec. 1.2.2). In the TMD, the large TSSA arises from two potential sources: initial-state effect (Sivers effects) and final-state effect (Collins effects). In addition, there are other explanations for the large TSSA, including initial- and final-state interactions, which involve soft gluon exchanges at the initial state or the final state [25, 26].

1.2.1 Transverse Momentum Dependent Factorization framework (TMD)

The Transverse Momentum Dependent (TMD) factorization framework is a QCD-based theoretical approach developed to describe high-energy hadronic processes in which the intrinsic transverse momentum of partons plays a crucial role. Within this framework, non-perturbative aspects of hadron structure are encoded through TMD parton distribution

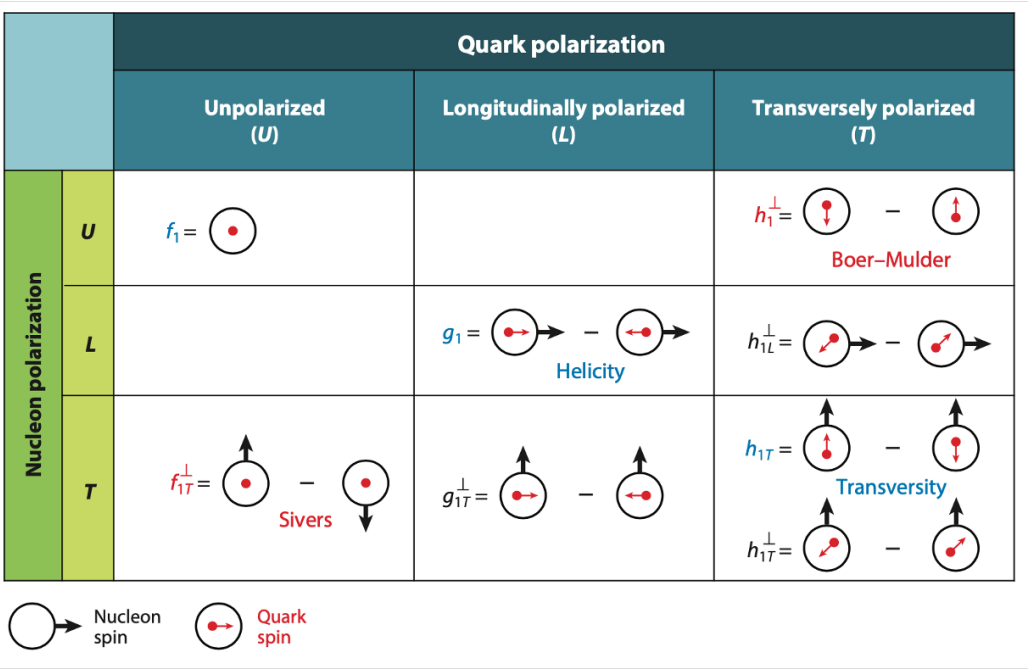

Figure 1.3: The leading-order of the TMD PDFs for quarks, classified according to the polarizations of the quark and the polarization of the nucleon.

functions (TMD PDFs) and fragmentation functions (TMD FFs), which depend explicitly on both the transverse momentum (k_T) and polarization degrees of freedom. Observables that are particularly sensitive to the low-k_T region, such as those measured in Drell–Yan and semi-inclusive deep inelastic scattering processes, provide direct access to the intrinsic transverse motions of partons inside hadrons. These measurements enable studies of the rich structure of TMDs and offer insights into the three-dimensional imaging of the proton, the orbital motion of partons, spin–orbit correlations, and principles of gauge invariance and universality in QCD physics [27, 28, 29].

The leading-order of the TMD PDFs contains eight functions of quarks, classified according to the polarization of both the quark and the nucleon: unpolarized(U), longitudinally polarized(L), and transversely polarized(T). Details are shown in Fig. 1.3 [29].

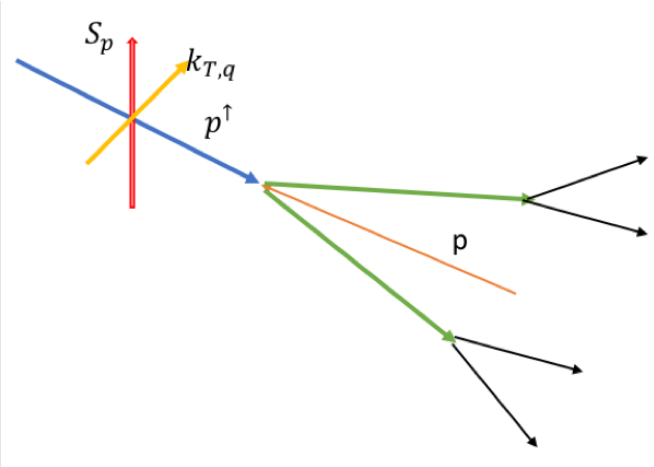

Figure 1.4: A schematic picture showing the Sivers effect in proton-proton collision.

Among the leading-order TMD PDFs for quarks, the Sivers function ($f_{1T}^{\perp}$) plays a vital role in the TSSA. Its effect, known as the Sivers effect, was first proposed by D. Sivers in 1990 [30]. It describes the correlation between the intrinsic transverse momentum of a parton ($\overrightarrow{k}_T$) and the transverse spin of the parent hadron ($\overrightarrow{S}_T$). Figure 1.4 shows a schematic picture of the Sivers effect. Incorporating such correlation, quark TMD PDFs in a transversely polarized proton can be expressed as:

$$\hat{f}_{q/p^\uparrow}(x, \overrightarrow{k}_\perp) = f_{q/p}(x, k_\perp) + \frac{1}{2}\Delta^N f_{q/p^\uparrow}(x, k_\perp)\overrightarrow{S} \cdot (\hat{P} \times \hat{k}_\perp), \tag{1.4}$$

where Δ^N is the density matrix. $\hat{P}$ is the vector unit of the proton momentum. The first experimental evidence for a non-zero Sivers function was reported by the HERMES Collaboration[31].

The Sivers function is process-dependent within the TMD framework, exhibiting a well-known sign change between the semi-inclusive deep inelastic scattering (SIDIS) process and the Drell–Yan (DY) process [29, 32]. In SIDIS, the Sivers asymmetry arises from final-

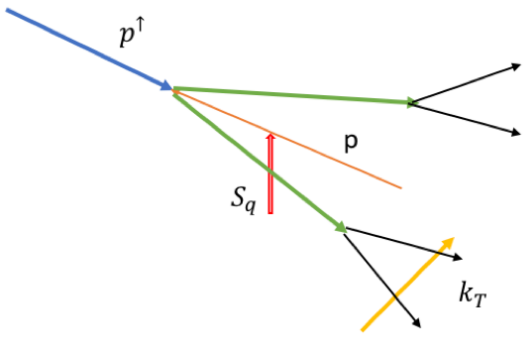

Figure 1.5: A schematic picture showing the Collins effect in proton-proton collision.

state interactions between the struck quark and the target remnant. In contrast, in the Drell–Yan process, such asymmetry originates from initial-state interactions between the incoming partons. This predicted sign reversal is regarded as a fundamental test of QCD. The sign change was first experimentally observed in the COMPASS experiment [33].

Another explanation for the large TSSA in the TMD factorization framework is the Collins effect, which describes the correlation between the transverse momentum of the fragmentation hadron and the spin of its parent quark, which J. Collins proposed [34]. Figure 1.5 shows a schematic picture of the Collins effect. Unlike the Sivers effect, the Collins effect is a final-state effect, manifesting the final-state fragmentation function, which describes the distribution of final-state particle production in a certain process, through the Collins fragmentation function ($H_1^{\perp}$). This fragmentation function characterizes the distribution of hadrons resulting from quark fragmentation and can generate azimuthal asymmetries in the angular distribution of the produced hadrons. The Collins effect can be experimentally measured via SIDIS processes [35] or proton-proton collisions [36].

1.2.2 Higher-Twist Collinear Factorization framework (Twist-3)

The higher-twist collinear factorization framework (Twist-3) extends the standard leading-twist collinear factorization within the TMD framework by incorporating the contributions that scale by additional powers of the hard scale, Q^2, the squared momentum transfer. Unlike the TMD factorization, the Twist-3 formalism explicitly requires a large momentum transfer as the "hard scale". Under this framework, the leading contribution to the TSSA arises from the quantum interference between a partonic scattering amplitude involving an active parton and another with an active two-parton composite state [37]. This interference can be represented by a universal Twist-3 quark-gluon correlation function, known as the Efremov-Teryaev-Qiu-Sterman (ETQS) function [38, 39]. The ETQS function is also related to the Sivers function with an integral over the transverse momentum:

$$T_F^q(x,x) \sim \int d^2k_T k_T^2 f_{1T}^{\perp q}(x,k_T) \tag{1.5}$$

As can be seen in this equation, the TMD framework is appropriate in the small-k_T region, while the collinear twist-3 approach becomes valid in the large-k_T regime. More specifically, when the momentum transfer ("hard" scale (Q)) is much greater than the transverse momentum ("soft" scale (q_T)), $Q \gg q_T$, the contribution from TMD framework is dominant; while at $q_T \gg \Lambda_{QCD}$ and $Q \gg \Lambda_{QCD}$, where Λ_{QCD} is the strong interaction scale, the twist-3 collinear factorization framework provides the leading contributions. However, in the region where $Q \gg q_T \gg \Lambda_{QCD}$, both frameworks provide similar contributions [40].

1.3 Diffractive Processes

1.3.1 Physics for diffractive processes

In high-energy collisions, final-state products, including the secondary decay products, fill almost the entire rapidity interval, where the rapidity is defined as $y = \frac{1}{2} \ln \frac{E+p_z c}{E-p_z c}$. However, some processes with a large interval of rapidity are devoid of any hadronic production. Such an interval is called a large rapidity gap, which is usually more than four units in rapidity. Although most frequent case of events with a large rapidity gap correspond to elastic scattering (e.g., $p + p \to p + p$), some events involve the transformation or dissociation of one or both incoming particles into a set of two or more final-state particles, with a total mass significantly smaller than $\sqrt{s}$ for the collision and preserving the proton quantum number [41]. These processes are governed by the exchange of a colorless object, typically a Pomeron, which is a Regge trajectory associated with vacuum quantum number exchange [42]. The name of these kinds of processes, "diffractive" processes, was introduced based on the pattern of the differential elastic cross-section as a function of the Mandelstam variable t (the momentum transfer between the target and the projectile), shown by the solid line in the right panel of Fig. 1.6. Such a pattern, characterized by the rotating peaks (maxima) and valleys (minima), resembles the diffractive pattern of the light intensity observed on a planar screen behind the circular obstacle in wave optics, shown in the left panel of Fig. 1.6 [28]. The presence of a large rapidity gap suggests that the diffractive cross-section results from the exchange of multiple partons with net zero color between the target and

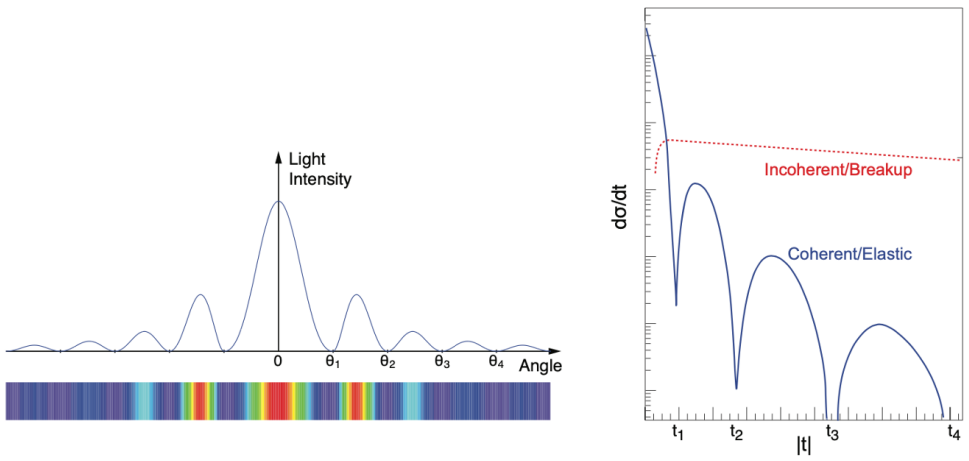

Figure 1.6: Left panel: The diffractive pattern of light on a circular obstacle in wave optics. Right panel: The diffractive cross-section in high-energy scattering. The solid line shows the elastic differential cross-section, while the dashed line shows the differential cross-section for the situation where either the projectile or the target breaks up. The elastic cross-section is analogous to the diffractive pattern in the left panel if identifying $|t| \approx k^2\theta^2$

the projectile. In high-energy scattering, this color-neutral exchange at the lowest order involves at least two exchanged gluons [28].

Experimentally, diffractive processes can be categorized depending on whether the target and projectile are dissociated. The single diffractive process refers to either the target or the projectile being dissociated, shown in Fig. 1.7 (a). In the double diffractive process, both the target and projectile are dissociated, shown in Fig. 1.7 (b). To determine the diffractive processes, two features are used experimently: large rapidity region in the detector devoid of hadronic activity (large rapidity gap); if one or both incoming particles stay intact after collision and are detected by dedicated forward detectors, its (their) fraction of momentum loss of the initial particle should be typically smaller than 0.15 [41].

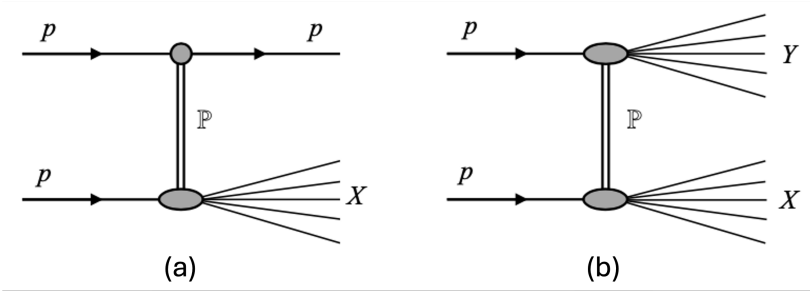

Figure 1.7: Schematic diagrams of (a) single diffractive process and (b) double diffractive process.

The diffractive processes constitute a non-negligible part of the cross section in collisions. In HERA experiments, it is found that about 15% of the total cross-section in the $e+p$ collision is due to diffractive processes [43]. Furthermore, the diffractive scattering events count about 25% of the total inelastic $p+p$ cross-section at the RHIC center-of-mass energies [44]. These indicate that the diffractive processes can serve as a key tool to study various physics programs at RHIC and at the future EIC, including the nuclei' spatial structure, orbital momentum of partons in protons with low-x, and saturation physics [23].

1.3.2 Indication of large TSSA originating from the diffractive processes

In addition to the well-established theoretical mechanisms discussed in Sec. 1.2, there are some indications in the experiment on the origin of the large TSSAs that the large TSSA could arise from diffractive processes. However, it has not been proven by any theories. Figure 1.8 shows the TSSA of the inclusive π^0 in polarized $p+p$ collisions at STAR [19]. In this figure, two different types of π^0 are considered: the isolated π^0 and the non-isolated π^0. The isolated π^0 refers to the π^0 without any particles nearby, while the non-

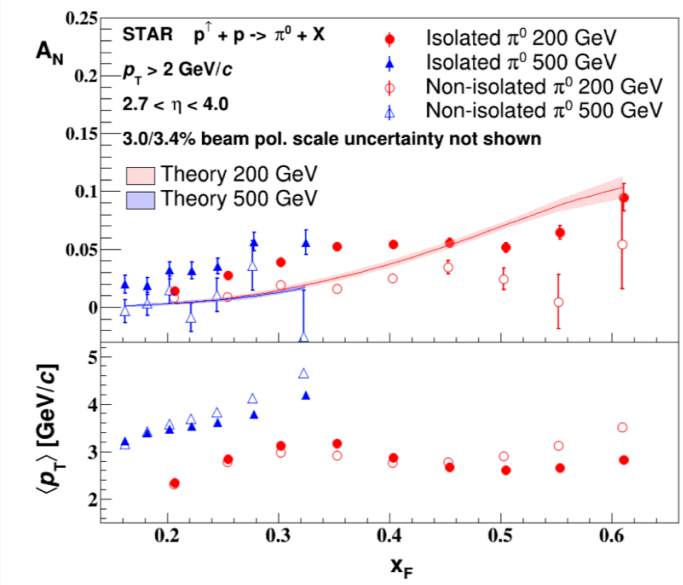

Figure 1.8: Transverse single-spin asymmetry for inclusive π^0 at forward rapidity using $p^{\uparrow}+p$ collisions at $\sqrt{s} = 200$ and 500 GeV at STAR. The isolated π^0 A_N are shown in solid points, while the non-isolated π^0 A_N are shown in empty points.

isolated π^0 does not have such requirement. The TSSA for the isolated π^0 is significantly larger than that for the non-isolated π^0. In addition, Fig. 1.9 shows the TSSA for inclusive electromagnetic jet (EM-jet) in polarized $p+p$ collisions at STAR [45]. This result shows the TSSA with a dependency on EM-jet photon multiplicity (number of photons within an EM-jet). Low photon multiplicity EM-jets exhibit a much larger asymmetry than high-multiplicity EM-jets. Since most low photon multiplicity EM-jets can be attributed to jets reconstructed predominantly from isolated π^0, this result is consistent with the behavior seen in the isolated π^0 A_N measurement. Both isolated π^0 and low-multiplicity EM-jets share a key characteristic associated with diffractive scattering: the presence of a rapidity gap. These observations, therefore, provide compelling indications that the large forward TSSA may originate from diffractive processes.

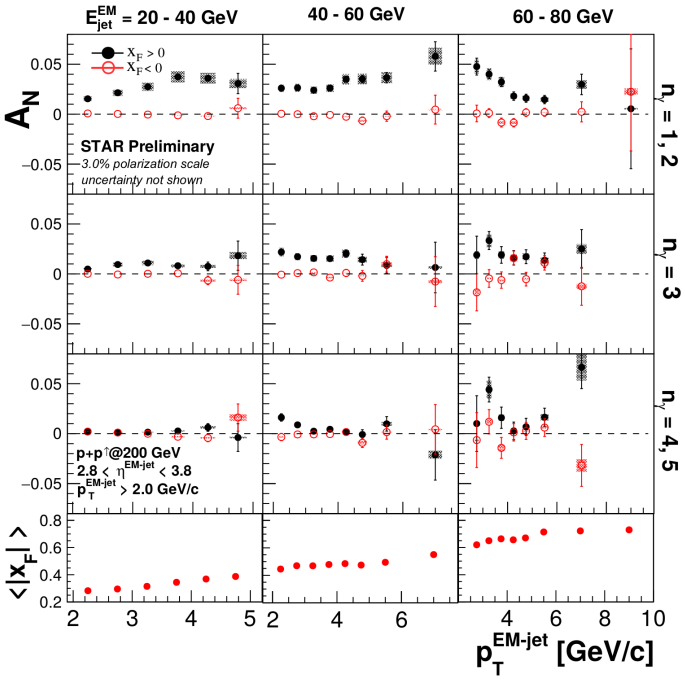

Figure 1.9: Transverse single-spin asymmetry for inclusive EM-jets at forward rapidity using $p^{\uparrow} + p$ collisions at $\sqrt{s} = 200$ GeV at STAR. Three cases of photon multiplicity (n_γ) are mentioned for extracting A_N: $n_\gamma = 1, 2$, $n_\gamma = 3$, $n_\gamma = 4, 5$.

1.4 Structure of this dissertation

In this dissertation, studies of transverse single-spin asymmetry of electromagnetic jets (EM-jets) for diffractive events using $p^{\uparrow} + p$ collisions at $\sqrt{s} = 200$ and 510 GeV at STAR are reported. Types of events used in these studies include single diffractive events, rapidity gap events (with a large fraction of single diffractive events), and semi-exclusive events (diffractive-like events).

The remaining chapters of this dissertation are arranged as follows: Chapter two describes the experimental facilities of RHIC, major detectors at the STAR experiment used for this dissertation, and the basic information and quality assurance check for the datasets used; Chapter three focuses on the TSSA for EM-jets in single diffractive events; Chapter four focuses on the TSSA for EM-jets in rapidity gap events; Chapter five focuses on the TSSA for EM-jets in semi-exclusive events; Chapter six provides the conclusions, discussions, and outlooks.

Chapter 2

Experiment

2.1 Relativistic Heavy Ion Collider (RHIC)

The Relativistic Heavy Ion Collider, also called RHIC, is a large nuclear physics facility located at Brookhaven National Laboratory (BNL) in the United States. Figure 2.1 shows the general design of RHIC, focusing on the polarized proton operation [46]. The major physics goals of RHIC include exploring the new high-energy form of matter (the quark-gluon plasma, which consists of interacting quarks, anti-quarks, and gluons), as well as investigating the proton spin structure. To achieve these physics goals, RHIC is designed to be capable of colliding a wide range of ions, including Uranium (U), Gold (Au), and Aluminium (Al), at various center-of-mass energies up to 200 GeV. Furthermore, RHIC also has the unique capability to collide polarized proton beams with center-of-mass energies of about 200 GeV and 500/510 GeV. RHIC is the only collider in the world that can provide polarized proton beams, providing unique opportunities to study the proton spin structure [47, 48, 49].

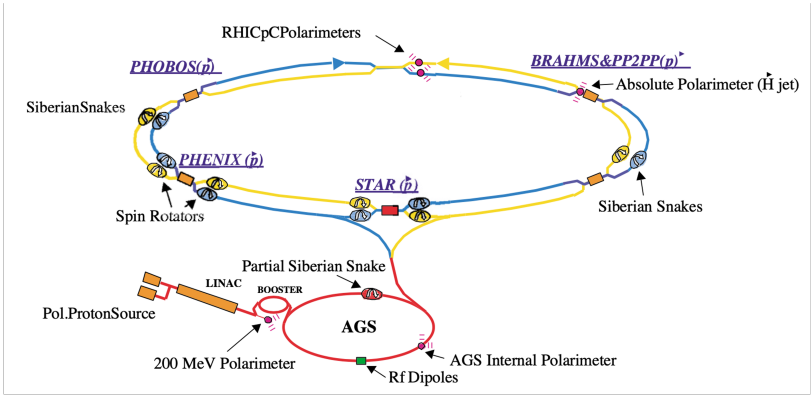

Figure 2.1: The general layout of the RHIC facility, focusing on the polarized proton operation.

To generate the polarized proton beam used in collisions, the process begins with the optically pumped polarized ion source (OPPIS), which produces polarized H^- (hydrogen ion) in a single pulse of 300 μs, containing approximately 9×10^{11} polarized H^-. The polarized proton is obtained after the polarized H^- collides with helium atoms and after the electron is captured with optically pumped Rb vapor [50]. Then, the polarized proton beam is accelerated to 200 MeV with the LINAC with approximately 50% efficiency. Afterwards, the polarized proton pulse is injected and captured into a single bunch in AGS Booster. Each bunch in AGS Booster contains about 4×10^{11} polarized protons. The polarized proton in each bunch is accelerated to 1.5 GeV kinetic energy in the booster and then is transferred to the Alternating Gradient Synchrotron (AGS). Finally, the polarized proton is accelerated to 25 GeV before injection into RHIC.

At RHIC, polarized proton beams are accelerated and stored in two independent rings, each with a circumference of approximately 2.4 miles. The blue ring carries protons circulating clockwise, while the yellow ring carries protons circulating counterclockwise. Each ring is filled with up to 120 bunches of polarized protons, which are accelerated to the

desired collision energy. These processes typically last around 10 minutes. Once acceleration is complete and ready for physics collisions, bunches from the two rings collide at designated interaction points around RHIC. For example, one of the primary collision points is located at the STAR detector, located at the 6 o'clock location of the RHIC ring.

During acceleration, preserving beam polarization is one of the biggest challenges. The evolution of the spin direction of the polarized proton beam in external magnetic fields is governed by the Thomas-BMT equation [51, 52]: Eq. 2.1,

$$\frac{d\vec{P}}{dt} = -\left(\frac{e}{\gamma m}\right)[G\gamma\vec{B}_{\perp} + (1+G)\vec{B}_{\parallel}] \times \vec{P} \tag{2.1}$$

where the $\vec{P}$ is the polarization vector expressed in the frame that is moving with the particle, $\vec{B}_{\perp}$ and $\vec{B}_{\parallel}$ are the components of the magnetic field perpendicular and parallel to the particle's velocity, respectively, $G = 1.7928$ is the proton anomalous magnetic moment and $\gamma = E/m$. At low energy, the longitudinal fields ($\vec{B}_{\parallel}$) can be effective in manipulating the spin motion, while the transverse fields ($\vec{B}_{\perp}$) dominate the spin motion at high energy. Furthermore, a major complication arises from depolarizing resonances, which occur during acceleration. These depolarizing resonances include imperfection resonances, driven by magnetic errors and misalignment, as well as intrinsic resonances driven by the focusing fields. To resolve such an issue, the "Siberian Snake" [53] is employed at RHIC. It generates a 180° spin rotation about a horizontal axis on the proton beam. When the spin rotation from the Siberian Snake exceeds that from resonance-driving fields, the net polarization remains preserved throughout acceleration. Two sets of "Siberian Snake" are equipped at the opposite sides of the RHIC ring. In addition, spin rotators are inserted on each side of the two major interaction points, allowing the spin orientation of the polarized beams to

switch from aligning with the vertical plane to the longitudinal plane. With these facilities, RHIC is capable of providing either transversely polarized or longitudinally polarized proton beams [46].

The polarization of the beam is measured from the left-right asymmetry in the proton-Carbon elastic scattering in the Coulomb-Nuclear Interference (CNI) region. This is the asymmetry in the cross-section for scatter or particle production in the left and right regions, as shown in Eq. 2.2.

$$P_B = \frac{1}{A_p}\frac{N_L - N_R}{N_L + N_R} = \frac{1}{A_p}\epsilon \tag{2.2}$$

P_B is the beam polarization, N_L and N_R are the number of scatters in the left and right of the beam normalized by the luminosity, A_p is the analyzing power from experiment or theory, and ϵ is the raw asymmetry. At RHIC, two complementary polarimetry systems are used. One type is the proton-Carbon (pC) polarimeter, which is used to measure the relative polarization [54, 55]. The pC-polarimeter consists of a carbon ribbon target and six silicon strip sensors aligned at $\pm 45°$, $\pm 90°$, and $\pm 135°$ azimuthal angles with respect to the beam direction. Figure 2.2 shows the RHIC pC-polarimeter setup. The beam polarization can be studied based on the number of scatters detected on the sensors on both sides using Eq. 2.2. Although the absolute beam polarization cannot be obtained from the pC-polarimeter because the analyzing power is not known at RHIC energies, it can still measure both the relative beam polarization and its depolarization rate. The other type of polarimetry is the hydrogen gas jet (H-jet) polarimeter [54, 56]. The H-jet polarimeter consists of one atomic beam source, one Breit-Rabi polarimeter, and two recoil detectors on opposite sides. Figure 2.3 shows the schematic layout for the H-jet polarimeter. Polarization is measured from

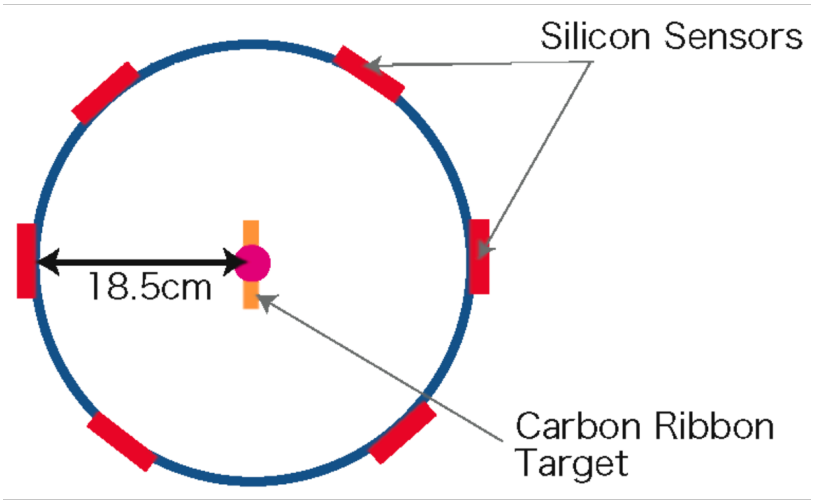

Figure 2.2: The setup for RHIC pC-polarimeter.

the left–right asymmetry in elastic scattering between the polarized proton beam and the polarized hydrogen target in the CNI region. The raw asymmetries for beam (ϵ_{beam}) and target (ϵ_{target}), from such proton-nuclear elastic scatterings, are calculated separately. The nuclear target polarization (P_{target}) is measured from the Breit-Rabi polarimeter. Since both scattering processes share the same analyzing power, the beam polarization (P_{beam}) can be calculated using Eq. 2.3.

$$P_{beam} = \frac{\epsilon_{beam}}{\epsilon_{target}} P_{target} \tag{2.3}$$

2.2 The STAR Experiment

The Solenoidal Tracker at RHIC (STAR) is one of the major experiments at RHIC. It is located at six o'clock at RHIC, as shown in Fig. 2.1. The STAR experiment is designed to achieve physics goals, including gaining a fundamental understanding of the internal

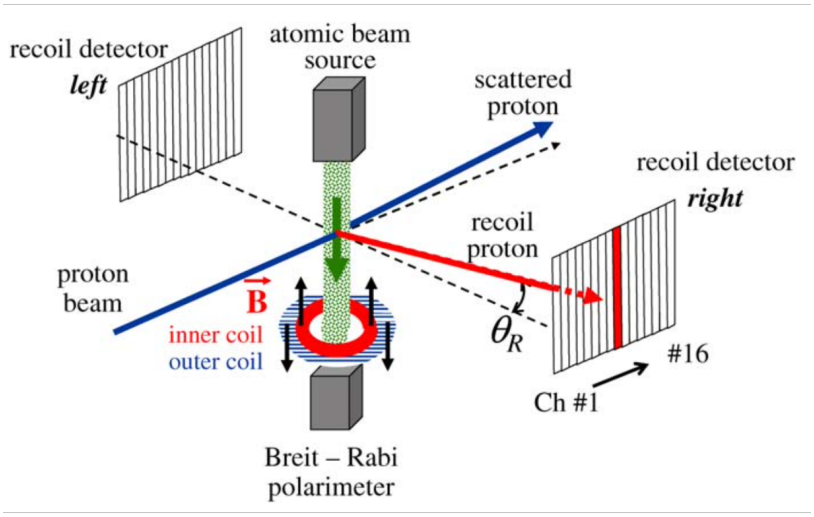

Figure 2.3: Schematic layout of RHIC H-jet polarimeter.

structure of hadrons and the mechanisms of hadronic interactions at high energy densities. A schematic of the STAR detector configuration in 2017 is shown in Fig. 2.4. The Time Projection Chamber (TPC) is the primary detector at STAR, which can reconstruct the tracks from the charged particles and measure their momenta, and identify the particle species [57]. The Barrel Electro-Magnetic Calorimeter (BEMC) [58], the Endcap Electro-Magnetic Calorimeter (EEMC) [59], and the Forward Meson Spectrometer (FMS) [60] are electromagnetic calorimeters that can be used to detect photons, electrons, and electromagnetic components from hadron decay. The BEMC, the EEMC, and the FMS cover distinct pseudorapidity ranges: $|\eta| < 1$, $1.1 < \eta < 2$, and $2.6 < \eta < 4.2$, respectively. The Beam-Beam Counters (BBC) [61], the Vertex Position Detector (VPD) [62], and the Zero-Degree Calorimeter (ZDC) [63] are the major trigger detectors in the STAR experiment. All three trigger detectors are located on both sides of the STAR detector. They can provide the primary input to the STAR trigger systems, which can be used for preliminary event se-

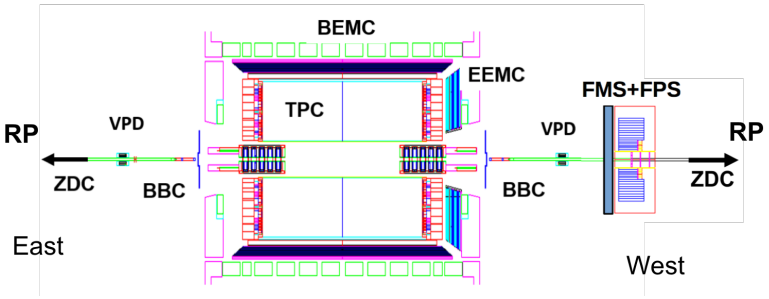

Figure 2.4: Schematic layout of the major STAR detectors in 2017. The abbreviations of the STAR sub-detectors are explained in the main contents.

lection criteria to determine collision events. Details of the STAR trigger systems can be found in [64]. Furthermore, these trigger detectors can measure the relative luminosity and determine the primary vertex. The Roman Pot detectors (RP) [65] are used to detect the slightly scattered protons near the beam in proton-proton collisions and reconstruct their momenta.

The primary detectors used for these analyses include the FMS, RP, and BBC, which are described in detail in the following subsections.

2.2.1 Forward Meson Spectrometer (FMS)

The Forward Meson Spectrometer (FMS) is a lead-glass electromagnetic calorimeter covering the pseudorapidity range of $2.6 < \eta < 4.2$. It is located about 7 m west of the STAR interaction point. Figure 2.5 shows the schematic layout of the FMS [20]. The FMS comprises 1,264 cells, which are divided into two parts based on the cell size, shown in Fig. 2.5. The outer region comprises 788 cells with a size of about 5.8 cm $\times$ 5.8 cm, while the inner region comprises 476 cells with a size of about 3.8 cm $\times$ 3.8 cm. By convention, the larger cells are referred to as large cells and the smaller ones as small cells. In terms

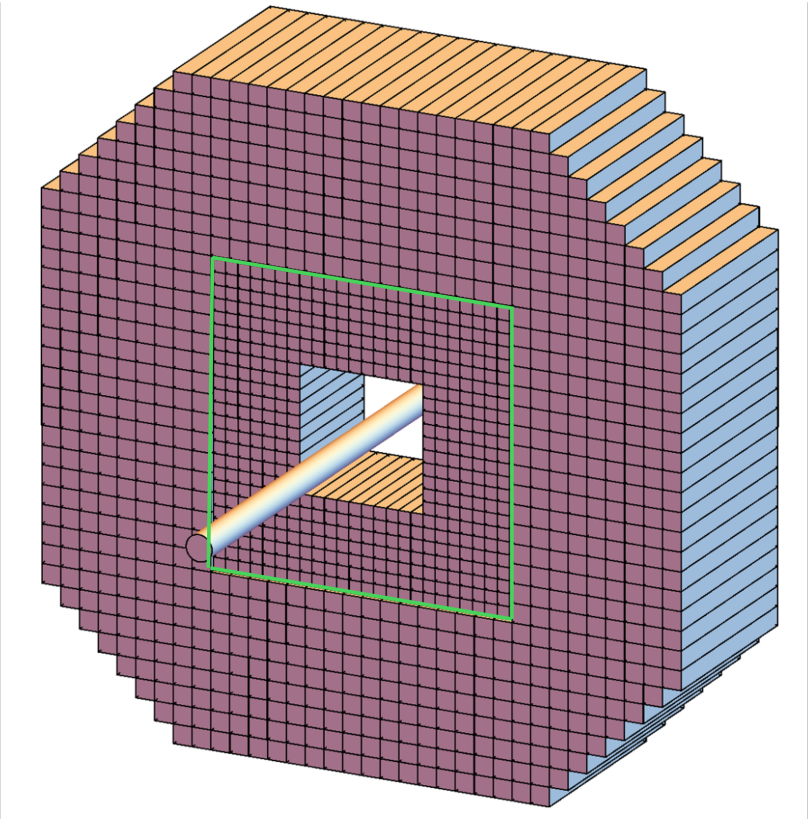

Figure 2.5: The schematic layout of the FMS. All the cells are displayed in the cartoon. The green lines split the FMS small cell region and the FMS large cell region.

of acceptance, the large cell region covers $2.6 < \eta < 3.3$, while the small cell region covers further forward to $3.3 < \eta < 4.2$.

The FMS is capable of detecting the electromagnetic particles, including photons and electrons. Separation of photons and electrons is achieved using the pre-shower (FPS) and post-shower (FPOST) detectors. In addition, neutral mesons such as π^0 and η can be reconstructed from photon candidates from the FMS. When the photon hits FMS, it interacts with the detector materials and loses energy, primarily through pair production. The resulting electrons and positrons from pair production radiate secondary photons via

the bremsstrahlung process, which in turn undergo further pair production. This cascade continues until the photon energies fall below the critical energy of the material, which for the FMS is approximately 10 MeV. Each FMS cell has a depth of about 18 radiation lengths, which is sufficient to fully deposit the photon energy.

The readout of each FMS cell uses the photon multiplier tube (PMT) attached to the end of each cell. The PMT can detect the Cerenkov lights, which are photons moving faster than the speed of light in the material. The energy for the photon deposited in one cell is proportional to the integral of the readout of the PMT within the time bin window for each event.

However, not every event is recorded. To efficiently select events relevant to the physics goals, the FMS trigger system is applied as a basic event selection criterion, operating in a manner similar to the STAR trigger system. There are two types of FMS triggers. The first type is the FMS Board Sum triggers. Events with the sum of the transverse energy within the localized overlapping regions passing the designed threshold are accepted. Details on defining the FMS Board Sum triggers can be found in [66]. Another type is the FMS Jet Patch triggers. Events are accepted if the sum of the transverse energy within a designated quadrant of the detector exceeds the designed threshold. Six designed quadrant areas for the FMS Jet Patch triggers are designed, with details in [66]. For each trigger type, three thresholds are implemented: small-cell Board Sum (FMS-sm-BS), large-cell Board Sum (FMS-lg-BS), and Jet Patch (FMS-JP). Their thresholds are listed in Tab. 2.1 in the unit of transverse momentum (p_T). Events passing the lower threshold in each category are subject to pre-scaling, meaning that only a fraction of the events passing these

Trigger name	p_T threshold in 2015 [GeV/c]	p_T threshold in 2017 [GeV/c]
FMS-JP0	1.6	1.6 / 7.6
FMS-JP1	2.4	3.0
FMS-JP2	3.2	4.5
FMS-sm-bs1	1.0 / 1.1	1.0 / 1.3
FMS-sm-bs2	1.6	2.0 / 2.4
FMS-sm-bs3	1.9 / 2.2	2.8 / 3.8
FMS-lg-bs1	1.0 / 1.1	1.0 / 1.3
FMS-lg-bs2	1.6	1.7 / 2.4
FMS-lg-bs3	2.4	3.0 / 4.6

Table 2.1: FMS trigger threshold for the major triggers used in this analysis. Some of the trigger thresholds were adjusted during the RHIC proton-proton collision period. Therefore, multiple trigger threshold values were shown for those triggers.

triggers are recorded in the database. By contrast, the events passing the highest threshold for each type are all recorded.

2.2.2 Roman Pot (RP)

The Roman Pot (RP) detectors are designed to detect protons scattered at very small angles, which are those close to the beam. These RP detectors were taken over from the PP2PP experiment at RHIC [67]. The RPs at STAR are able to provide outstanding effi-

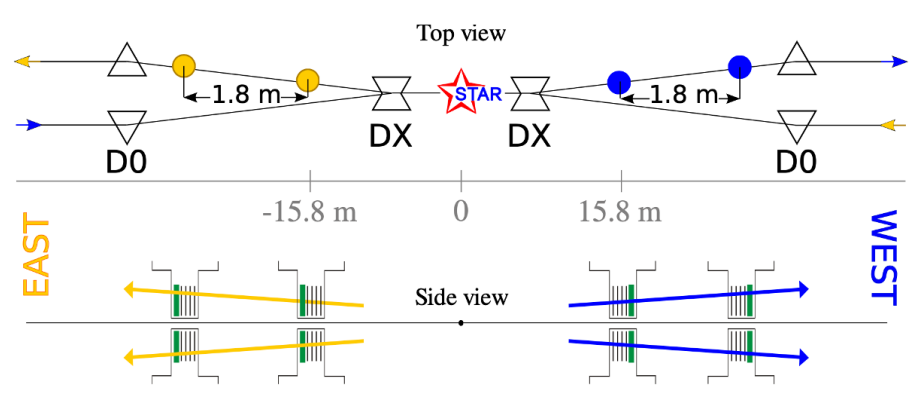

Figure 2.6: (Top) The schematic layout of the STAR RP system (not to scale). The blue points indicate the two RP stations on the west side of STAR, and the yellow points indicate the two RP stations on the east side of STAR. (Bottom) The schematic layout for displaying RP stations on the side view. Each RP station consists of two RP vessels, housing four SSD planes (represented by black solid lines) and one scintillation counter (represented by a green solid box).

ciency in tagging the forward-scattered protons, with an excellent capability for suppressing the non-exclusive background [65].

Figure 2.6 shows the schematic design of the RP system at STAR [68]. RP detectors are located on both sides (east side and west side) of the STAR. On each side, two RP stations are set up at about 15.8 meters and 17.6 meters from the STAR interaction point. Each station contains two RP vessels above and below the beam pipe. Each vessel consists of four Silicon Strip Detectors (SSDs) and one scintillation counter. The SSDs are arranged such that two measure hits in the x-direction and two measure hits in the y-direction. The scintillation counter serves as a forward-proton trigger and provides timing information [68].

At STAR, the RP systems are placed between the RHIC dipole DX and D0 magnets, as shown in the top panel of Fig. 2.6. The DX dipole magnets target the incoming beams and bend the outgoing beams back into the beam pipe, while also provide a uniform

magnetic field. This field enables reconstruction of the proton momentum from its measured scattering angle and hit position at the RP detectors.

The RP track reconstruction includes several steps. First of all, the energy deposit in the SSD planes is required to be larger than $5\sigma_{ped}$, where σ_{ped} is the average pedestal width [69], to distinguish the noise. Then, the clustering procedure for each SSD plane is performed, as shown in [70]. Afterwards, the cluster matching between planes measuring the same coordinates is performed to reconstruct the hit point position in (x,y) coordinates in one RP station. Finally, the reconstructed hit point positions in both RP stations on the same side (either the east side or the west side) are used to reconstruct the RP track [71].

2.2.3 Beam-Beam Counter (BBC)

The Beam-Beam Counter (BBC) is a system of scintillator annuli mounted around the beam pipe, located approximately 3.7 meters from the STAR interaction point (IP) on both the east and west sides. The BBC provides full 2π azimuthal coverage and spans the pseudorapidity range $2.1 < |\eta| < 5.0$. On each side of the BBC, there are six small hexagonal scintillator tiles in the inner region, called the small BBC region, which covers $3.4 < |\eta| < 5.0$, and twelve large hexagonal scintillator tiles in the outer region, called the large BBC region, which covers $2.1 < |\eta| < 3.4$. Figure 2.7 shows the schematic layout for BBC scintillator tiles [72]. During the proton-proton collision period, the BBC serves multiple functions, including providing the minimum-bias trigger, monitoring the instantaneous and integrated luminosity, and measuring the relative luminosity between different proton spin orientations [61, 73]. Furthermore, specifically for this analysis, the

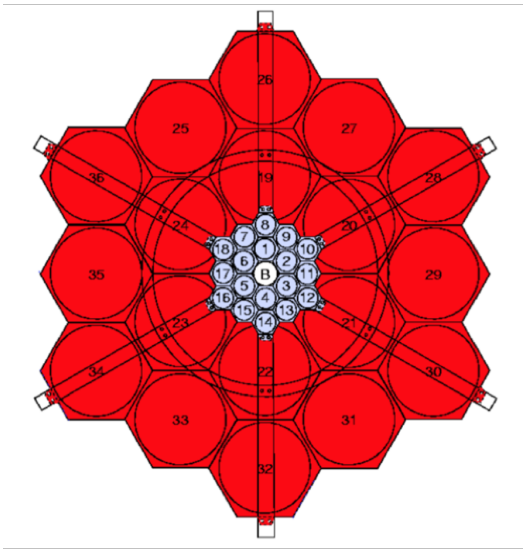

Figure 2.7: Schematic layout for BBC detector on the front view. The tiles in the large BBC region are shown in red, while the tiles in the small BBC region are shown in grey.

east side BBC is used to determine the rapidity gap for diffractive events, as it covers approximately 3 pseudorapidity units between the east RP and the FMS.

2.3 Dataset

2.3.1 Information for the Dataset

Two datasets are used for these analyses. The first is the transversely polarized proton-proton collisions at $\sqrt{s}$ = 200 GeV collected at STAR during 2015, simplified as the Run 15 dataset. The second is the transversely polarized proton-proton collisions at $\sqrt{s}$ = 510 GeV collected at STAR during 2017, simplified as the Run 17 dataset. The average beam polarizations for these datasets are about 57% and 55%, with integrated luminosities of about 52 pb^{-1} and 350 pb^{-1}, respectively. These high-luminosity datasets with good average beam polarization provide a unique opportunity for this study.

At RHIC, a fill refers to the period from beam injection until the beams are dumped. For polarized proton–proton collisions, a fill typically lasts around eight hours, although shorter durations could occur depending on beam quality. Within each fill, there are several runs at STAR; a run, in this context, refers to about a half-hour of data taking. During a run, events that satisfy specific triggers are written to different data streams according to the trigger configuration. For this analysis, the FMS stream is used, which records the events passing the FMS triggers. This stream includes information from the STAR trigger system, trigger detectors (for example, the BBC), the FMS, and the RP.

2.3.2 Quality Assurance

Before performing any physics analysis, it is essential to carry out quality assurance (QA) of the dataset to ensure that the data are reliable and ready for use. The QA includes two major parts: quality checks of each run (and fill), and detector calibrations. In this section, only the calibration of the FMS is discussed for the Run 15 dataset and the Run 17 dataset. In this section, only the calibration of the FMS is discussed.

The FMS detector for both the Run 15 dataset and the Run 17 datasets was calibrated by the STAR collaboration [74, 75]. The calibration procedure in both cases relied on the π^0 reconstruction method. Since the π^0 meson decays into two photons, it can be reconstructed by two photons at the FMS. By comparing the deviation of the reconstructed invariant mass from the two photons to the π^0 invariant mass, the conversion between ADC values and deposited energy in each FMS cell is iteratively adjusted. This process is repeated until the reconstructed invariant mass aligns with the nominal value

(π^0 invariant mass) within the expected resolution. Details of the π^0 reconstruction can be found in Appendix A.

Furthermore, additional calibration procedures are applied to check and identify the other calibration issues, including the bit shift, hot channels, and bad channels, with details shown as follows:

- Bit shift: This is due to the mismatch between the ADC and the binary bit. To detect this issue, ADC values are converted into binary format and compared with the expected pattern from the database.

- Hot channel: The hot channel refers to the number of hits in an FMS cell far higher than average. If identified, manually mask out this cell. Furthermore, in this analysis, additional hot channel masking is performed based on the EM-jet distribution with a fill-by-fill basis. Cells exhibiting significantly higher EM-jet yields than average are masked out. Figure 2.8 shows an example of EM-jet distribution before (left) and after (right) additional hot channel masking. After the hot channel masking, the EM-jet distribution becomes more evenly distributed.

- Bad channel: The bad channel refers to the number of hits in an FMS cell far lower than average or close to zero. The bad channels can be easily identified by checking the ADC spectra and the number of hit distribution. The bad channels are excluded in these analyses.

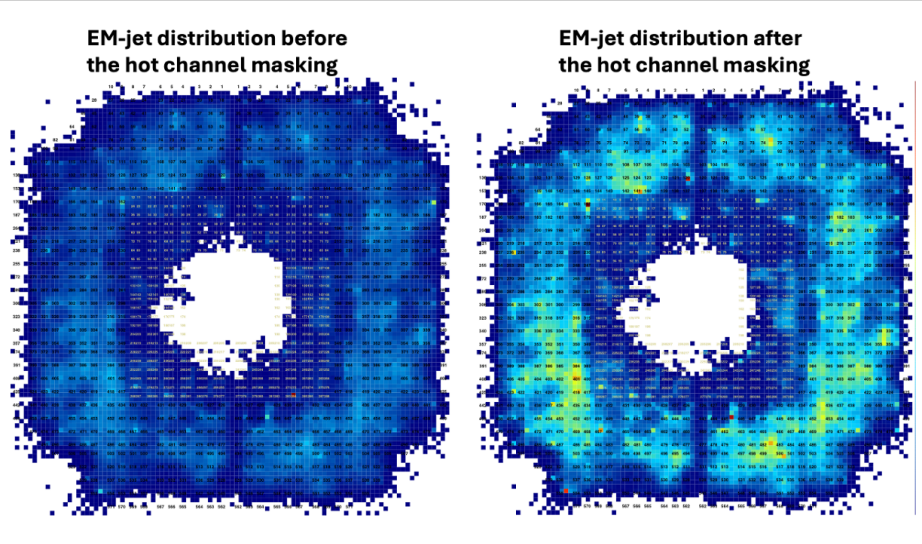

Figure 2.8: Example of the EM-jet distribution for an entire fill. The numbers are the FMS cell ID. The left plot shows the distribution before the additional hot channel masking. The red spots are considered the hot channels, which are manually masked out. The right plot shows the distribution after the additional hot channel masking. The red spots are mostly gone, and the EM-jet distribution is closer to evenly distributed.

Chapter 3

Transverse Single-spin Asymmetry for Single Diffractive Events

3.1 Event Selection

The single diffractive event used for this analysis requires only one EM-jet at FMS, one proton track on the east side RP, and the veto on the east side BBC. A schematic cartoon describing the single diffractive event is shown in Fig. 3.1. The list of event selection criteria for the single diffractive events used in the Run 15 dataset and the Run 17 dataset can be briefly summarized into four categories: event property, EM-jet reconstruction, BBC east veto, and east RP track. The details for these categories of event selection criteria are described in the following sub-sections.

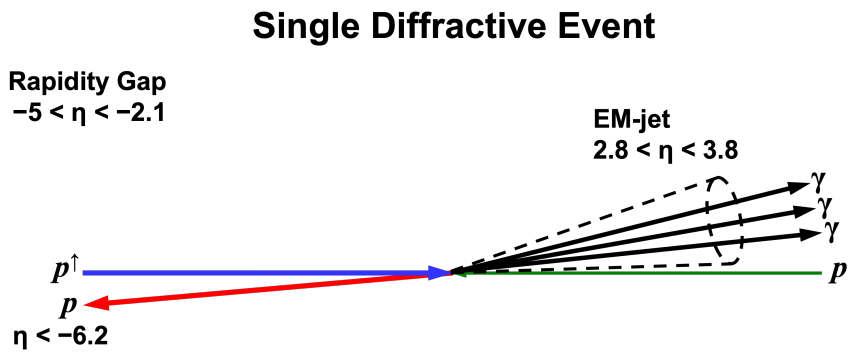

Figure 3.1: A schematic cartoon describing the single diffractive events used for this analysis.

3.1.1 Event Property Cuts

To begin with, the proton bunch of each event is checked. Although RHIC is capable of 120 bunches of protons, only 111 bunches of protons were injected during the Run 15 period and the Run 17 period. The remaining 9 are empty bunches void of protons, which can be used for background studies. The bunch ID can be used to identify the bunches with and without protons. In the analyses mentioned in the dissertation, only the bunches with protons in the blue and yellow beams are accepted.

Then, the spin patterns of the blue beam proton and the yellow beam proton are checked. In this analysis, the proton is transversely polarized. In this case, the spin pattern can be described as either up or down. The spin patterns for each beam are obtained from the bunch crossing for each event, described in Tab. 3.1. In this table, the spin patterns for both the blue and yellow beams are combined into 4-spin bit. Only events satisfying any of the following four 4-spin bit cases in Tab. 3.1 are accepted.

After that, the primary vertex position in the z-direction (vertex z) must be within 80 cm of the STAR IR, i.e., $|z| < 80$ cm, for this analysis. The primary vertex is determined

Table 3.1: Four acceptable 4-bit spin patterns

4-bit spin	Base-10	Blue beam polarization	Yellow beam polarization
0101	5	up	up
0110	6	up	down
1001	9	down	up
1010	10	down	down

as a priority for the vertex obtained from TPC, VPD, and BBC. This means that the TPC vertex is checked first. If it exists, the primary vertex for this event is the TPC vertex. If not, the VPD vertex is then checked. If it exists, the primary vertex for this event is the VPD vertex. If not, the BBC vertex is checked afterwards. If it exists, the primary vertex for this event is the BBC vertex. If the vertex can not be found from any of these detectors, the primary vertex in the z direction for this event is set to be 0.

The fractions of the primary vertex obtained from the TPC, the VPD, and the BBC for events without any other cuts are approximately 1%, 33%, and 50%, respectively. Specifically, it should be mentioned that, in reality, the fraction of all events with BBC vertex is more than 50% because some fraction of the events with TPC vertex or VPD vertex also have BBC vertex.

3.1.2 EM-jet Reconstruction

In high-energy physics and nuclear physics, jets play a vital role in experiments. Jets are collimated sprays of the final-state particles formed when high-energy quarks and

gluons undergo hadronization during particle collisions. Since it is impossible to isolate a quark or a gluon due to the confinement in QCD, a jet is an ideal proxy of a quark or a gluon in experiments. Studying the jets enables us to investigate the PDFs for quarks and gluons, allowing us to have a better understanding of the internal structure of the proton, as well as for the QCD physics [76].

The electromagnetic jet, commonly referred to as an EM-jet, is a jet reconstructed only using electromagnetic components. During the periods of Run 15 and Run 17, the FMS is the major detector in the forward region. However, it can detect photons and neutral mesons, but cannot detect charged hadrons. Furthermore, there were no detectors capable of detecting the charged hadrons within the same coverage as FMS for the two datasets used in these analyses. Therefore, the reconstructed jets mentioned in these analyses only contain electromagnetic components.

The FMS points are photon candidates used for the EM-jet reconstruction. Their determination follows a series of steps based on established procedures related to the FMS [77]. The basic unit in the FMS is the FMS hit, defined as an individual FMS cell with a non-zero ADC value. Clusters are first formed by grouping adjacent FMS hits into an FMS cluster. Each cluster is then classified as either a single-photon-type or a two-photon-type cluster, based on its size and energy distribution. Such a photon component inside the FMS cluster is called an FMS point. The photon component extracted from such a cluster is referred to as an FMS point. Once the cluster type is identified, the position and energy of each FMS point are determined using a shower-shape fitting algorithm. Further details of cluster-finding procedures and shower-shape fitting algorithms are provided in Ref. [77].

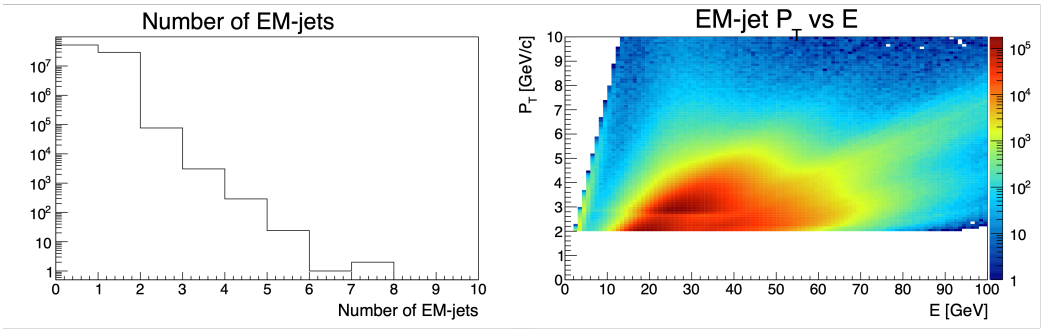

Figure 3.2: Quality insurance plots for EM-jet after the EM-jet reconstruction and p_T cuts for the Run 15 dataset. The left plot is the number of EM-jets in each event. The right plot is the EM-jet p_T vs energy distribution.

In these analyses, to reduce the noise background, only FMS points with $E > 1$ GeV are applied to the EM-jet reconstruction. The EM-jets are reconstructed using the anti-k_T algorithm from the FastJet package [78], with a resolution parameter of $R = 0.7$. Furthermore, the transverse momentum (p_T) of the EM-jet must be greater than both sets of thresholds to reject the soft background. The first set of thresholds is the trigger-dependent threshold, as shown in Tab. 2.1. The second threshold is a fixed threshold of 2 GeV/c. Figure 3.2 and Figure 3.3 show the number of EM-jets in each event (left plot) and the EM-jet kinematics (right plot) after the EM-jet reconstruction and p_T cuts for the Run 15 dataset and the Run 17 dataset, respectively.

After the EM-jet reconstruction, there are two kinds of corrections applied to the EM-jets. The first is the Underlying Event (UE) correction. The UE contribution is part of a jet, not from the parton fragmentation, but from secondary scattering or other processes. Such a contribution will deposit some energy into the jet, so a correction to the UE is required to subtract its energy from the jet. In these analyses, the off-axis cone

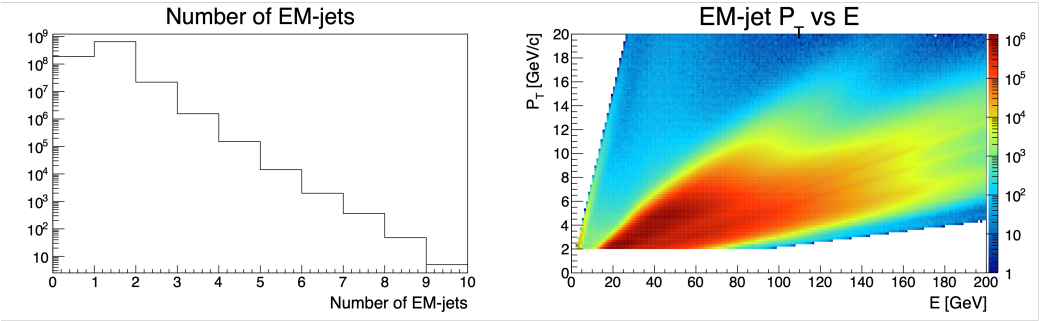

Figure 3.3: Quality insurance plots for EM-jet after the EM-jet reconstruction and p_T cuts for the Run 17 dataset. The left plot is the number of EM-jets in each event. The right plot is the EM-jet p_T vs energy distribution.

method estimates the UE contribution [79]. In this method, two off-axis jets with the same pseudorapidity but at opposite azimuthal angles ($\pm\pi/2$) at the edge of the original jet are reconstructed as UE background. Then, the UE energy density (ρ) can be calculated using $\rho = E/(\pi R^2)$, where E is the average UE energy and R is the UE jet radius. The fastjet program uses the "ghost particle" technique to calculate the jet area (A). The maximum "ghost particle" η is 5.0, and the "ghost area" is 0.04. Finally, the jet energy is subtracted by the UE energy: $E_{corrected} = E_{original} - \rho \times A$, where the corrected EM-jet energy is $E_{corrected}$, and the original EM-jet energy is $E_{original}$. Figure 3.4 shows a schematic cartoon for estimating the UE contribution with the off-axis cone method [79].

After the UE correction for the EM-jet energy, the next kind of correction is the detector-level to particle-level correction for the EM-jet energy. The major idea for such correction is that the energy of the EM-jet is calculated during the EM-jet reconstruction using the FMS point. The energy of the FMS points is measured and calculated at the detector level, which may be potentially affected by the resolution of the FMS and the algorithms used for cluster finding and shower shape fitting, which form the FMS points.

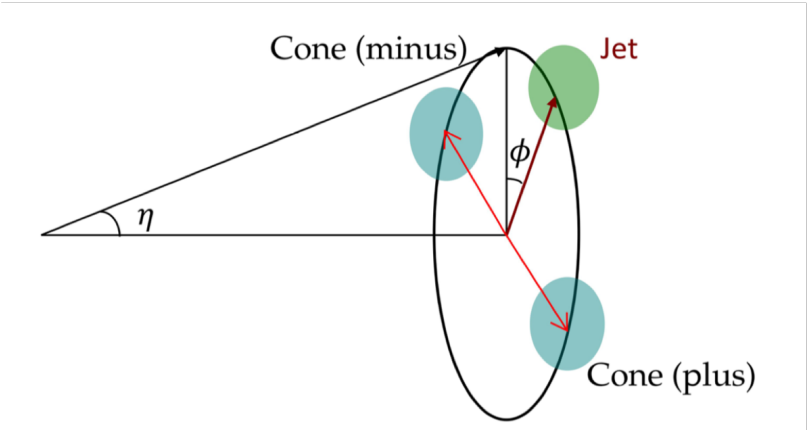

Figure 3.4: The schematic cartoon for the Underlying Event contribution estimation using the off-axis cone method.

Therefore, a simulation is necessary to investigate their effects and correct the EM-jet energy from the detector level to the particle level.

This correction is based on a Monte Carlo simulation using both particle-level simulation with PYTHIA and detector-level simulation with GEANT3. For the particle level simulation, the proton-proton collisions with $\sqrt{s} = 200$ GeV are generated, with the tune setting of Perugia2012 (Tune parameter 370) [80, 81]. Then, the GEANT3 simulation framework, with FMS detector response implemented within the STAR simulation framework, is used for the detector-level simulation [82]. Afterwards, the EM-jet reconstruction, using the same criteria as for the data, is applied to reconstruct both the detector-level EM-jets and the particle-level EM-jets. The left panel of Fig. 3.5 shows the particle-level FMS EM-jet energy plotted against the matched detector-level EM-jet energy in the simulation for the Run 15 dataset. To better describe the relation of the detector-level EM-jet energy and the particle-level EM-jet energy, the right panel of Fig. 3.5 shows a two-dimensional profile plot between the EM-jet energy in detector-level and particle-level. The linear fit is

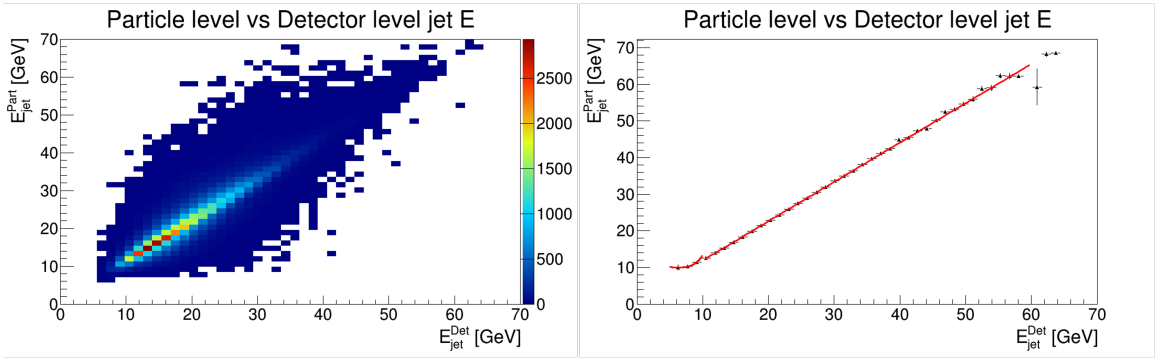

Figure 3.5: (left) The 2D plot for the distribution of particle-level FMS EM-jet energy vs the matched detector-level EM-jet energy in the simulation. (right) The 2D profile plot between the EM-jet energy at the detector level and the particle level, with polynomial fits.

applied to fit the points in the high-energy range, while the 6th-order polynomial fit is used to fit the low-energy range. Given an energy value for the detector-level EM-jet, these fits are used to determine the corresponding particle-level EM-jet energy.

The above shows the EM-jet correction for the Run 15 dataset. The steps for studying the EM-jet correction for the Run 17 dataset are similar; however, the center-of-mass energy for the particle-level simulation with Pythia 6 is 510 GeV.

3.1.3 BBC East Veto Cuts

The BBC east veto cuts serve two major purposes for single diffractive events: to minimize accidental coincidence (AC) events, also known as multiple collision events, and to determine the rapidity gap. The AC events occur when the RP detects the protons coming from one collision or from elastic scattering events, but the EM-jet at FMS comes from another collision. This could happen because the trigger rate of the FMS is much faster than the other major detectors (like TPC) at STAR. The AC events typically exhibit higher ADC sum values at the BBC because more hits from particles in multiple collision events

are accumulated on the BBC. Furthermore, the rapidity gap, one of the characteristics of the single diffractive event in the experiment[41], can be determined from the BBC east veto in this analysis. The pseudorapidity coverage of the east side BBC is about a unit of 3, which could roughly satisfy the rapidity gap requirement at these mid-energy collisions.

The study of BBC East veto cuts is carried out simultaneously with the East RP track cut study, detailed in Sec. 3.1.4. Here is a detailed exploration of the BBC East veto cuts using the Run 15 dataset. To begin with, a rough cut is applied to a small BBC East ADC sum of less than < 150 to eliminate some of the AC backgrounds. Then, with the rough BBC East ADC sum cut, East RP θ_X and θ_Y distributions for East RP track with different ξ ranges are checked, where ξ is the fraction of proton momentum loss in the collision, $\xi = \frac{p_{beam} - p_{proton}}{p_{beam}}$, and θ_X (θ_Y) is the East RP track polar angle component in x- (y-) direction. The goal of checking the rough East RP θ_X and θ_Y distributions is to figure out the rough East RP θ_X and θ_Y cuts and to use them to reduce the background further to determine the BBC East veto cuts. Figure 3.6 shows rough East RP θ_X and θ_Y distributions for three different East RP ξ regions. Based on the hot areas for each figure, which are indicated in red and yellow colors, we determine the rough cut for East RP, specifically θ_X and θ_Y. Then, with the rough East RP θ_X and θ_Y cuts applied, we explore the small/large BBC east ADC sum distributions to determine the cuts on small/large BBC East. The left panel of Fig. 3.7 shows the small BBC East ADC sum distribution, while the right panel of Fig. 3.7 shows the large BBC East ADC sum distribution. According to Fig. 3.7, we choose the small BBC East ADC sum < 90 and the large BBC East ADC sum < 80 as BBC East veto cuts for the Run 15 dataset.

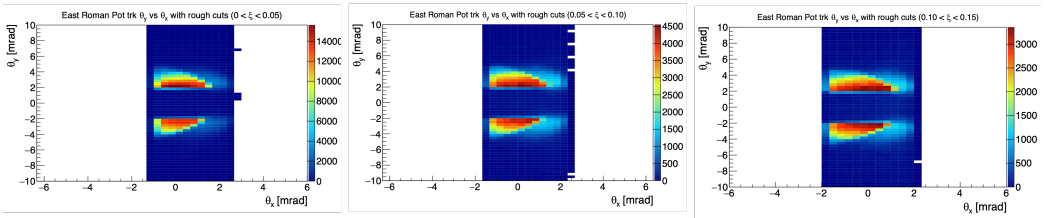

Figure 3.6: East RP θ_X and θ_Y distributions for three different East RP track ξ ranges ($0 < \xi < 0.05$ (left); $0.05 < \xi < 0.1$ (middle); $0.1 < \xi < 0.15$ (right)) with only applying BBC East ADC sum < 150.

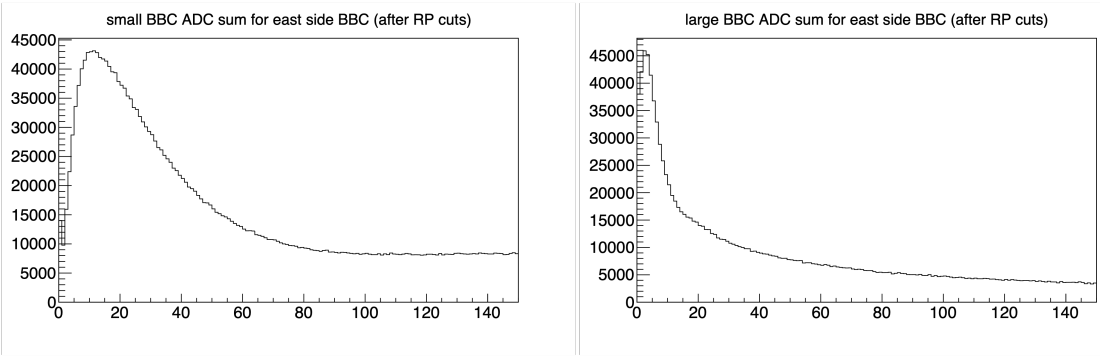

Figure 3.7: The small (left) and large (right) BBC East ADC sum distribution after the rough East RP θ_X and θ_Y cuts for the Run 15 dataset.

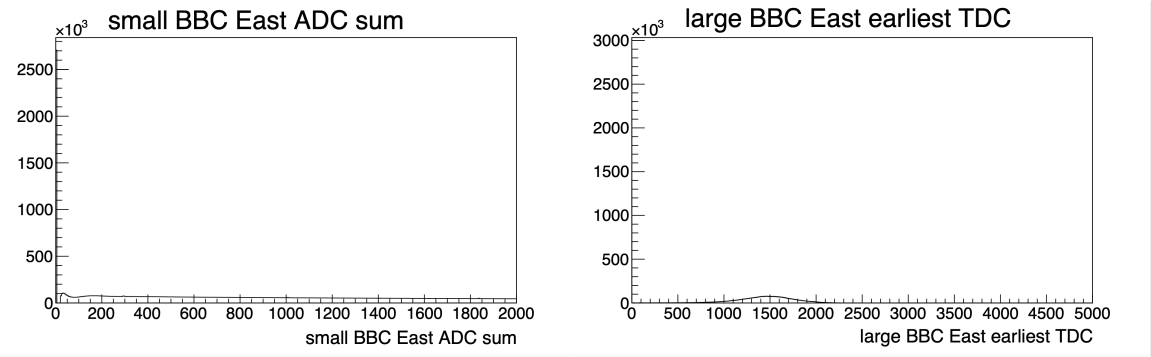

Figure 3.8: The small BBC East ADC sum distribution (left) and the large BBC East earliest TDC distribution (right) after the rough East RP θ_X and θ_Y cuts for the Run 17 dataset.

The BBC East veto cuts for the Run 17 dataset are examined using a similar approach to that employed for the Run 15 dataset. The small BBC East ADC sum cut is < 80 for the Run 17 dataset, where the distribution is shown in the left panel of Fig. 3.8. However, in the Run 17 dataset, no information is available on the large BBC East ADC sum. Therefore, to determine the veto on the large BBC East region, the large BBC East earliest TDC value is used, with the distribution shown in the right panel of Fig. 3.8. Such a value is non-zero when there are any hits on the large BBC East. Following this idea, we only accept the veto in the large BBC East region with the large BBC East earliest TDC value < 30, allowing for the resolution of the detector.

3.1.4 East Roman Pot (RP) Track Cuts

After exploring and applying BBC East veto cuts, the next set of cuts are East Roman Pot (RP) track cuts. The major goals for the East RP track cuts are to identify reasonable proton tracks that hit the RP and select the single diffractive events from proton tracks.

To begin with, in order to select the single diffractive events, only one East RP track per event is accepted. However, there is no requirement on the West RP track for the single diffractive events. Then, to ensure that the East RP track is appropriately reconstructed, it must hit more than six silicon planes. Furthermore, according to the requirement for the proton in the single diffractive events in [41], the East proton momentum loss fraction is required to be within the range of $0 < \xi < 0.15$. These cuts are the same for both analyses using the Run 15 dataset and the Run 17 dataset.

The cuts regarding the East RP track kinematics are then considered. The East RP track kinematic cuts for the Run 15 dataset are explained in detail as an example. First, the East RP track distributions of θ_X and θ_Y are further explored. Figure 3.9 shows the East RP track θ_X and θ_Y distributions for three ξ ranges. The hot area will be considered as acceptable final East RP θ_X and θ_Y cuts. The final East RP track θ_Y cuts are uniform for all three ξ ranges: $2 < |\theta_Y| < 4$ mrad. However, the final East RP track θ_X cuts are ξ dependent, shown in Tab. 3.2. Finally, with then the final East RP θ_X and θ_Y cuts applied, the East RP track p_X and p_Y distributions are also explored, where p_X and p_Y are the x- and y-component of the momentum of the East RP track. Figure 5.6 shows the East RP track p_X and p_Y distributions for three ξ ranges. Holding a similar idea on choosing the hot regions for the East RP track p_X and p_Y, the shape of a rectangle with a quarter circle is used to determine the final East RP track p_X and p_Y cuts. The expressions are detailed in Tab. 3.3.

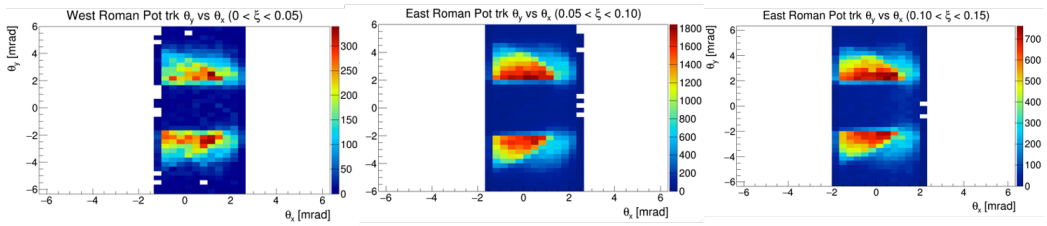

Figure 3.9: East RP track θ_X and θ_Y distributions for three East RP track ξ ranges ($0 < \xi < 0.05$ (left); $0.05 < \xi < 0.1$ (middle); $0.1 < \xi < 0.15$ (right)) for the Run 15 dataset.

East RP track ξ range	θ_X final cuts [mrad]
$0.00 < \xi < 0.05$	$-1.0 < \theta_X < 1.5$
$0.05 < \xi < 0.10$	$-1.25 < \theta_X < 1.25$
$0.10 < \xi < 0.15$	$-1.5 < \theta_X < 1.25$

Table 3.2: Final cuts for East RP track θ_X by three ξ regions for the Run 15 dataset.

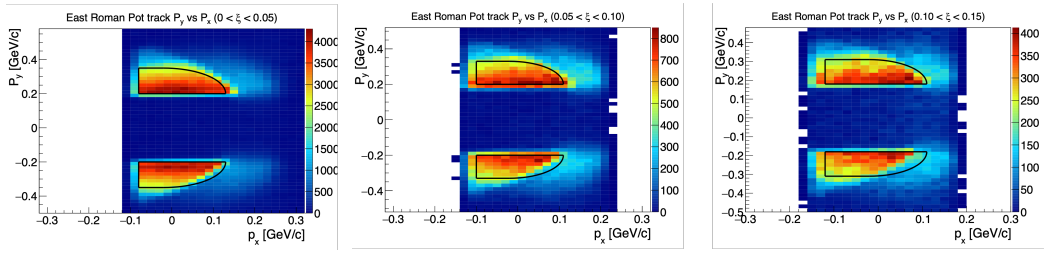

Figure 3.10: East RP track p_X and p_Y distributions for three East RP track ξ ranges ($0 < \xi < 0.05$ (left); $0.05 < \xi < 0.1$ (middle); $0.1 < \xi < 0.15$ (right)) for the Run 15 dataset. The black curves indicate the ranges of accepted East RP track p_X and p_Y cuts.

ξ range	p_X and p_Y final cuts [GeV/c]
$0.00 < \xi < 0.05$	$(p_X + 0.02)^2 + (\lvert p_Y \rvert - 0.2)^2 < 0.15^2$ or $-0.08 < p_X < -0.02$ and $0.2 < \lvert p_Y \rvert < 0.35$
$0.05 < \xi < 0.10$	$(p_X + 0.02)^2 + (\lvert p_Y \rvert - 0.2)^2 < 0.13^2$ or $-0.10 < p_X < -0.02$ and $0.2 < \lvert p_Y \rvert < 0.33$
$0.10 < \xi < 0.15$	$(p_X + 0.02)^2 + (\lvert p_Y \rvert - 0.18)^2 < 0.13^2$ or $-0.12 < p_X < -0.02$ and $0.18 < \lvert p_Y \rvert < 0.31$

Table 3.3: East RP track p_X and p_Y final cuts for the Run 15 dataset

The study of East RP track kinematic cuts for the Run 17 dataset follows a similar approach to that for the Run 15 dataset. The distributions of the East RP track θ_X and θ_Y distributions are shown in Fig. 3.11. In the figure, the final θ_Y cuts are uniform for all three ξ ranges: $1.25 < |\theta_Y| < 3$ mrad. The final East RP track θ_X cuts are ξ dependent, shown in Tab. 3.4. Then, the distributions of the East RP track p_X and p_Y are shown in Fig. 5.8, as well as the final East RP track θ_X and θ_Y cuts shown in Tab. 3.5.

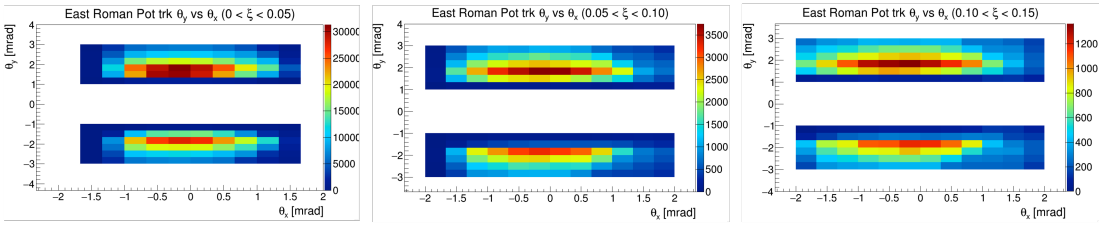

Figure 3.11: East RP track θ_X and θ_Y distributions for three East RP track ξ ranges ($0 < \xi < 0.05$ (left); $0.05 < \xi < 0.1$ (middle); $0.1 < \xi < 0.15$ (right)) for the Run 17 dataset.

East RP track ξ range	θ_X final cuts [mrad]
$0.00 < \xi < 0.05$	$-1.0 < \theta_X < 1.25$
$0.05 < \xi < 0.10$	$-1.25 < \theta_X < 1.25$
$0.10 < \xi < 0.15$	$-1.5 < \theta_X < 1.25$

Table 3.4: Final cuts for East RP track θ_X by three ξ regions for the Run 17 dataset.

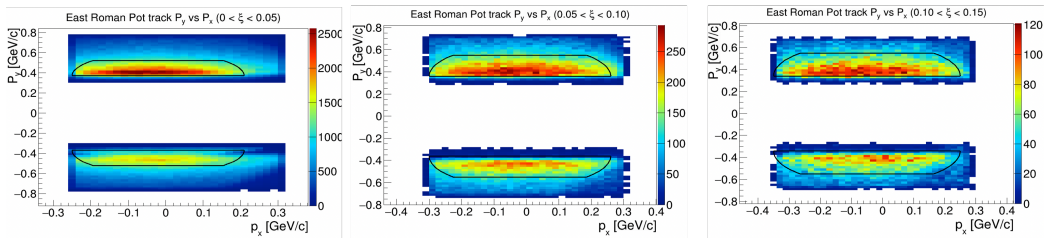

Figure 3.12: East RP track p_X and p_Y distributions for three East RP track ξ ranges ($0 < \xi < 0.05$ (left); $0.05 < \xi < 0.1$ (middle); $0.1 < \xi < 0.15$ (right)) for the Run 17 dataset. The black curves indicate the ranges of accepted East RP track p_X and p_Y cuts.

ξ range	p_X and p_Y final cuts [GeV/c]
$0.00 < \xi < 0.05$	$(p_X + 0.02)^2 + (\lvert p_Y \rvert - 0.37)^2 < 0.23^2$ and $0.37 < \lvert p_Y \rvert < 0.52$
$0.05 < \xi < 0.10$	$(p_X + 0.02)^2 + (\lvert p_Y \rvert - 0.36)^2 < 0.28^2$ and $0.36 < \lvert p_Y \rvert < 0.55$
$0.10 < \xi < 0.15$	$(p_X + 0.05)^2 + (\lvert p_Y \rvert - 0.34)^2 < 0.30^2$ and $0.34 < \lvert p_Y \rvert < 0.55$

Table 3.5: East RP track p_X and p_Y final cuts for the Run 17 dataset.

3.2 Background Study

After the event selection criteria for the single diffractive events, there might be a fraction of the background contamination in the single diffractive events. In this section, the fraction of the background in the single diffractive events is explored.

The dataset used to estimate the background is from the same collisions, but with the minimum bias trigger applied. This dataset is called the zerobias dataset. The minimum bias trigger is the trigger with the minimum threshold set for the STAR detectors. With the minimum bias trigger set up, the number of events passing such a trigger is enormous. The events passing the minimum bias triggers are highly pre-scaled before being filled into the zerobias dataset. In the zerobias dataset, it is less likely that there are single diffractive events for this analysis because the coincidence for the events with FMS is low. Therefore, the zerobias dataset can be used to estimate the background for the single diffractive events.

To begin with, the zerobias dataset is obtained and checked for the number of events when the cuts for FMS, RP, and BBC detectors are not required. Then, the same event selection criteria for BBC East veto cuts (see Sec. 3.1.3) and East RP track cuts (see

Sec. 3.1.4) are applied, and the number of events is checked later on. Only about 0.20% of the events in the zerobias dataset pass these event selection criteria for the Run 15 dataset, while this fraction is about 0.37% for the Run 17 dataset. Such backgrounds are mostly accidental coincidence (AC) backgrounds for the single diffractive process without any bias.

The calculation of the AC background for the measured single diffractive events is shown in Eq. 3.1. In this equation, n_{AC} is the number of the AC events, which is difficult to count directly. n_{mea} is the number of event counts per x_F bin in the asymmetry calculation for the measured single diffractive events. n_{RG} is the number of event counts per x_F bin in the asymmetry calculation for the RG events, where the description for RG events is in Chap. 4. $\frac{n_{AC}}{n_{RG}}$ can be considered as the fraction of AC events for RG events, which is about 0.20% (0.37%) for the Run 15 dataset (the Run 17 dataset). By counting the events per x_F bin for measured single diffractive events and RG events, the fraction for the AC events is about 1.8% (5.5%) for each x_F bin for the Run 15 dataset (the Run 17 dataset). Therefore, the purity of the single diffractive events, the fraction of the real single diffractive events to the measured single diffractive events, is about 98.2% (94.5%) for each x_F bin for the Run 15 dataset (the Run 17 dataset).

$$frac_{bkg} = \frac{n_{AC}}{n_{mea}} = \frac{n_{AC}}{n_{RG}} \times \frac{n_{RG}}{n_{mea}} \tag{3.1}$$

The effect of the measured transverse single-spin asymmetry (A_N) from the AC background is assigned to the systematic uncertainty because the AC background fraction is low. The detailed calculation is shown as follows. First of all, the A_N is corrected based on Eq. 3.2. $A_N(sig)$ is the corrected A_N, while $A_N(mea)$ is the measured A_N which contains the effect of AC events. $frac(sig)$ is the signal fraction, while $frac(bkg)$ is the

AC background fraction. The error propagation for Eq. 3.2 is expressed in Eq. 3.3. Since the AC background fraction and its uncertainty are very small, the second and third terms are negligible. Therefore, only the first term related to the statistical uncertainty of the measured asymmetry is kept, assigned to the systematic uncertainty.

$$A_N(sig) = \frac{A_N(mea) - frac(bkg) * A_N(bkg)}{frac(sig)} = \frac{A_N(mea) - frac(bkg) * A_N(bkg)}{1 - frac(bkg)} \tag{3.2}$$

$$\begin{aligned}
\sigma^2 &= \left(\frac{\partial A_N(sig)}{\partial A_N(mea)}\right)^2 \sigma A_N^2(mea) + \left(\frac{\partial A_N(sig)}{\partial frac(bkg)}\right)^2 \sigma frac^2(bkg) + \left(\frac{\partial A_N(sig)}{\partial A_N(bkg)}\right)^2 \sigma A_N^2(bkg) \\
&= \left(\frac{1}{1 - frac(bkg)}\right)^2 \sigma A_N^2(mea) + \left(\frac{A_N(sig)}{1 - frac(bkg)}\right)^2 \sigma frac^2(bkg) \\
&+ \left(\frac{frac(bkg)}{1 - frac(bkg)}\right)^2 \sigma A_N^2(bkg) \\
&= \left(\frac{1}{frac(sig)}\right)^2 \sigma A_N^2(mea) + \left(\frac{A_N(sig)}{frac(sig)}\right)^2 \sigma frac^2(bkg) + \left(\frac{frac(bkg)}{frac(sig)}\right)^2 \sigma A_N^2(bkg) \\
&\approx \left(\frac{1}{frac(sig)}\right)^2 \sigma A_N^2(mea)
\end{aligned} \tag{3.3}$$

3.3 Cross-ratio Method

In these analyses mentioned in this dissertation, the cross-ratio method is used to extract the A_N. Equation 3.4 and Equation 3.5 show the formulas for the cross-ratio method. In both equations, ϵ stands for the raw asymmetry. $N^{\uparrow(\downarrow)}(\phi)$, $N^{\uparrow(\downarrow)}(\phi+\pi)$ are the yields detected at ϕ, $(\phi+\pi)$ for spin up (down) state, where ϕ is the azimuthal angle of the EM-jet reconstructed at the FMS in the lab frame respect to the beam direction. For these analyses, the full 2π azimuthal coverage is split into 16 ranges. It is noted that definitions

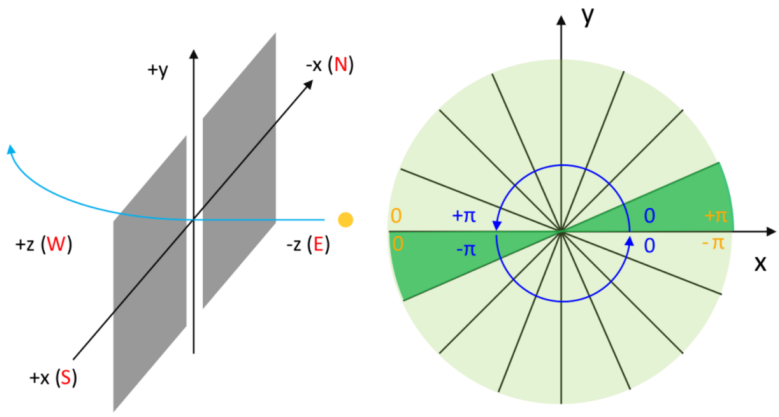

Figure 3.13: Schematic diagram for defining the x- and y-coordinates (left), as well as the ϕ regions (right) with respect to two different polarized proton beam directions: blue beam (blue color) and yellow beam (yellow color).

for the ϕ in the blue beam and the yellow beam directions are different in the local STAR frame, with details shown in Fig. 3.13. P is the average polarization of the proton beam for all the events after the event selection for the entire dataset, which is about 56% for the Run 15 dataset and about 58% for the Run 17 dataset, respectively.

$$\epsilon = \frac{\sqrt{N^{\uparrow}(\phi)N^{\downarrow}(\phi+\pi)} - \sqrt{N^{\downarrow}(\phi)N^{\uparrow}(\phi+\pi)}}{\sqrt{N^{\uparrow}(\phi)N^{\downarrow}(\phi+\pi)} + \sqrt{N^{\downarrow}(\phi)N^{\uparrow}(\phi+\pi)}} \tag{3.4}$$

$$\epsilon = PA_N cos(\phi) \tag{3.5}$$

Then, a cosine fit $(p_0\cos(\phi)+p_1)$ is applied to the entire dataset after all the event selection criteria to extract the A_N from the raw asymmetry in Eq. 3.5. The constant term p_1 could provide a cross-check for possible unidentified asymmetry, while these analyses do not take it into account. Figure 3.14 shows one example for the raw asymmetry extraction with the cosine fit applied.

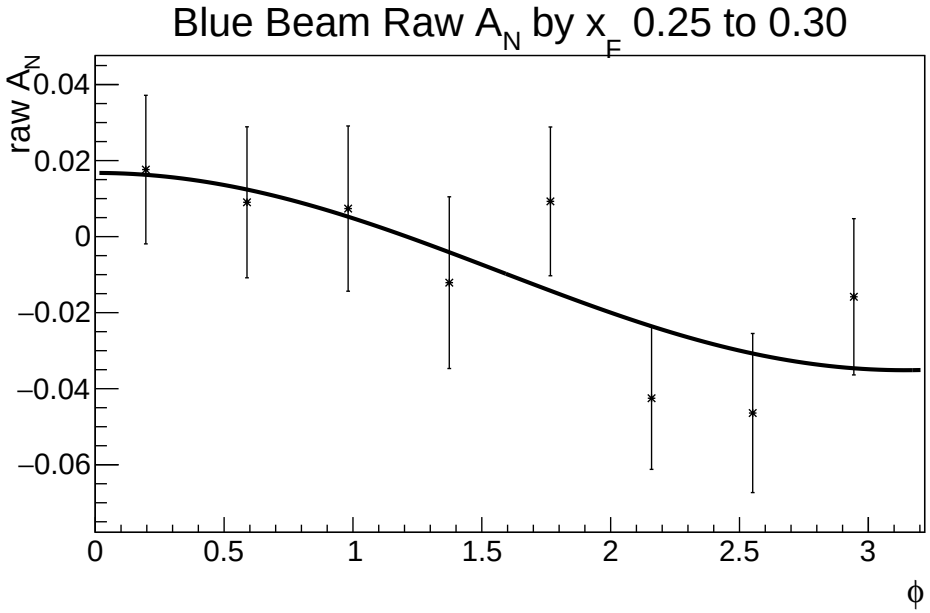

Figure 3.14: Example of the raw asymmetry extraction with the cosine fit. It is the fit for calculating the raw asymmetry for single diffractive EM-jet A_N with all photon multiplicity at the EM-jet $0.25 < x_F < 0.30$.

To check the quality of the cosine fit, the χ^2 distribution for all the fits for all the A_N analyses mentioned in this dissertation is plotted. The left panel of Fig. 3.15 shows the χ^2 distribution for all the fits with the Run 15 dataset, while the right panel of Fig. 3.15 shows the χ^2 distribution for all the fits with the Run 17 dataset. The χ^2 probability distribution with degree of freedom equal to 6 for these analyses is also included in the figure. The χ^2 value from the fit for the analyses with the Run 15 dataset mostly matches the χ^2 probability distribution. However, for the analyses in the Run 17 dataset, the χ^2 value from the fit is partially matched with the χ^2 probability distribution.

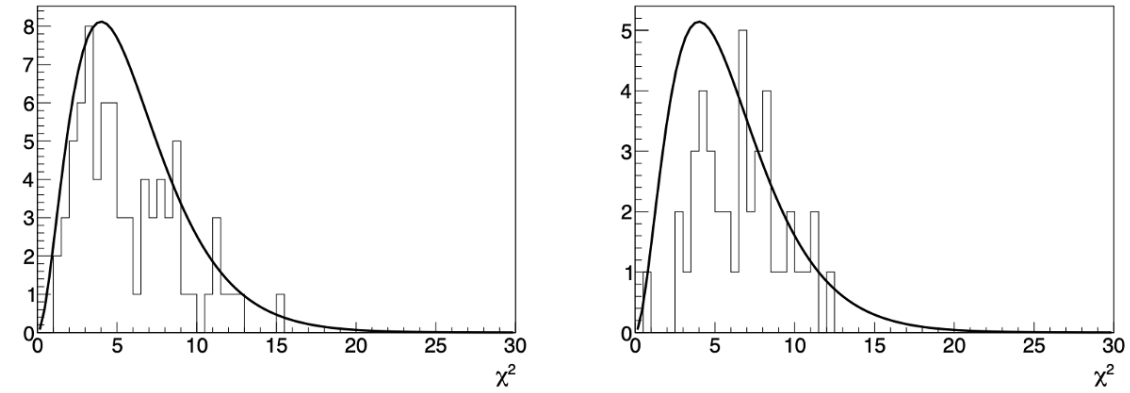

Figure 3.15: χ^2 distribution for all the fits with Run 15 dataset (left) and with Run 17 dataset (right). The χ^2 probability distribution with degrees of freedom equal to 6 is also shown in the curve.

This method leverages the FMS detector's azimuthal symmetry to cancel out effects caused by non-uniform detector efficiency and time-dependent luminosity for the dataset.

3.4 Systematic Uncertainty

The systematic uncertainty for A_N in single diffractive events includes the cuts on the BBC East veto, the Ring of Fire, and the accidental coincidence (AC) background. The approach to calculating the systematic uncertainty for the BBC East veto cuts and Ring of Fire is mentioned below. The AC background is estimated in Sec. 3.2. The final systematic uncertainty for the A_N results is calculated individually for every x_F bin. They are calculated as $\sqrt{\sum_i \sigma_i^2}$, where i is each term for systematic uncertainty for cuts on BBC East veto, Ring of Fire, and AC background. Furthermore, the systematic uncertainty of the polarization is also explored.

3.4.1 Systematic uncertainty for the BBC East veto cuts

The systematic uncertainty for the BBC East veto cuts is investigated by varying the cut values and exploring their effects on the A_N results. Cut values changed for studying the systematic uncertainty are listed as follows:

- Small BBC East ADC sum cut for the Run 15 dataset: choose four different cut values: < 70, < 80, < 100, < 110.
- Large BBC East ADC sum cut for the Run 15 dataset: choose four different cut values: < 60, < 70, < 90, < 100.
- Small BBC East ADC sum cut for the Run 17 dataset: choose four different cut values: < 60, < 70, < 90, < 100.
- Large BBC East earliest TDC cut for the Run 17 dataset: choose four different cut values: $= 0$, < 15, < 60, < 120.

The systematic uncertainty for studying the Small BBC East cuts and Large BBC East cuts is explored independently. For each of the cuts, the A_N and its statistical uncertainty are collected.

The impact of varying the cut is evaluated to determine whether the effect is significant enough to be included as a source of systematic uncertainty. This assessment is performed using the Bayesian method introduced in Ref. [83]. For each EM-jet x_F bin for each type of cuts, the standard deviation is calculated based on the A_N obtained with the nominal cut value and with the varied cut values. The cut with variations produces a maximum value with statistical uncertainty $A_N(1) \pm \delta_1$ and a minimum value with statistical

uncertainty $A_N(2) \pm \delta_2$, respectively. Only when $\frac{|A_N(1)-A_N(2)|}{\sqrt{|\delta_1^2-\delta_2^2|}} > 1$ the standard variation will be used for this systematic uncertainty term, otherwise such term of systematic uncertainty term will be set 0 [83]. This procedure, commonly referred to as the Barlow check, provides a quantitative criterion for determining whether variations in a specific cut should be included in the systematic uncertainty.

3.4.2 Ring of Fire

The Ring of Fire is a kind of background related to the FMS-sm-bs3 trigger, and its effect is taken into account as systematic uncertainty for the Run 15 dataset. This trigger is targeted at the inner region of FMS, which is close to the beam. The pre-scale factor of the FMS-sm-bs3 trigger is the smallest among the FMS small board sum triggers. Furthermore, the FMS-sm-bs3 trigger threshold is not high enough to fully minimize the background from the beam remnant for the Run 15 dataset. However, for the Run 17 dataset, the Ring of Fire background is small because the FMS-sm-bs3 trigger threshold for the Run 17 dataset is much higher than that for the Run 15 dataset, which can highly minimize the effect due to the beam remnant background. Therefore, it is not necessary to consider the Ring of Fire as systematic uncertainty for the Run 17 dataset.

To investigate the effect of the Ring of Fire on the Run 15 dataset, the A_N value, along with its statistical uncertainty, is studied when the FMS-sm-bs3 trigger is included/excluded. The standard deviation is also calculated for these two situations. Additionally, the Barlow check is applied to determine whether to assign the systematic uncertainty as well.

3.4.3 Polarization Uncertainty

In the cross-ratio method, the polarization values of the blue beam and the yellow beam are used to calculate the A_N results. Therefore, it is necessary to calculate the polarization uncertainty. The polarization measurement results for both beams are provided by the CNI group at the RHIC. The results are listed in the table on the webpage [84] for the Run 15 dataset and the webpage [85] for the Run 17 dataset. In the webpage, the starting time (t_0), the polarization of the blue (yellow) beam at the beginning of every fill (P_0), and the decay rate ($\frac{dP}{dt}$) are provided for each fill. For each event, the beam polarization can be calculated from the time difference from the beginning of the fill using Eq. 3.6, where t_{event} is the time of each event. The beam polarization for each run can be calculated by Eq. 3.7, where t_{run} is the time of the center of the run. The beam polarization for each fill can be calculated using the weighted average run polarization with Eq. 3.8, where L_{run} is the luminosity of each run. However, since L_{run} is proportional to the number of events in each run, the luminosity of each run can be replaced by the number of events in each run in the calculation as estimation.

$$P_{event} = P_0 + \frac{dP}{dt}(t_{event} - t_0) \tag{3.6}$$

$$P_{run} = P_0 + \frac{dP}{dt}(t_{run} - t_0) \tag{3.7}$$

$$P_{fill} = \frac{\sum_{run} L_{run} P_{run}}{\sum_{run} L_{run}} \tag{3.8}$$

According to [86], the beam polarization uncertainty includes the scale uncertainty,

fill-to-fill uncertainty, and uncertainty from the profile correction procedure. The scale uncertainty is related to the polarization measurement methods, including H-jet scale, H-jet background, and pC scale. For the Run 15 dataset, the scale uncertainty is 3%; while for the Run 17 dataset, the scale uncertainty is 1.1% [86]. Additionally, the relative uncertainty of the profile correction for a single beam in a single fill is 2.2%. For a set of M fills in a dataset, the relative profile correction for the single-spin asymmetry measurement is $\sigma(profile)/P = 2.2\%/\sqrt{M}$ [86]. The uncertainty from the profile correction procedure is approximately 0.3% and approximately 0.17% for the Run 15 dataset and for the Run 17 dataset, respectively.

The fill-to-fill uncertainty is propagated based on Eq. 3.8 with the uncertainty of P_0 and $\frac{dP}{dt}$. Details for the propagation can be found in [87]. The uncertainty for these two terms, $\sigma(P_0)$ and $\sigma(\frac{dP}{dt})$, of either the blue beam or the yellow beam can be obtained in the RHIC polarization result table. This fill-to-fill uncertainty can be expressed in Eq. 3.9. The third term on the right side of the equation is due to the sensitivity of the measurement of the energy scale of the nuclei in the pC polarimetry, and the value is negligible. However, for the term shown in Eq. 3.10, this correction overcounts the measurement using a fraction of the run period. Therefore, a correction scale factor $\sqrt{1-\frac{N}{M}}$ is applied for the second term, which is shown in Eq. 3.11. For the Run 15 dataset, N=54 and M=142; while N=179 and M=190 for the Run 17 dataset. The fill-to-fill uncertainty for single diffractive EM-jet analysis is about 0.3% and 0.06% for the Run 15 dataset and the Run 17 dataset, respectively.

$$\sigma^2(P_{fill}) = \sigma^2(P_0)+\sigma^2\left(\frac{dP}{dt}\right)\cdot\left(\frac{\sum_{run} t_{run}L_{run}}{L_{fill}} - t_0\right)^2+\left(\frac{\sigma(fill-to-fill)}{P}\right)^2\cdot P_{fill}^2 \quad (3.9)$$

$$P_{set}^2 = \frac{\sum_{run} t_{run}L_{run}}{L_{fill}} \quad (3.10)$$

$$P_{fill-to-fill\ scale}^2 = \left(1-\frac{N}{M}\right)\cdot P_{set}^2 \quad (3.11)$$

In summary, the polarization uncertainty is calculated in the quadrature. The polarization uncertainty is approximately 3.0% and approximately 1.1% for the Run 15 dataset and for the Run 17 dataset, respectively. However, since the polarization uncertainty for each fill is different, such polarization uncertainty is not included in the systematic uncertainty for the A_N measurement. Instead, the polarization uncertainty is listed separately in the measured A_N plots.

3.5 Cross-section Fraction Study

The fraction of the single diffractive event cross-section to the inclusive event cross-section is investigated. This study can provide evidence to develop theories to understand the underlying mechanism for the A_N in the single diffractive events.

The cross-section fraction mentioned in this dissertation is expressed as $\frac{\sigma_{SD}}{\sigma_{inc}}$. σ_{SD} is the cross-section for single diffractive events in the forward region, and is calculated in Eq. 3.12. σ_{inc} is the cross-section for inclusive events in the forward region, and is calculated in Eq. 3.13. N_{SD} and N_{inc} denote the yields of single diffractive events and inclusive events,

respectively. It is important to note that the inclusive event yields are counted only for the runs used in the single diffractive analysis. ε_{RP} and ε_{BBC} are the Roman Pot efficiency and BBC efficiency, respectively. The "purity" term represents the fraction of true single diffractive events in the measured sample, determined from the background study in Sec. 3.2. ε_{FMS} denotes as FMS efficiency, $\varepsilon_{trigger}$ denotes as efficiency for the STAR trigger system, $\mathcal{L}$ denotes as integrated luminosity. In practice, it is difficult to calculate ε_{FMS} and $\varepsilon_{trigger}$, and $\mathcal{L}$. Therefore, the absolute cross-section, σ_{SD} and σ_{inc}, for either type of events are not calculated. Instead, we assume that the FMS and trigger efficiencies, as well as the integrated luminosity, are identical for both event categories. Under this assumption, these factors cancel in the ratio, and the cross-section fraction can be calculated using Eq. 3.14.

$$\sigma_{SD} = \frac{N_{SD} \times purity}{\mathcal{L} \times \varepsilon_{RP} \times \varepsilon_{BBC} \times \varepsilon_{FMS} \times \varepsilon_{trigger}} \tag{3.12}$$

$$\sigma_{inc} = \frac{N_{inc}}{\mathcal{L} \times \varepsilon_{FMS} \times \varepsilon_{trigger}} \tag{3.13}$$

$$\frac{\sigma_{SD}}{\sigma_{inc}} = \frac{N_{SD} \times purity}{N_{inc} \times \varepsilon_{RP} \times \varepsilon_{BBC}} \tag{3.14}$$

The RP efficiency is estimated using simulations of single diffractive events. At the particle level, events are generated with Pythia8 [88], while the detector-level response is modeled with the RP detector simulation (pp2pp) [68]. The RP efficiency is defined as the ratio of the number of events containing a good east RP track after detector-level simulation to the number of events containing any proton on the east side in the particle-level simulation. Both the good east RP track in the RP simulation and the proton track

in the particle level simulation are required to be within $0 < \xi < 0.15$. Following this procedure, the RP efficiency is determined to be approximately 11.4%. The corresponding relative systematic uncertainty is estimated to be 6.5% based on [68].

The BBC efficiency is estimated using the simulations for single diffractive events with Pythia8 at the particle level [88] and the simulation with STAR detectors, including the BBC detectors, at the detector level with Geant3. This efficiency can be calculated by the fraction of the events passing the BBC East veto cuts (detail in Sec. 3.1.3) at the detector level to all the events with an east proton intact at the particle level. The BBC efficiency is about 99.9%. The relative systematic uncertainty for the BBC efficiency is 10%, based on [89].

The overall cross-section fraction is $0.672\% \pm 0.080\%$ for the Run 15 dataset. The differential cross-section fraction is studied as a function of EM-jet x_F region for the Run 15 dataset, shown in Fig. 3.16. From either the overall cross-section fraction or the differential cross-section fraction results, the single diffractive event cross-section is very small compared to the inclusive event cross-section in the forward region, which shows that single diffractive events can not have a significant contribution to the large A_N in inclusive events.

The cross-section fraction study for the Run 17 dataset is still ongoing. However, based on the cross-section fraction results from the Run 15 dataset, the cross-section fraction for the Run 17 dataset remains small. Similar conclusions can be drawn with the Run 17 dataset.

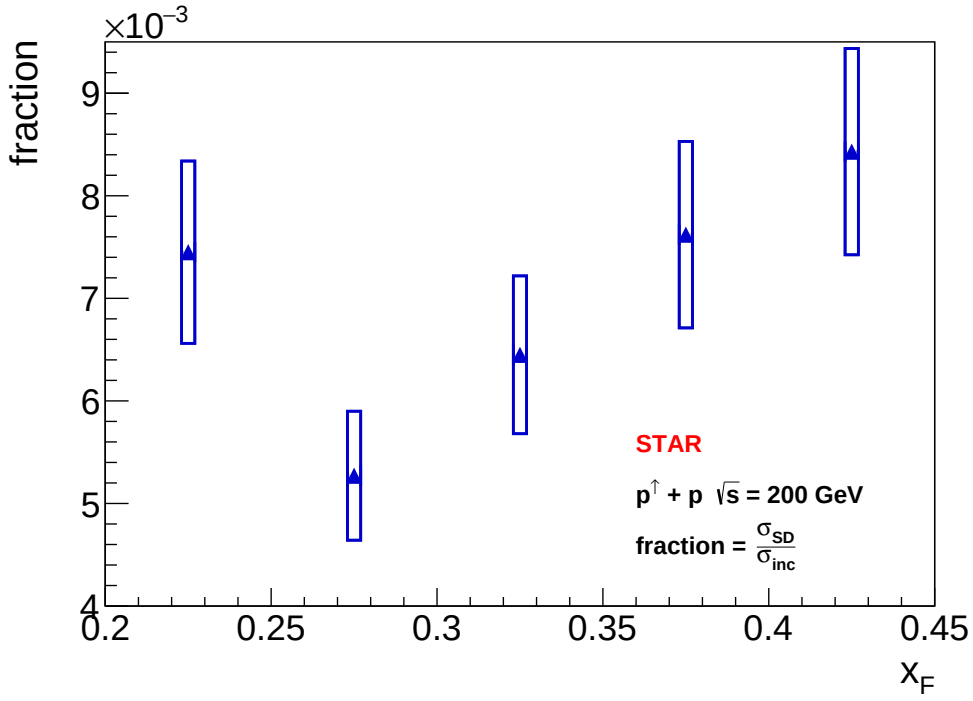

Figure 3.16: Cross-section fraction of the single diffractive process (σ_{SD}) to the inclusive process (σ_{inc}) as a function of x_F for the Run 15 dataset.

3.6 Transverse Single-spin Asymmetry for Single Diffractive Events in $\sqrt{s} = 200$ GeV and 510 GeV

In this study, the transverse single-spin asymmetry (A_N) is explored for both the Run 15 dataset and the Run 17 dataset, considering three different cases of photon multiplicity: all-photon multiplicity, only one- or two-photon multiplicity, and three- or more-photon multiplicity. Photon multiplicity refers to the number of photons inside an EM-jet.

Figure 3.17 shows the A_N of the single diffractive EM-jet as a function of x_F for three cases of photon multiplicity mentioned above in $p^{\uparrow} + p$ collisions at $\sqrt{s} = 200$ GeV with Run 15 dataset. The figure considers five EM-jet x_F regions ranging from 0.20 to 0.45. Among the three panels in the figure, the blue points are for the blue beam A_N, represented as $x_F > 0$, which corresponds to A_N for the polarized beam direction pointing to the front of the FMS (blue beam); while the red points are for the yellow beam A_N, represented as $x_F < 0$, corresponding to the A_N for the yellow beam with the beam direction to the back of the FMS. The yellow beam A_N serves as the cross check, and it is consistent with zero as expected.

An overall non-zero significant test is applied for the three photon multiplicity cases. A constant fit is used among the five data points in each of the photon multiplicity cases. The ratio of the constant term value from the fit to its uncertainty is considered a non-zero significant value. Table 3.6 shows results for single diffractive EM-jet A_N for each photon multiplicity case in $p^{\uparrow} + p$ collisions at $\sqrt{s} = 200$ GeV.

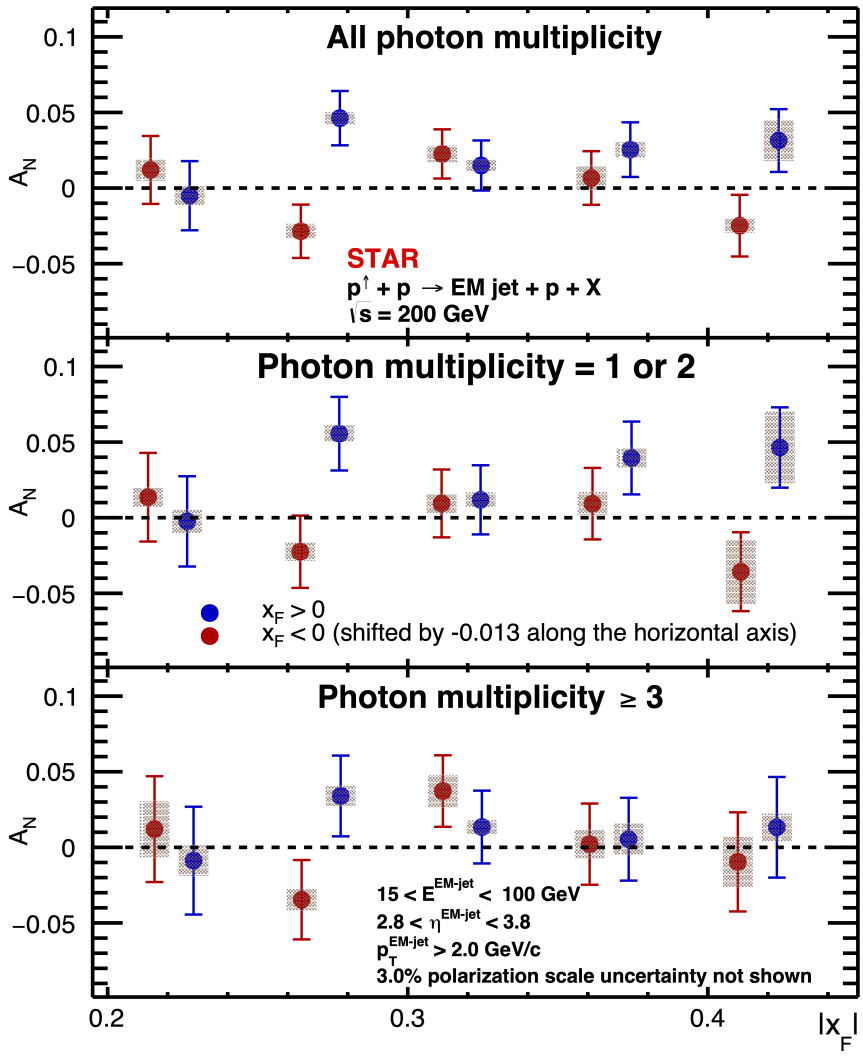

Figure 3.17: Transverse single-spin asymmetry for single diffractive events as a function of x_F with $p^{\uparrow} + p$ collisions at $\sqrt{s} = 200$ GeV for three different photon multiplicity cases: all photon multiplicity (top), one- or two-photon multiplicity (middle), and three- or more-photon multiplicity (bottom). The A_N for $x_F > 0$ are shown in blue points. The A_N for $x_F < 0$ (red points) shifts -0.013 along the x-axis.

Photon multiplicity case	Constant fit result	n-σ significant
All photon multiplicity	0.024 ± 0.009	2.7
One- or two-photon multiplicity	0.030 ± 0.012	2.5
Three- or more-photon multiplicity	0.014 ± 0.013	1.0

Table 3.6: n-σ significant for each photon multiplicity case for $x_F > 0$ for single diffractive events in $\sqrt{s} = 200$ GeV

Photon multiplicity case	Constant fit result	n-σ significant
All photon multiplicity	0.014 ± 0.005	2.6
One- or two-photon multiplicity	0.025 ± 0.009	2.8
Three- or more-photon multiplicity	0.006 ± 0.007	0.8

Table 3.7: n-σ significant for each photon multiplicity case for $x_F > 0$ for single diffractive events in $\sqrt{s} = 510$ GeV

In addition, the single diffractive EM-jet A_N with $p^{\uparrow} + p$ collisions at $\sqrt{s} = 510$ GeV with the Run 17 dataset is studied, shown in Fig. 3.18. The results are explored with the same three cases of photon multiplicity as for the Run 15 dataset. With the higher $\sqrt{s}$ collisions, the EM-jet A_N for the lower x_F regions can be explored, with the ranges of $0.10 < x_F < 0.35$. The n-σ non-zero significance is checked for these results with three photon multiplicity cases, using the same method as for the study in the Run 15 dataset. The n-σ non-zero significance results are shown in Tab. 3.7.

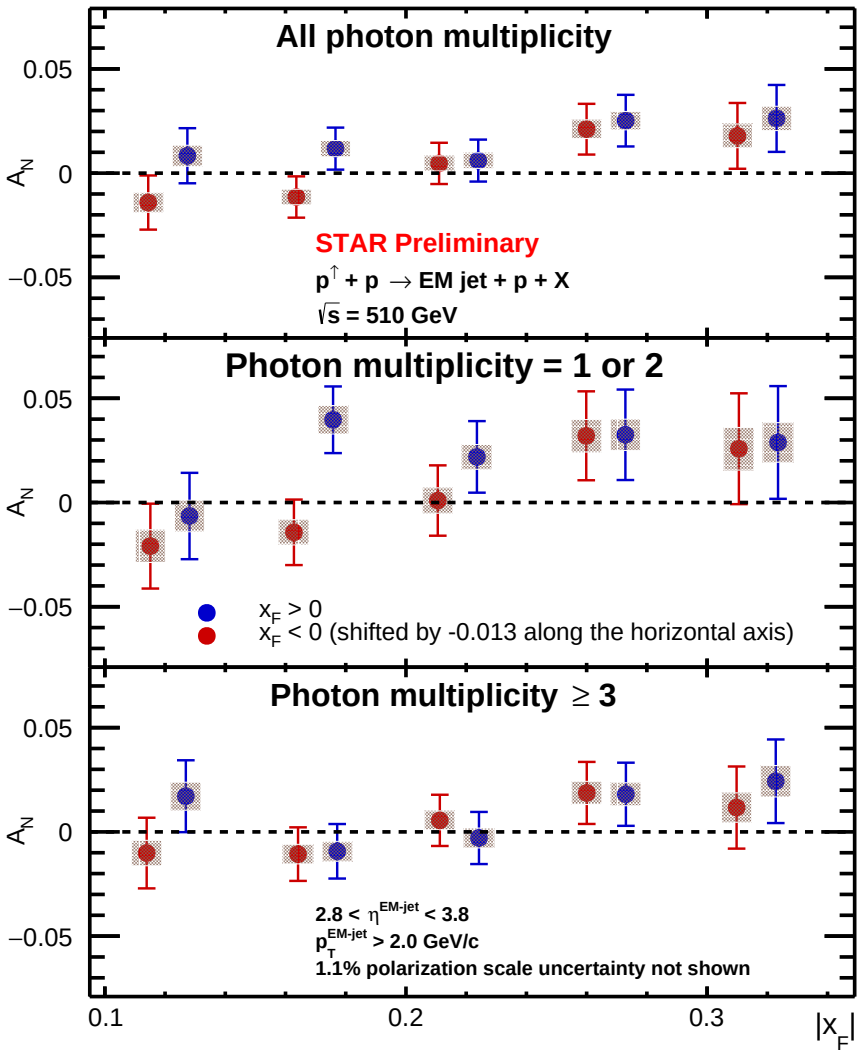

Figure 3.18: Transverse single-spin asymmetry for single diffractive events as a function of x_F with $p^{\uparrow} + p$ collisions at $\sqrt{s} = 510$ GeV for three different photon multiplicity cases: all photon multiplicity (top), one- or two-photon multiplicity (middle), and three- or more-photon multiplicity (bottom). The A_N for $x_F > 0$ are shown in blue points. The A_N for $x_F < 0$ (red points) shifts -0.013 along the x-axis.

The single diffractive EM-jet A_N for $\sqrt{s} = 200$ GeV and 510 GeV datasets show that they are more than 2-σ significance to be non-zero for the cases of all-photon multiplicity and one- or two-photon multiplicity for EM-jets with $x_F > 0$. Furthermore, the A_N for the EM-jets with one or two photons is much larger than the A_N with three or more photons for $x_F > 0$. These results show the single diffractive EM-jet A_N with the strong photon multiplicity dependency for $x_F > 0$, sharing a similar trend with the results shown in inclusive events [45].

Furthermore, a direct comparison for the single diffractive EM-jet A_N for $\sqrt{s} =$ 200 GeV and 510 GeV is shown in Fig. 3.19. Such a comparison plot provides direct insight into investigating the dependency of the single diffractive A_N on different center-of-mass energy collisions. The result shows that the single diffractive EM-jet A_N for $\sqrt{s} = 200$ and 510 GeV are consistent with each other within the uncertainty. This reveals that the energy dependency for the single diffractive EM-jet A_N is weak.

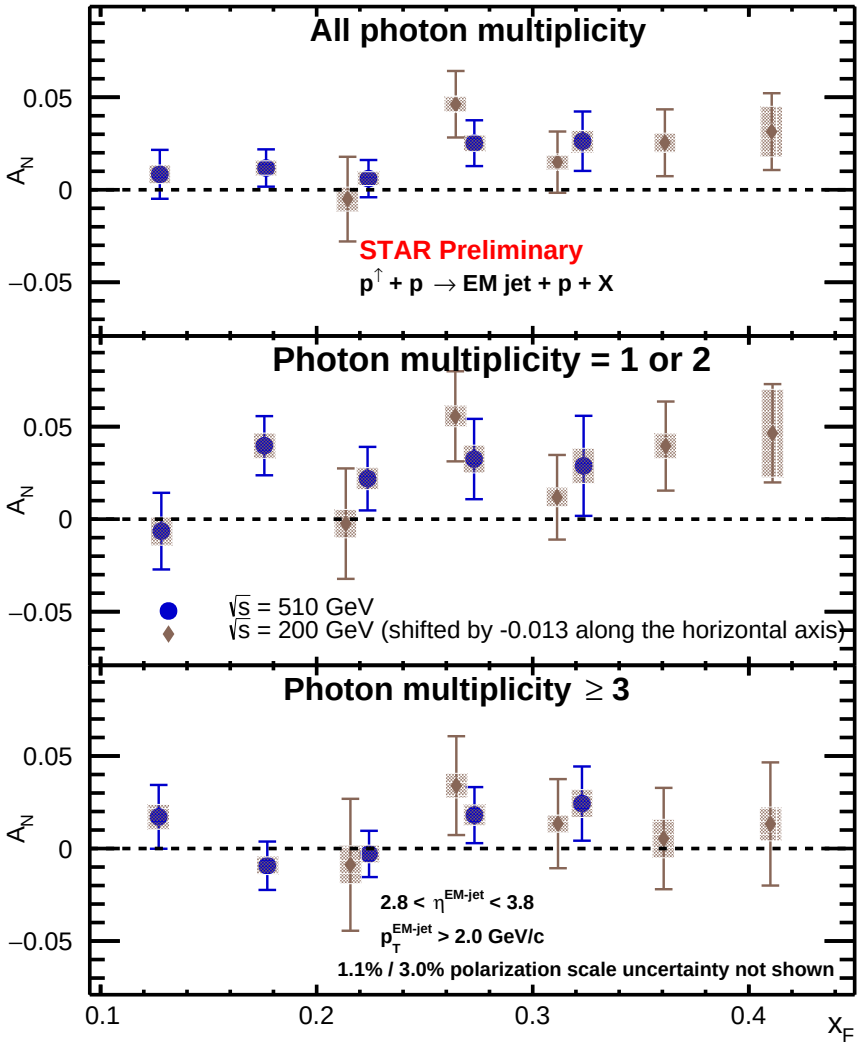

Figure 3.19: Comparison for the single diffractive EM-jet A_N for $\sqrt{s} = 200$ GeV (brown) and 510 GeV (blue). The single diffractive EM-jet A_N for $\sqrt{s} = 200$ GeV (brown points) shifts -0.013 along the x-axis.

Chapter 4

Transverse Single-spin Asymmetry for Rapidity Gap Events

4.1 Introduction

The rapidity gap event presented in this dissertation requires only one EM-jet at FMS, and the veto on the east side BBC. The EM-jet reconstruction and correction for the rapidity gap event are the same as those for the single diffractive event mentioned in Sec. 3.1.2. The East BBC veto for the rapidity gap event is also the same as that for the single diffractive event mentioned in Sec. 3.1.3. The major difference compared to the single diffractive event is that there is no requirement on the East RP in the rapidity gap event. Fig. 4.1 shows a schematic diagram for the rapidity gap event.

The single diffractive events mentioned in Chpt. 3 are the subset of the rapidity gap events. Since the RP detectors do not have full 2π azimuthal coverage, the A_N measurement

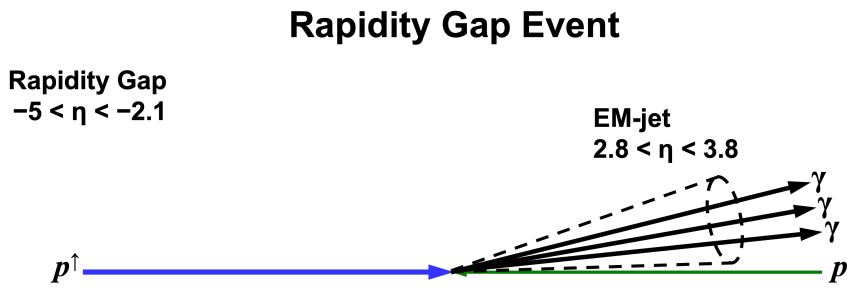

Figure 4.1: A schematic cartoon describing the rapidity gap event used for this analysis.

for the single diffractive events might be affected by such asymmetry. Considering that the fraction of the single diffractive events in the rapidity gap events (detailed in Sec. 4.2) is high, Furthermore, a particle-level simulation for the single diffractive events using Pythia 8 shows that when considering the BBC East veto in the particle level, which means that there are no charged hadrons at the final state, more than 86% of the events pass such BBC East veto. Besides, if it is required to present any jets in the FMS pseudorapidity region, more than 99% of the events pass such a BBC East veto. However, similar criteria for the non-single diffractive events at the particle level are explored, showing that only about 16% of the non-single diffractive events pass the BBC East veto at the particle level. Such results suggest that it may be optimistic to investigate single diffractive events using the East BBC veto without requiring East RP responses.

4.2 Single Diffractive Fraction in the Rapidity Gap Events

This section focuses on calculating the fraction of the single diffractive events in the rapidity gap events in the data measurement. To begin with, a particle-level simulation

for single diffractive events using Pythia 8 is performed. Then, both the east BBC detector simulation, via a GEANT3-based STAR detector level simulation, and the east RP detector simulation, via the pp2pp simulation mentioned in [68], are used for the detector-level simulation. The same BBC East veto cuts as those applied to the rapidity gap events are used in the simulation to determine the rapidity gap. The cut on the east RP track, hitting more than six east RP planes, is used to determine the good east RP track. In addition, only one RP track is allowed as the east RP cut for single diffractive events.

After applying the criteria above for the simulation, in this section, we define single diffractive (SD) events as the events that pass the BBC East veto cuts and the East RP cuts. Additionally, we define rapidity gap (RG) events in the simulation as those passing the east BBC cut without requiring the east RP cut. Notably, RG events in the simulation are all real single diffractive (RSD) events. However, RG events in data contain RSD events and non-single diffractive events (NSD). The fraction of SD events to RG events in the simulation and data can be expressed as Eq. 4.1 and Eq. 4.2, respectively. From both equations, the significant difference for RG events in simulation and data is that the non-single diffractive contamination only appears in the data. Furthermore, since the purity of SD events in the data is high (detailed in Sec. 3.2), we can consider the fraction of SD events to RSD events in the set of RG events, $\frac{SD}{RSD}$, is the same between the simulation and the data. The fraction of real single diffractive events among rapidity gap events in the data, $\frac{RSD}{RSD+NSD}$, is $68.7\% \pm 0.6\% \pm 8.2\%$ for the Run 15 dataset.

$$frac(sim) = \frac{SD}{RSD} \tag{4.1}$$

$$frac(data) = \frac{SD}{RSD + NSD} \tag{4.2}$$

The fraction of the real single diffractive events in the rapidity gap events is high. Therefore, the A_N for rapidity gap events is helpful to study A_N for single diffractive events. Furthermore, measuring the A_N for single diffractive events is not easy to perform for datasets with the STAR Forward Upgrade, because the RP detectors are unavailable for those datasets, which cannot provide detection of the forward scattering protons. The measurement of A_N for rapidity gap events offers a unique approach to accessing and exploring A_N for single diffractive events using the datasets collected with the STAR Forward Upgrades.

4.3 Results

4.3.1 Transverse Single-spin Asymmetry for Rapidity Gap Events in $\sqrt{s}$ = 200 GeV and 510 GeV

In this study, the A_N for rapidity gap events in $p^{\uparrow} + p$ collisions at $\sqrt{s} = 200$ GeV and 510 GeV, corresponding to the Run 15 dataset and the Run 17 dataset, is investigated. The cross-ratio method is applied to extract the A_N for the rapidity gap events. Details of the cross-ratio method can be found in Sec. 3.3. For the Run 15 dataset, the x_F range is [0.1, 0.4]. For the Run 17 dataset, the x_F range is [0.1, 0.35]. The full 2π azimuthal coverage is split into 16 ranges for each x_F region. The systematic uncertainty for the rapidity gap event EM-jet A_N are studied with the following terms using the same method as for the single diffractive EM-jet A_N study: BBC East veto cuts (detailed in Sec. 3.4.1) and Ring of

Fire (detailed in Sec. 3.4.2). Three photon multiplicity cases are considered for the rapidity gap event EM-jet A_N study: all-photon multiplicity, only one- or two-photon multiplicity, and three- or more-photon multiplicity. These three photon multiplicity cases are the same as that of the A_N for single diffractive events.

Figure 4.2 shows the A_N for the EM-jet of the rapidity gap events as a function of x_F for $\sqrt{s} = 200$ GeV with the three cases of photon multiplicity mentioned above. In addition, Fig. 4.3 shows the A_N for the EM-jet of rapidity gap events as a function of x_F for $\sqrt{s} = 510$ GeV with the same three cases of photon multiplicity. In both figures, the A_N of all photon-multiplicity and one- or two-photon multiplicity cases shows a non-zero value. However, the A_N for the three- or more-photon multiplicity case shows the value consistent with zero within uncertainty. Furthermore, the yellow beam A_N is also consistent with zero, regardless of the cases of the photon multiplicity.

A direct comparison of the A_N for the EM-jet of the rapidity gap events for $\sqrt{s} =$ 200 / 510 GeV datasets is shown in Fig. 4.4. In this figure, the A_N at lower x_F regions can be explored using the dataset with the higher $\sqrt{s}$ collisions. The A_N at higher x_F regions is accessible using the dataset with the lower $\sqrt{s}$ collisions. In the overlap x_F regions for the measurement with both datasets, the A_N for the rapidity gap events are consistent with each other within uncertainty. It shows that the rapidity gap event A_N has weak dependence on $\sqrt{s}$ energies of the collision.

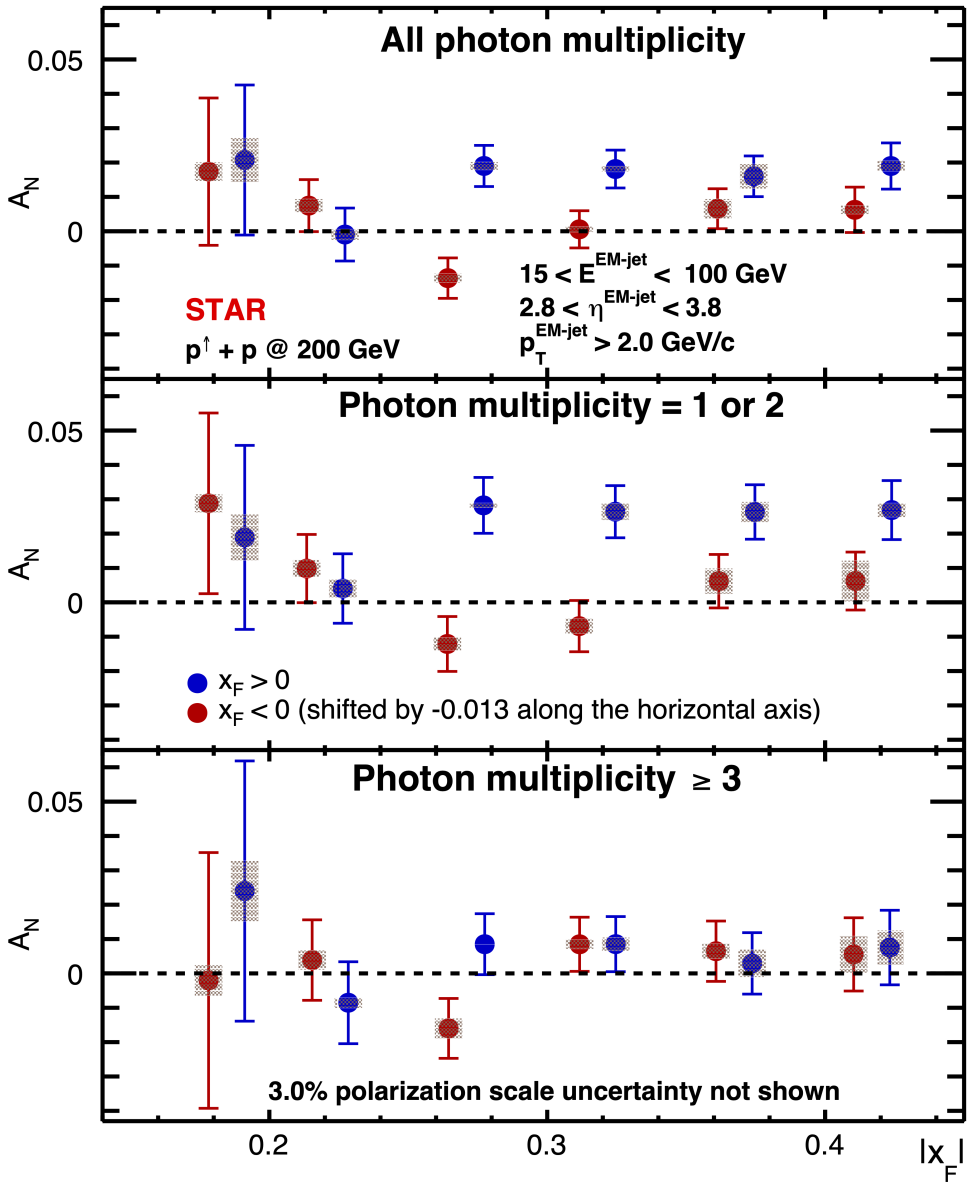

Figure 4.2: A_N for the EM-jet of rapidity gap events as a function of x_F using $p^{\uparrow}+p$ at $\sqrt{s}$ = 200 GeV dataset for three different photon multiplicity cases: all photon multiplicity (top), one- or two-photon multiplicity (middle), and three- or more-photon multiplicity (bottom). The A_N for $x_F < 0$ (red points) shifts -0.013 along the x-axis.

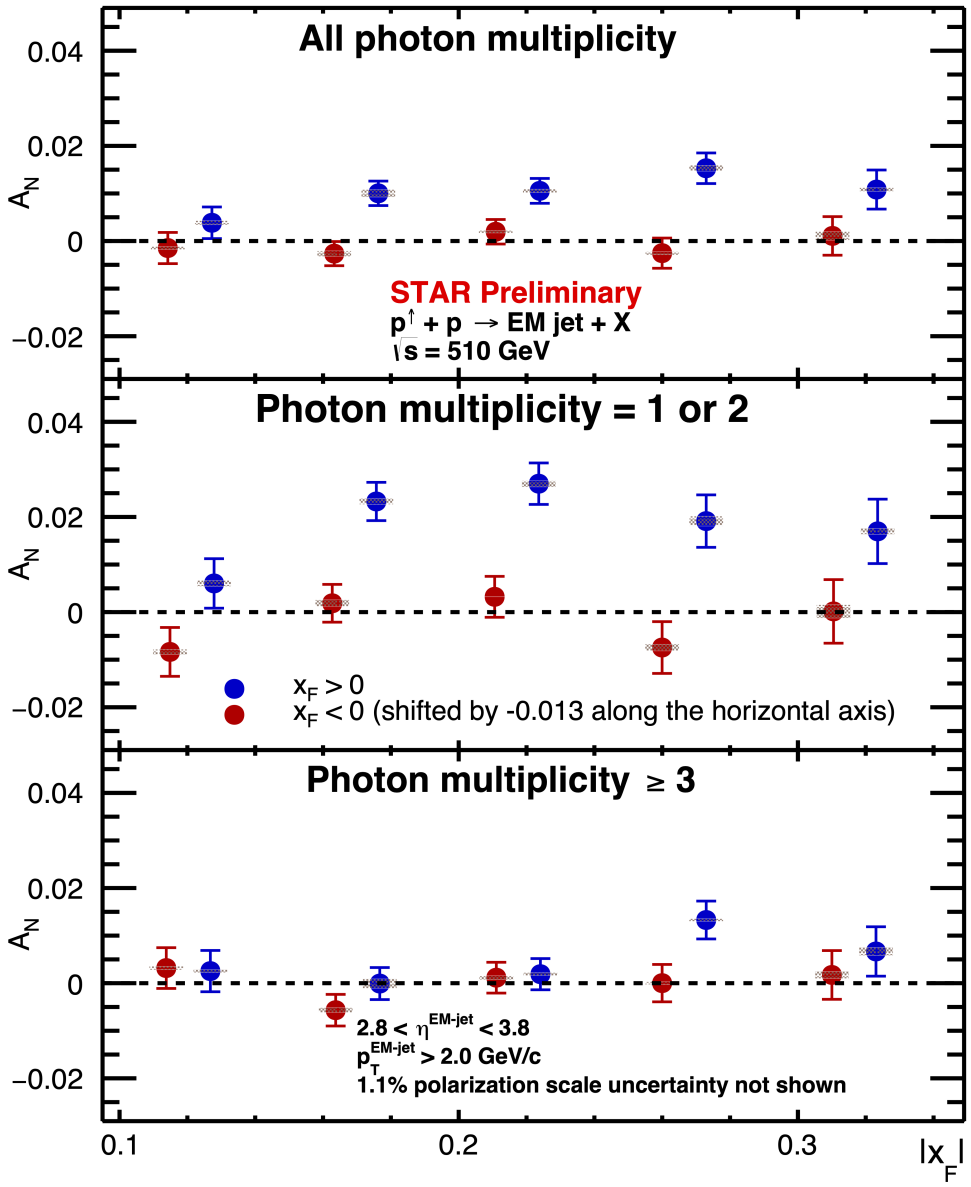

Figure 4.3: A_N for the EM-jet of rapidity gap events as a function of x_F $p^{\uparrow} + p$ at $\sqrt{s} =$ 510 GeV for three different photon multiplicity cases: all photon multiplicity (top), one- or two-photon multiplicity (middle), and three- or more-photon multiplicity (bottom). The A_N for $x_F < 0$ (red points) shifts -0.013 along the x-axis.

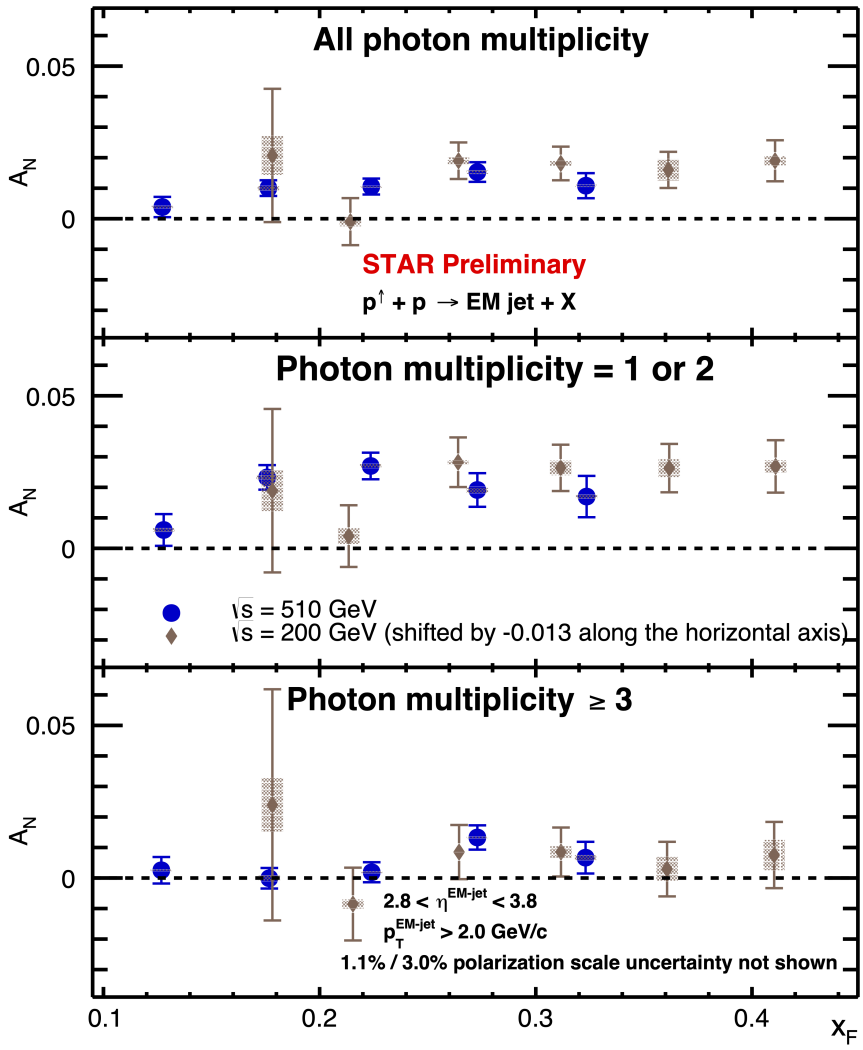

Figure 4.4: Comparison for the rapidity gap event EM-jet A_N for $\sqrt{s} = 200$ GeV (brown) and 510 GeV (blue). The rapidity gap event EM-jet A_N for $\sqrt{s} = 200$ GeV (brown points) shifts -0.013 along the x-axis.

4.3.2 Direct Comparison among Inclusive Events, Rapidity Gap Events, and Single Diffractive Events

One of the objectives of this dissertation is to examine the possible contribution of single diffractive events to the large transverse single-spin asymmetry observed in inclusive events. Figure 4.5 shows the direct comparison of the EM-jet A_N for inclusive events, rapidity gap events, and single diffractive events in $p^{\uparrow} + p$ collisions at $\sqrt{s} = 200$ GeV separated into two photon-multiplicity cases: one- or two-photon multiplicity, and three- or more-photon multiplicity. Similarly, Fig. 4.6 shows a similar comparison at $\sqrt{s} = 510$ GeV. In both datasets, the A_N for the inclusive events, rapidity gap events, and single diffractive events are consistent with each other within uncertainty. As discussed in Sec. 3.5, the fraction of single diffractive events contributing to the inclusive cross section in the forward region is small. However, the fraction of single diffractive events in the rapidity gap event sample is relatively large. If the large A_N observed in inclusive events were primarily driven by the single diffractive component, one would expect an even larger A_N in single diffractive events and rapidity gap events. However, no such enhancement is observed. Therefore, the A_N for single diffractive events is not a significant contribution to the large A_N observed in inclusive events.

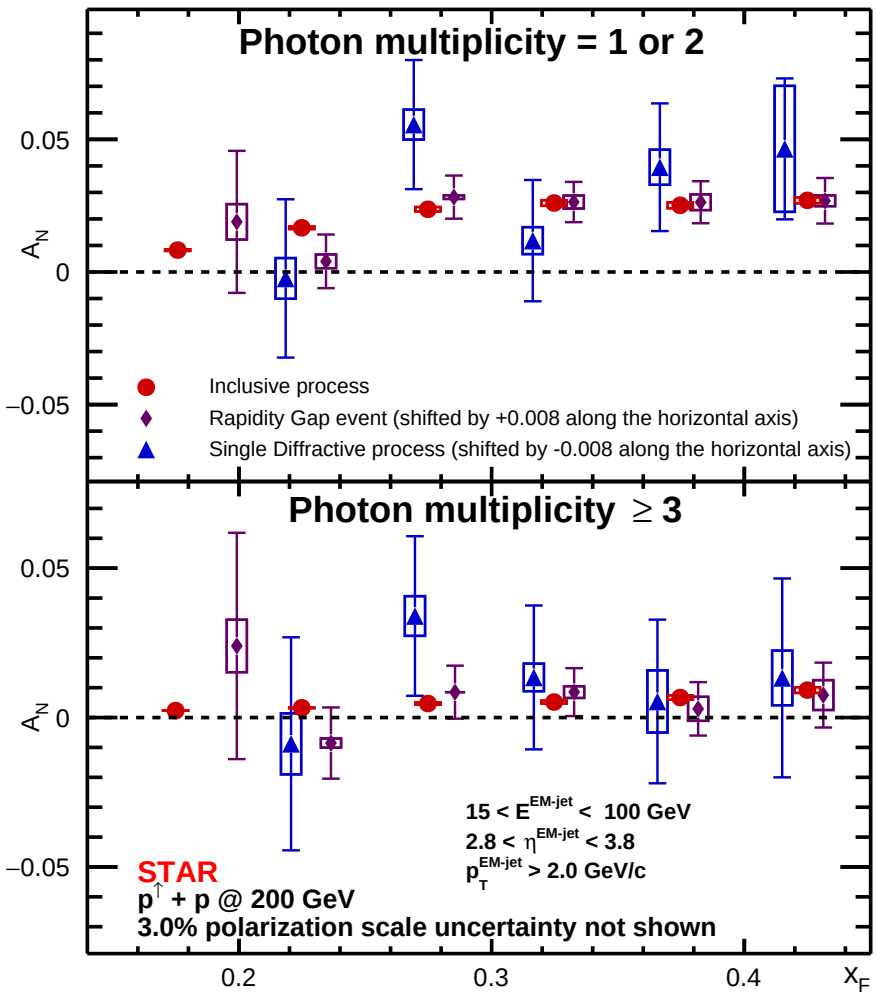

Figure 4.5: A_N for inclusive events (red), rapidity gap events (purple), and single diffractive events (blue) as a function of x_F in $p^{\uparrow} + p$ at $\sqrt{s} = 200$ GeV for one- or two-photon multiplicity case (top panel) and three- or more-photon multiplicity (bottom panel). The A_N for single diffractive process shifts -0.008 along the x-axis, and the A_N for rapidity gap events shifts +0.008 along the x-axis.

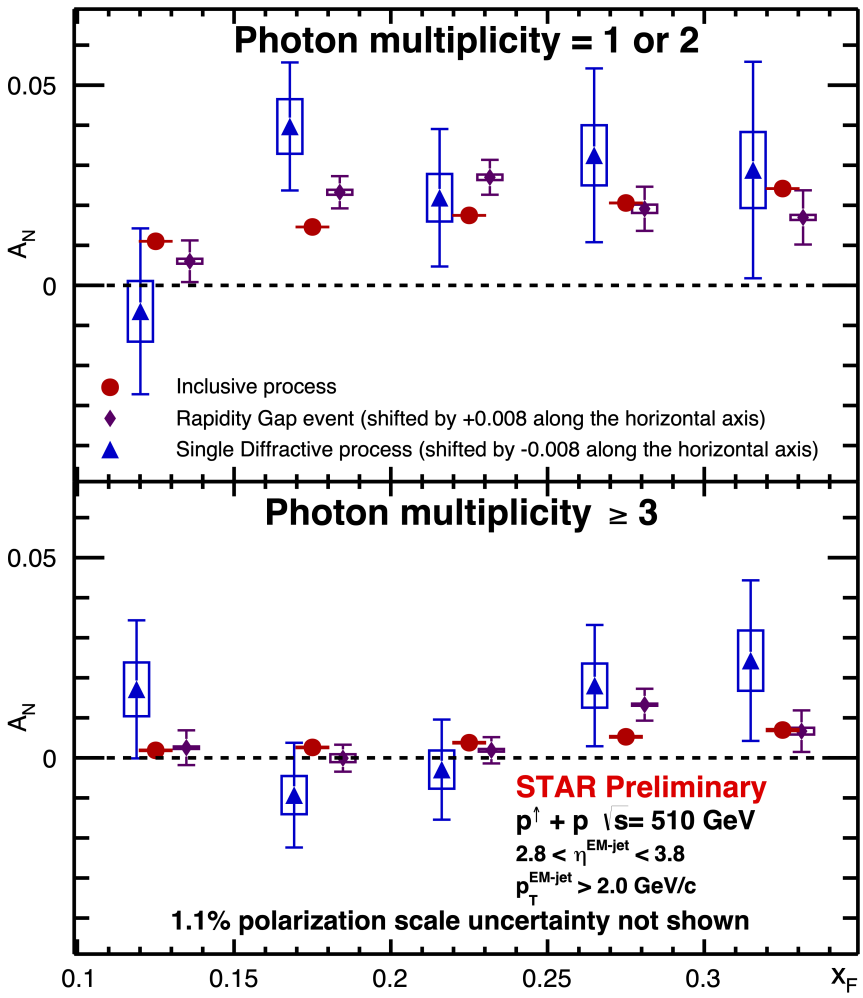

Figure 4.6: A_N for inclusive events (red), rapidity gap events (purple), and single diffractive events (blue) as a function of x_F in $p^{\uparrow} + p$ at $\sqrt{s} = 510$ GeV for one- or two-photon multiplicity case (top panel) and three- or more-photon multiplicity (bottom panel). The A_N for single diffractive process shifts -0.008 along the x-axis, and the A_N for rapidity gap events shifts +0.008 along the x-axis.

Chapter 5

Transverse Single-spin Asymmetry for Semi-exclusive Events

5.1 Event Selection

The semi-exclusive events are defined by requiring only one EM-jet at the FMS, one proton track on the west-side RP, and a veto on the west side BBC. In addition, the sum of the EM-jet energy and the proton energy is required to be consistent with the beam energy within resolution. Figure 5.1 shows a schematic cartoon describing the semi-exclusive event. However, the pseudorapidity coverage of the west side BBC partially overlaps with that of the FMS, which can not satisfy the rapidity gap requirement for the diffractive process. Consequently, semi-exclusive events can not be classified as diffractive events. Despite this, the semi-exclusive events remain of considerable interest, as they may provide insight into the underlying mechanism of the large A_N observed in the inclusive events.

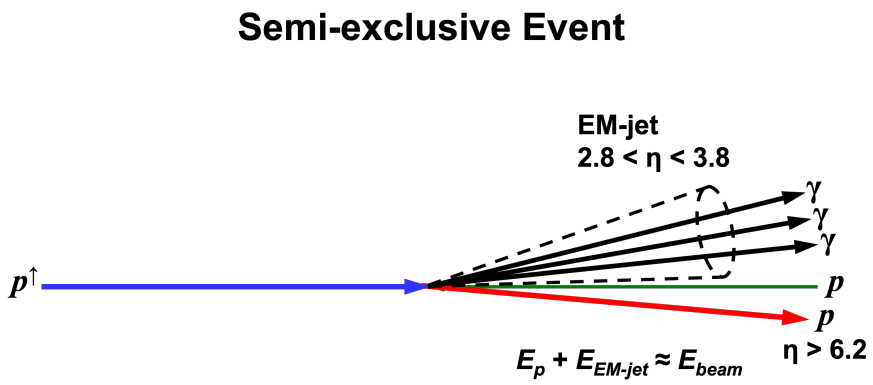

Figure 5.1: A schematic cartoon describing the semi-exclusive event used for this analysis.

The event selection criteria for the semi-exclusive events used in the Run 15 dataset and the Run 17 dataset can be briefly categorized as follows: event property, EM-jet reconstruction, BBC west veto, west RP track, and energy sum cuts. The details for these categories of event selection criteria are described in the following sub-sections.

5.1.1 Event Property and EM-jet Reconstruction

The event property cuts for semi-exclusive events are the same as those for single diffractive events in either dataset, with details in Sec. 3.1.1. To briefly summarize the event property cuts, they include the following terms:

- Events with only the bunches in the blue and yellow beams with protons are accepted. Events with abort gaps are discarded.
- The 4-bit spin pattern of the blue beam proton and the yellow beam proton must satisfy any of the four accepted cases shown in Tab. 3.1.

- The primary vertex position in the z direction (vertex z) is required to be within 80 cm of the STAR IR, vertex $|z| < 80$ cm.

Also, the EM-jet reconstruction algorithm and corrections for semi-exclusive events are the same as those for single diffractive events in each dataset, with detailed descriptions in Sec. 3.1.2. The EM-jet reconstruction algorithm and corrections include the following items:

- Only the reconstructed FMS points with energy greater than 1 GeV are used as photon candidates in the EM-jet reconstruction.
- The Anti-k_T algorithm with the resolution parameter $R = 0.7$.
- The reconstructed EM-jet transverse momentum (p_T) is required to be higher than both the fixed threshold (2 GeV/c) and the trigger-dependent threshold (detailed in Tab. 2.1).
- The Underlying Event correction using the off-axis method is applied to the reconstructed EM-jet energy.
- The energy correction for the EM-jet from detector level to particle level is applied.

5.1.2 BBC West Veto Cuts

The primary purpose of the BBC West veto cuts is to minimize the accidental coincidence events for the semi-exclusive events. However, the BBC West veto cuts can not be used to determine the rapidity gap.

The strategy for studying the BBC West veto cuts follows the same approach used in analyzing the BBC East veto cuts for single diffractive events. To begin with, the rough cut on the small BBC West ADC sum < 150 is applied to reduce the background. Next, rough selection criteria on the west RP track θ_X and θ_Y with nine different ξ ranges within $0 < \xi < 0.45$ are applied. Figure 5.2 shows the rough selection criteria of the west RP track θ_X for the Run 15 dataset, where the hot areas in every figure are determined as the rough west RP track θ_X and θ_Y cuts. The corresponding west RP track θ_X cuts for nine different ξ ranges are shown in Tab. 5.1. After applying the rough west RP track θ_X cuts, the west BBC small BBC ADC sum and the west BBC large BBC ADC sum are checked. The left panel of Fig. 5.3 shows the small BBC west ADC sum for the Run 15 dataset, while the right panel of Fig. 5.3 shows the large BBC west ADC sum for the Run 15 dataset. Based on these contributions, we select the small BBC West ADC sum < 80 and the large BBC West ADC sum < 60 as the BBC West veto cuts for the Run 15 dataset.

Furthermore, the BBC West veto cuts for the Run 17 dataset are investigated using a similar approach to that of the Run 15 dataset. For the Run 17 dataset, only the small BBC West ADC sum is accessible, while the large BBC West ADC sum is inaccessible. Therefore, the large BBC West earliest TDC value is studied and applied as the cut for the veto at the large BBC west region. The left and the right panel of Fig. 5.4 show the distributions of the small BBC West ADC sum and the large BBC West earliest TDC

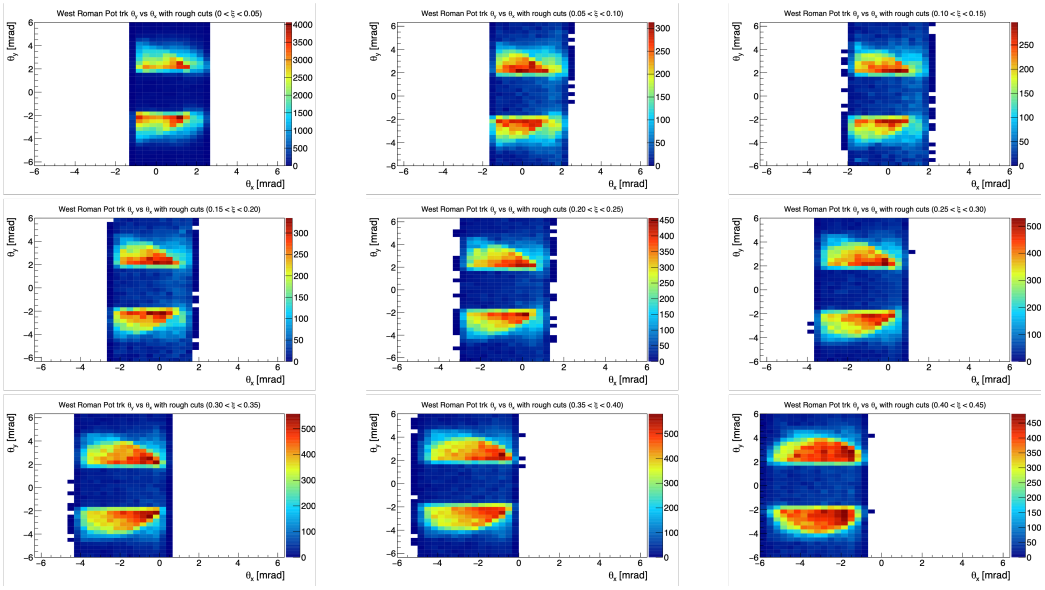

Figure 5.2: West RP θ_X and θ_Y distributions for nine different west RP track ξ ranges ($0 < \xi < 0.05$ (top left); $0.05 < \xi < 0.1$ (top middle); $0.1 < \xi < 0.15$ (top right); $0.15 < \xi < 0.2$ (middle left); $0.2 < \xi < 0.25$ (middle middle); $0.25 < \xi < 0.3$ (middle right); $0.3 < \xi < 0.35$ (bottom left); $0.35 < \xi < 0.4$ (bottom middle); $0.4 < \xi < 0.45$ (bottom right)) with only applying small BBC West ADC sum < 150 for the Run 15 dataset.

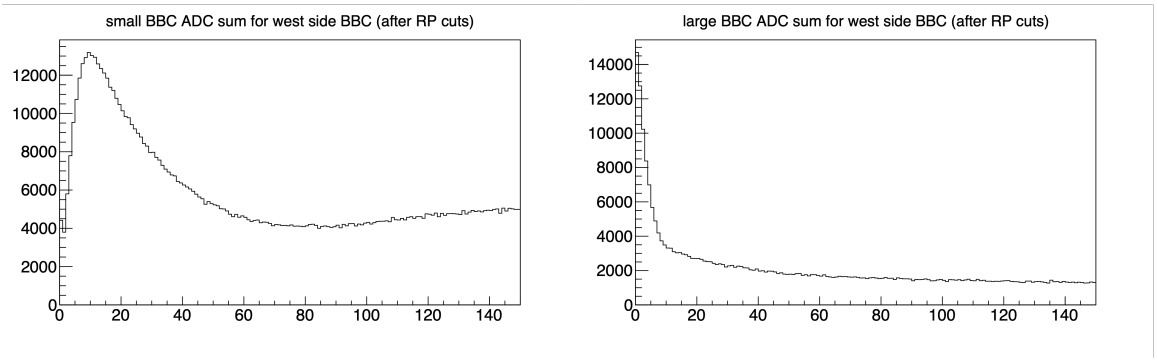

Figure 5.3: Small BBC west ADC sum distribution (left) and large BBC west ADC sum distribution (right) after the rough west RP cuts for the Run 15 dataset.

West RP ξ range	West RP θ_X rough cut [mrad]
$0 < \xi < 0.05$	$-1 < \theta_X < 1.75$
$0.05 < \xi < 0.1$	$-1.5 < \theta_X < 1.5$
$0.1 < \xi < 0.15$	$-1.75 < \theta_X < 1.25$
$0.15 < \xi < 0.2$	$-2.5 < \theta_X < 1.25$
$0.2 < \xi < 0.25$	$-3 < \theta_X < 1$
$0.25 < \xi < 0.3$	$-3.25 < \theta_X < 0.5$
$0.3 < \xi < 0.35$	$-3.75 < \theta_X < 0$
$0.35 < \xi < 0.4$	$-4.25 < \theta_X < -0.5$
$0.4 < \xi < 0.45$	$-5 < \theta_X < -1$

Table 5.1: Rough west RP θ_X cuts with ξ dependent for the Run 15 dataset.

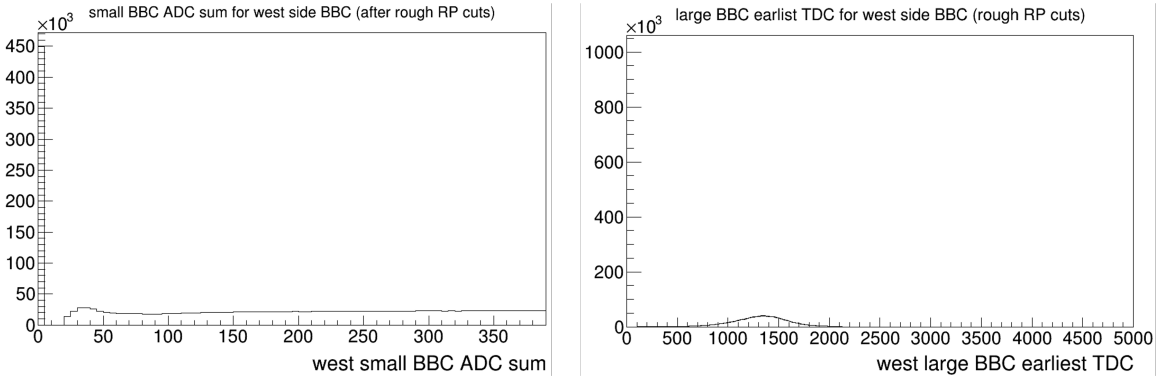

Figure 5.4: Small BBC west ADC sum distribution (left) and large BBC west earliest TDC distribution (right) after the rough west RP cuts for the Run 17 dataset.

distributions after passing the rough west RP θ_X and θ_Y cuts, respectively. The small BBC West ADC sum cut is chosen to be less than 80, and the large BBC West earliest TDC cut is determined to be less than 30 for the Run 17 dataset.

5.1.3 West Roman Pot (RP) Track Cuts

The studies of the west RP track cuts are conducted by applying the BBC west veto cuts. The west RP track cuts are applied to the kinematics of the west RP track, including the polar angle component in x- and y-directions (θ_X and θ_Y) of the west RP track, and the momentum component in x- and y-directions (p_X and p_Y) of the west RP track. Since the analysis procedures for Run 15 and Run 17 are identical, the detailed methodology is presented only for the Run 15 dataset, while for the Run 17 dataset, only the final results of the west RP track cuts are reported.

To begin with, the west RP θ_X and θ_Y distributions after the BBC west veto cuts are checked. Figure 5.5 shows the west RP θ_X and θ_Y distributions for nine different west RP ξ regions after the BBC west veto cuts. The hot regions are chosen as the west RP θ_X

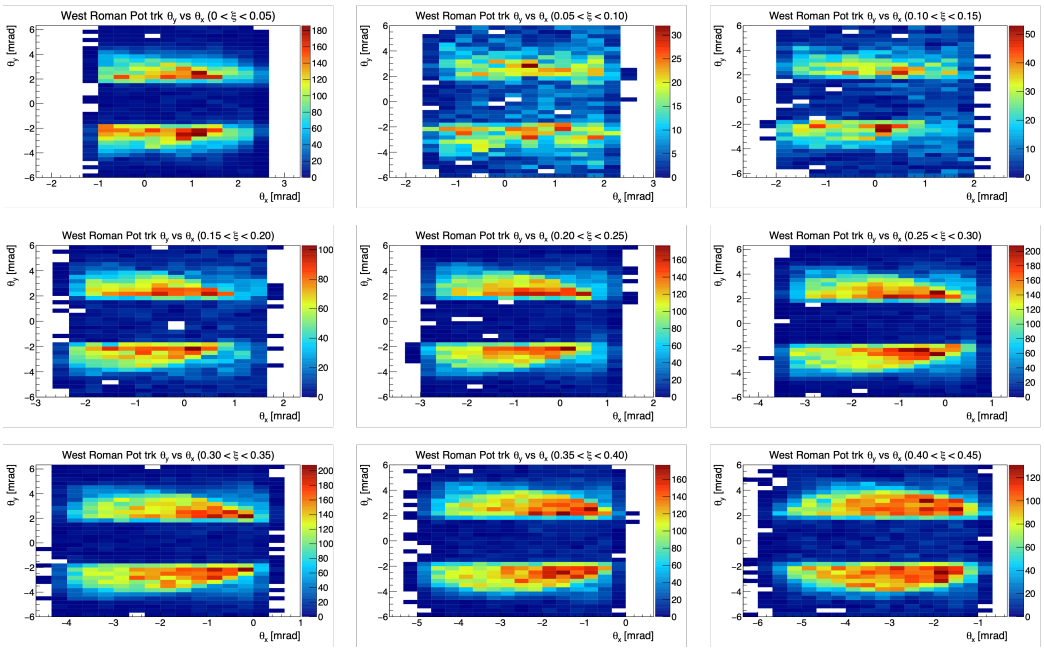

Figure 5.5: West RP θ_X and θ_Y distributions after the BBC west veto cuts for nine different west RP track ξ ranges ($0 < \xi < 0.05$ (top left); $0.05 < \xi < 0.1$ (top middle); $0.1 < \xi < 0.15$ (top right); $0.15 < \xi < 0.2$ (middle left); $0.2 < \xi < 0.25$ (middle middle); $0.25 < \xi < 0.3$ (middle right); $0.3 < \xi < 0.35$ (bottom left); $0.35 < \xi < 0.4$ (bottom middle); $0.4 < \xi < 0.45$ (bottom right)) for the Run 15 dataset.

and θ_Y cuts for each west RP ξ region. Table 5.2 shows the west RP θ_X cuts. The θ_Y cuts are $1.5 < |\theta_Y| < 4$ [mrad] for all nine west RP ξ regions.

Then, the west RP θ_X and θ_Y final cuts are applied to check distributions of the west RP p_X and p_Y. Figure 5.6 show the distributions of the west RP p_X and p_Y for nine west RP ξ regions for the Run 15 dataset, where black curves indicate the acceptance range of the west RP p_X and p_Y regions. Details of the west RP p_X and p_Y cuts for each west RP ξ region are shown in Tab. 5.3.

West RP ξ range	West RP θ_X final cut [mrad]
$0 < \xi < 0.05$	$-1 < \theta_X < 1.75$
$0.05 < \xi < 0.1$	$-1.5 < \theta_X < 1.5$
$0.1 < \xi < 0.15$	$-1.75 < \theta_X < 1.25$
$0.15 < \xi < 0.2$	$-2 < \theta_X < 1$
$0.2 < \xi < 0.25$	$-2.75 < \theta_X < 0.5$
$0.25 < \xi < 0.3$	$-3.25 < \theta_X < 0.5$
$0.3 < \xi < 0.35$	$-3.75 < \theta_X < 0$
$0.35 < \xi < 0.4$	$-4.5 < \theta_X < -0.5$
$0.4 < \xi < 0.45$	$-5.5 < \theta_X < -1.25$

Table 5.2: Final west RP θ_X cuts for the Run 15 dataset

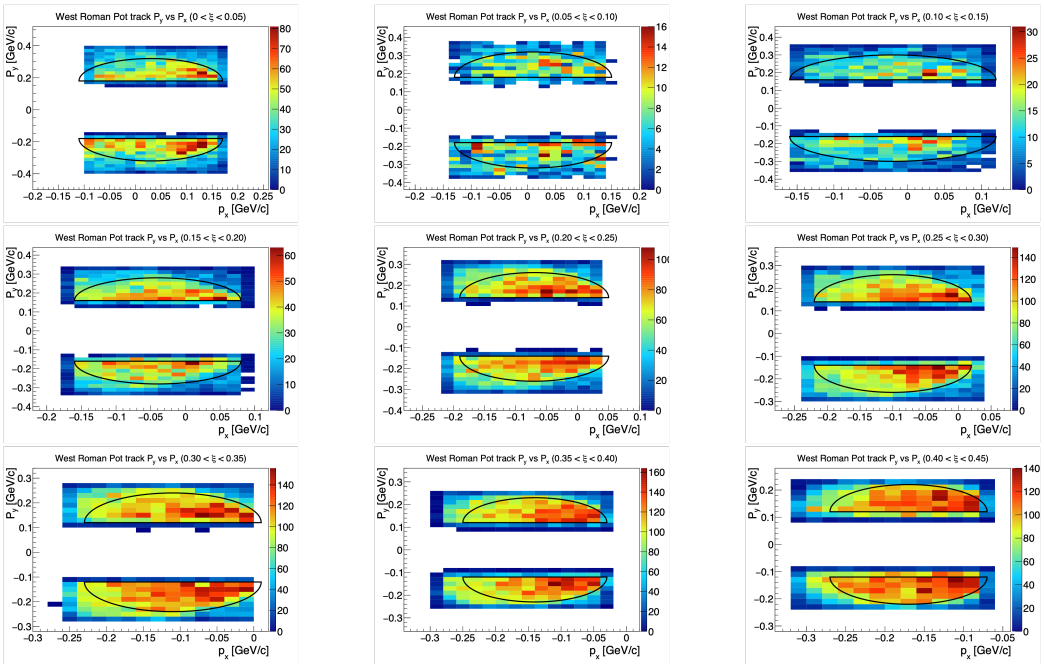

Figure 5.6: West RP track p_X and p_Y distributions for nine west RP track ξ ranges ($0 < \xi < 0.05$ (top left); $0.05 < \xi < 0.1$ (top middle); $0.1 < \xi < 0.15$ (top right); $0.15 < \xi < 0.2$ (middle left); $0.2 < \xi < 0.25$ (middle middle); $0.25 < \xi < 0.3$ (middle right); $0.3 < \xi < 0.35$ (bottom left); $0.35 < \xi < 0.4$ (bottom middle); $0.4 < \xi < 0.45$ (bottom right)) for the Run 15 dataset. The black curves indicate the ranges of accepted west RP track p_X and p_Y cuts.

West RP ξ range	West RP p_X and p_Y final cut [GeV/c]
$0 < \xi < 0.05$	$(p_X - 0.03)^2 + (p_Y - 0.18)^2 < 0.14^2$ and $0.18 < \lvert p_Y \rvert < 0.32$
$0.05 < \xi < 0.1$	$(p_X - 0.01)^2 + (p_Y - 0.18)^2 < 0.14^2$ and $0.18 < \lvert p_Y \rvert < 0.32$
$0.1 < \xi < 0.15$	$(p_X + 0.02)^2 + (p_Y - 0.16)^2 < 0.14^2$ and $0.16 < \lvert p_Y \rvert < 0.3$
$0.15 < \xi < 0.2$	$(p_X + 0.04)^2 + (p_Y - 0.16)^2 < 0.12^2$ and $0.16 < \lvert p_Y \rvert < 0.28$
$0.2 < \xi < 0.25$	$(p_X + 0.07)^2 + (p_Y - 0.14)^2 < 0.12^2$ and $0.14 < \lvert p_Y \rvert < 0.26$
$0.25 < \xi < 0.3$	$(p_X + 0.1)^2 + (p_Y - 0.14)^2 < 0.12^2$ and $0.14 < \lvert p_Y \rvert < 0.26$
$0.3 < \xi < 0.35$	$(p_X + 0.11)^2 + (p_Y - 0.12)^2 < 0.12^2$ and $0.12 < \lvert p_Y \rvert < 0.24$
$0.35 < \xi < 0.4$	$(p_X + 0.14)^2 + (p_Y - 0.12)^2 < 0.11^2$ and $0.12 < \lvert p_Y \rvert < 0.23$
$0.4 < \xi < 0.45$	$(p_X + 0.17)^2 + (p_Y - 0.12)^2 < 0.1^2$ and $0.12 < \lvert p_Y \rvert < 0.22$

Table 5.3: Final west RP p_X and p_Y cuts for each west RP ξ region of the Run 15 dataset.

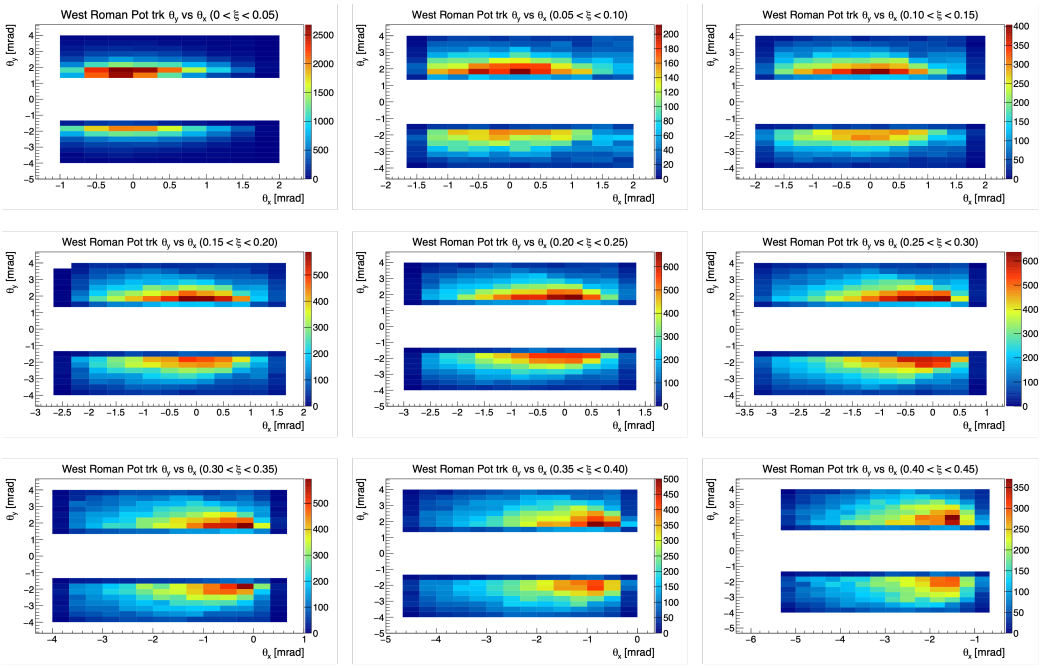

Figure 5.7: West RP θ_X and θ_Y distributions after the BBC west veto cuts for nine different west RP track ξ ranges ($0 < \xi < 0.05$ (top left); $0.05 < \xi < 0.1$ (top middle); $0.1 < \xi < 0.15$ (top right); $0.15 < \xi < 0.2$ (middle left); $0.2 < \xi < 0.25$ (middle middle); $0.25 < \xi < 0.3$ (middle right); $0.3 < \xi < 0.35$ (bottom left); $0.35 < \xi < 0.4$ (bottom middle); $0.4 < \xi < 0.45$ (bottom right)) for the Run 17 dataset.

For the Run 17 dataset, Fig. 5.7 shows the west RP θ_X and θ_Y distributions for each west RP ξ region, with the details of the west RP θ_X cuts for each west RP ξ region shown in Tab. 5.4. The θ_Y cuts are $1.5 < |\theta_Y| < 4$ [mrad] for all nine west RP ξ regions. In addition, the west RP p_X and p_Y distributions for each west RP ξ region are shown in Fig. 5.8. The west RP p_X and p_Y cuts for each west RP ξ region are shown in Tab. 5.5.

West RP ξ range	West RP θ_X final cut [mrad]
$0 < \xi < 0.05$	$-0.75 < \theta_X < 1.5$
$0.05 < \xi < 0.1$	$-1.25 < \theta_X < 1.5$
$0.1 < \xi < 0.15$	$-1.5 < \theta_X < 1.5$
$0.15 < \xi < 0.2$	$-1.75 < \theta_X < 1$
$0.2 < \xi < 0.25$	$-1.75 < \theta_X < 0.75$
$0.25 < \xi < 0.3$	$-2.25 < \theta_X < 0.5$
$0.3 < \xi < 0.35$	$-2.75 < \theta_X < 0.25$
$0.35 < \xi < 0.4$	$-3.5 < \theta_X < -0.25$
$0.4 < \xi < 0.45$	$-4.5 < \theta_X < -1$

Table 5.4: Final west RP θ_X cuts for the Run 17 dataset

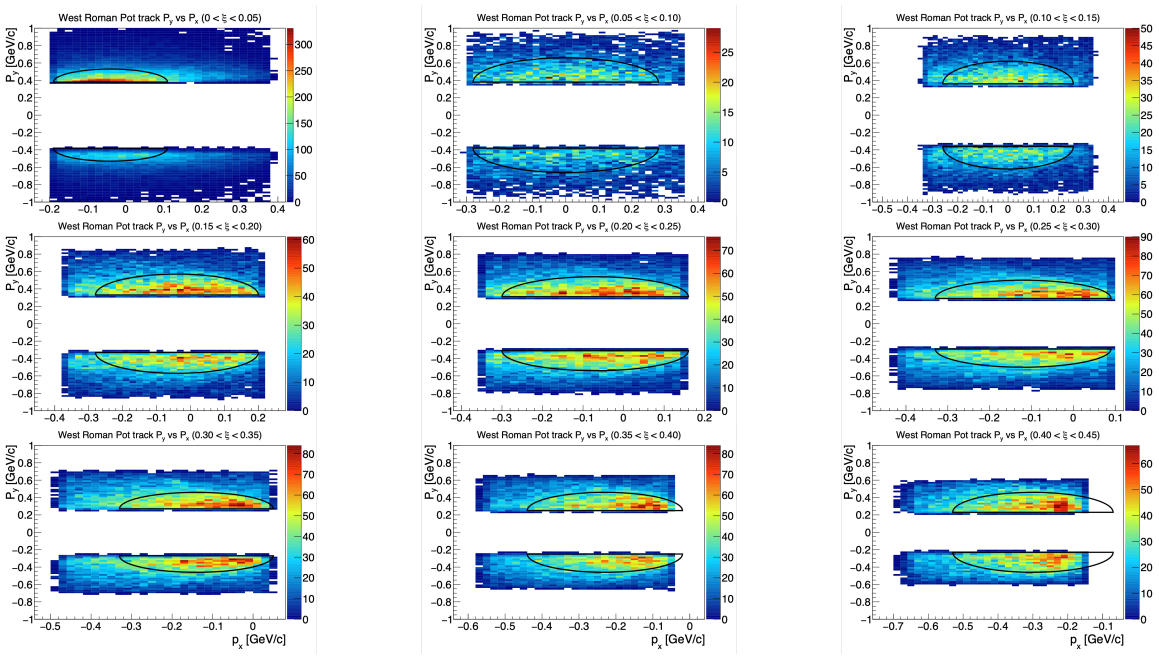

Figure 5.8: West RP track p_X and p_Y distributions for nine west RP track ξ ranges ($0 < \xi < 0.05$ (top left); $0.05 < \xi < 0.1$ (top middle); $0.1 < \xi < 0.15$ (top right); $0.15 < \xi < 0.2$ (middle left); $0.2 < \xi < 0.25$ (middle middle); $0.25 < \xi < 0.3$ (middle right); $0.3 < \xi < 0.35$ (bottom left); $0.35 < \xi < 0.4$ (bottom middle); $0.4 < \xi < 0.45$ (bottom right)) for the Run 17 dataset. The black curves indicate the ranges of accepted west RP track p_X and p_Y cuts.

West RP ξ range	West RP p_X and p_Y final cut [GeV/c]
$0 < \xi < 0.05$	$(p_X + 0.04)^2 + (p_Y - 0.38)^2 < 0.15^2$ and $0.15 < \lvert p_Y \rvert < 0.53$
$0.05 < \xi < 0.1$	$(p_X + 0.00)^2 + (p_Y - 0.38)^2 < 0.28^2$ and $0.28 < \lvert p_Y \rvert < 0.66$
$0.1 < \xi < 0.15$	$(p_X + 0.00)^2 + (p_Y - 0.36)^2 < 0.26^2$ and $0.26 < \lvert p_Y \rvert < 0.62$
$0.15 < \xi < 0.2$	$(p_X + 0.04)^2 + (p_Y - 0.33)^2 < 0.24^2$ and $0.24 < \lvert p_Y \rvert < 0.57$
$0.2 < \xi < 0.25$	$(p_X + 0.07)^2 + (p_Y - 0.31)^2 < 0.23^2$ and $0.23 < \lvert p_Y \rvert < 0.54$
$0.25 < \xi < 0.3$	$(p_X + 0.12)^2 + (p_Y - 0.29)^2 < 0.21^2$ and $0.32 < \lvert p_Y \rvert < 0.50$
$0.3 < \xi < 0.35$	$(p_X + 0.14)^2 + (p_Y - 0.21)^2 < 0.19^2$ and $0.19 < \lvert p_Y \rvert < 0.40$
$0.35 < \xi < 0.4$	$(p_X + 0.23)^2 + (p_Y - 0.25)^2 < 0.21^2$ and $0.21 < \lvert p_Y \rvert < 0.46$
$0.4 < \xi < 0.45$	$(p_X + 0.30)^2 + (p_Y - 0.23)^2 < 0.23^2$ and $0.23 < \lvert p_Y \rvert < 0.46$

Table 5.5: Final west RP p_X and p_Y cuts for each west RP ξ region of the Run 17 dataset.

5.1.4 Energy Sum Cut

For semi-exclusive events, the final state consists of an EM-jet and a proton, both detected on the west side. The sum of the EM-jet energy and the proton energy (hereafter referred to as the energy sum) is required to be consistent with the beam energy within resolution. Events satisfying this condition are categorized as semi-exclusive events.

The energy sum cut is studied after applying all other selection criteria, including event property cuts, EM-jet reconstruction and corrections, BBC west veto cuts, and west RP track cuts. At this stage, the EM-jet is well reconstructed and the West RP track is confirmed to be the good proton track. The energy sum cut is studied across different EM-jet x_F regions. Figure 5.9 shows the energy sum distributions for five EM-jet x_F regions for the Run 15 dataset, ranging from 0.2 to 0.45. In each figure, two distinct peaks are observed. The lower energy peak, at around the beam energy (100 GeV) within the resolution, corresponds to the real semi-exclusive events. However, the higher energy peak, exceeding the beam energy, arises primarily from accidental coincidence events, typically originating from multiple collisions in which the EM-jet is reconstructed from one event while the proton track is taken from another. In Sec. 5.2, there are more detailed discussions and studies on estimating the accidental coincidence event contributions. Based on the separation of the two peaks, the energy sum cuts are determined individually for each EM-jet x_F bin, keeping the peak at the lower energy, associated with real semi-exclusive events. Table 5.6 shows the energy sum cuts for each EM-jet x_F bin for the Run 15 dataset.

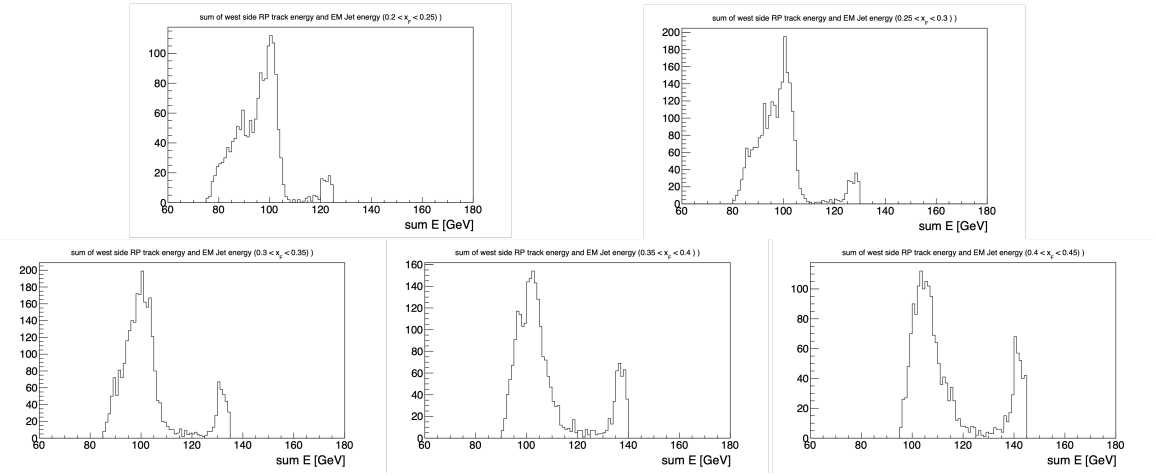

Figure 5.9: Energy sum distributions for five EM-jet x_F regions ($0.2 < x_F < 0.25$ (top left); $0.25 < x_F < 0.3$ (top right); $0.3 < x_F < 0.35$ (bottom left); $0.35 < x_F < 0.4$ (bottom middle); $0.4 < x_F < 0.45$ (bottom right)) for the Run 15 dataset.

EM-jet x_F	Energy sum (E_{sum}) cut
0.2 - 0.25	$E_{sum} < 110$ GeV
0.25 - 0.3	$E_{sum} < 110$ GeV
0.3 - 0.35	$E_{sum} < 115$ GeV
0.35 - 0.4	$E_{sum} < 115$ GeV
0.4 - 0.45	$E_{sum} < 120$ GeV

Table 5.6: Energy sum cuts for semi-exclusive process for five EM-jet x_F regions for the Run 15 dataset.

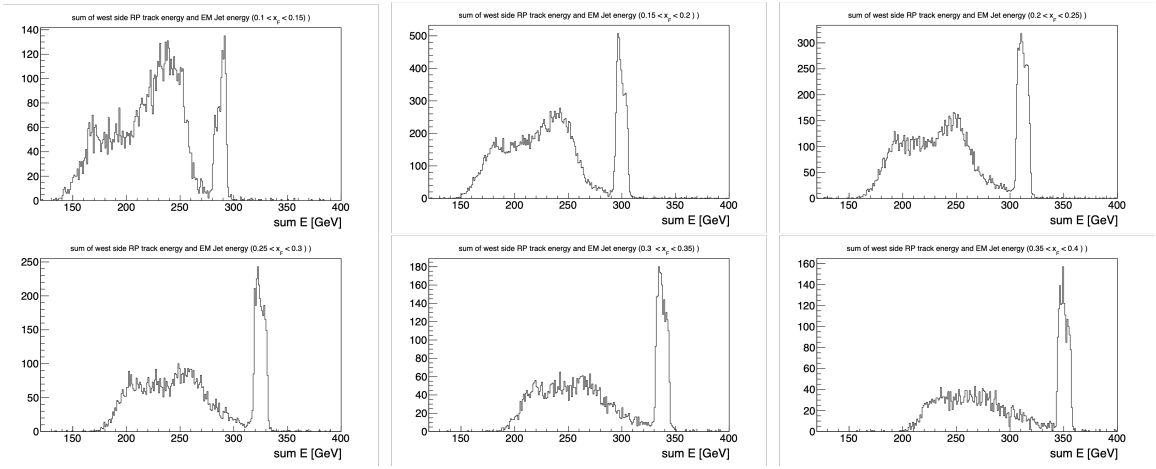

Figure 5.10: Energy sum distributions for six EM-jet x_F regions ($0.1 < x_F < 0.15$ (top left); $0.15 < x_F < 0.2$ (top middle); $0.2 < x_F < 0.25$ (top right); $0.25 < x_F < 0.3$ (bottom left); $0.3 < x_F < 0.35$ (bottom middle); $0.35 < x_F < 0.4$ (bottom right)) for the Run 17 dataset.

Figure 5.10 shows the energy sum distributions for different EM-jet x_F regions for the Run 17 dataset, ranging from 0.1 to 0.4. Following the same approach to studying the energy sum cuts, the energy sum cut values for the Run 17 dataset are summarized in Tab. 5.7.

5.2 Background Study

The primary goal of the background study is to estimate the fraction of accidental coincidence events in the semi-exclusive events using the mixed event method. Accidental coincidences typically arise when the West RP track originates from a proton in a non-diffractive process, most often elastic scattering. The EM-jet energy distribution from inclusive events (Details in [45]) and the west RP track energy distribution from the zerobias

EM-jet x_F	Energy sum (E_{sum}) cut
0.1 - 0.15	$E_{sum} < 260$ GeV
0.15 - 0.2	$E_{sum} < 270$ GeV
0.2 - 0.25	$E_{sum} < 280$ GeV
0.25 - 0.3	$E_{sum} < 290$ GeV
0.3 - 0.35	$E_{sum} < 310$ GeV
0.35 - 0.4	$E_{sum} < 320$ GeV

Table 5.7: Energy sum cuts for semi-exclusive process for six EM-jet x_F regions for the Run 17 dataset.

dataset (Details in Sec. 3.2) are used to estimate the accidental coincidence background shape.

In the mixed event method, all possible combinations of EM-jet energies from inclusive events and west RP energies from the zerobias dataset are calculated. Equation 5.1 shows the simplified expression for the mixed event method. Here, $P(i)$ refers to the fraction of EM-jet yields in the inclusive EM-jet energy distribution for [i,i+1] (GeV) bin for a given EM-jet x_F range. $n(j)$ is the yield of west RP momentum in the zerobias events within [j,j+1] (GeV/c) bin. Notably, the distribution of west RP momentum can be considered the same as the west RP energy distribution. By summing up all integer values of i and j, the energy sum distribution ($Esum(i+j)$) is obtained for each x_F bin. Figure 5.11 shows one example of the mixed event energy sum study for the Run 15 dataset. The left panel shows the inclusive EM-jet energy distribution in $0.2 < x_F < 0.25$ region, which corresponds to $20 <= i < 25$ in Eq. 5.1. The middle panel shows the west RP momentum

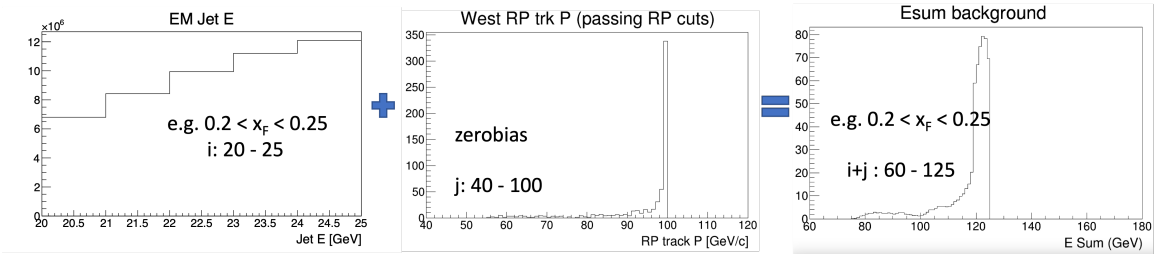

Figure 5.11: Example for mixed event energy sum background distribution for EM-jet with $0.2 < x_F < 0.25$ in the Run 15 dataset.

distribution in the zerobias dataset, restricted to west RP momentum between 40 GeV and 100 GeV for the Run 15 dataset, which corresponds to $40 <= j < 100$ in Eq. 5.1. The right panel shows the mixed event energy sum background distribution for EM-jet for $0.2 < x_F < 0.25$.

$$Esum(i+j) = \sum_{i,j} P(i) \times n(j) \tag{5.1}$$

Then, the shape of the mixed event energy sum background distribution is used to estimate the fraction of accidental events in semi-exclusive events. In each energy sum plot in the data, we define the signal region and the background region based on the energy sum cut in Tab. 5.6 for the Run 15 dataset and Tab. 5.7 for the Run 17 dataset. The shape of the mixed event energy sum background distribution is then scaled to the maximum bin value of the background region in the energy sum plot for the corresponding EM-jet x_F bin. Figure 5.12 and Figure 5.13 show the mixed event background distribution for each EM-jet x_F region for the Run 15 dataset and the Run 17 dataset, respectively. In each plot, the red curve indicates the energy sum distribution in the data, while the black curve indicates the scaled mixed event energy sum background distribution. The fraction of accidental

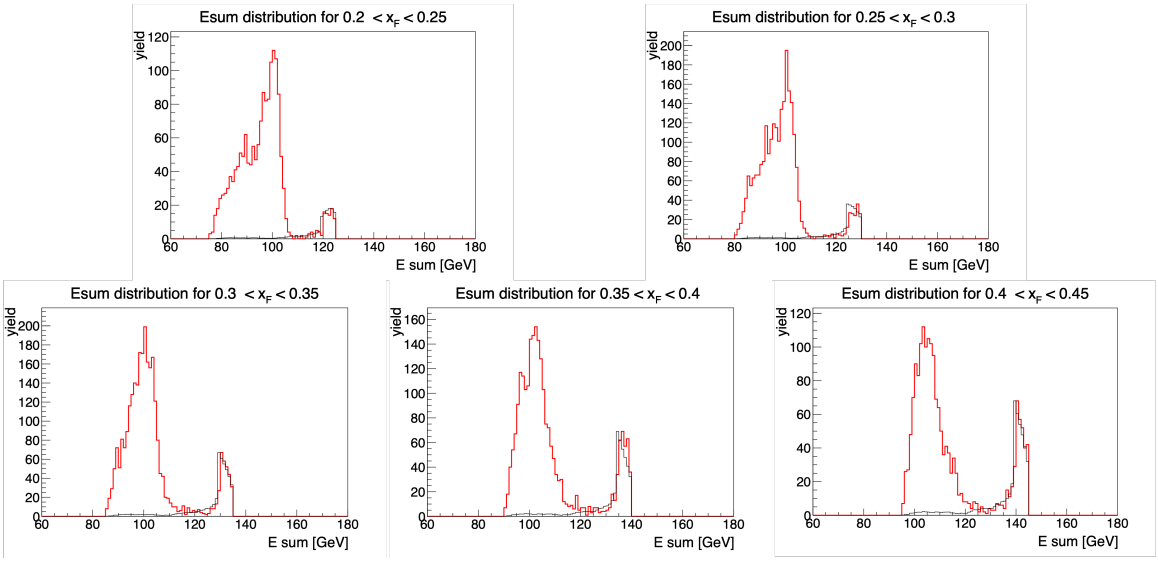

Figure 5.12: Mixed event energy sum background study results for each EM-jet x_F regions ($0.2 < x_F < 0.25$ (top left); $0.25 < x_F < 0.3$ (top right); $0.3 < x_F < 0.35$ (bottom left); $0.35 < x_F < 0.4$ (bottom middle); $0.4 < x_F < 0.45$ (bottom right)) for the Run 15 dataset.

coincidence events in semi-exclusive events in the data can be calculated as the ratio of the integrated yield for the scaled mixed event energy sum background to the integrated yield for the data in the signal region.

Table 5.8 shows the fraction of accidental coincidence events in semi-exclusive events in each EM-jet x_F bin for the Run 15 dataset. Such a fraction as the accidental coincidence background fraction is no higher than 2.7%, which means that the accidental coincidence will have a negligible effect on the results in the semi-exclusive event measurements. The effect on the results from the accidental coincidence background is assigned to the systematic uncertainty.

For the Run 17 dataset, Table 5.9 shows the fraction of the accidental coincidence events (background) for each EM-jet x_F region. Compared to the fraction of background in

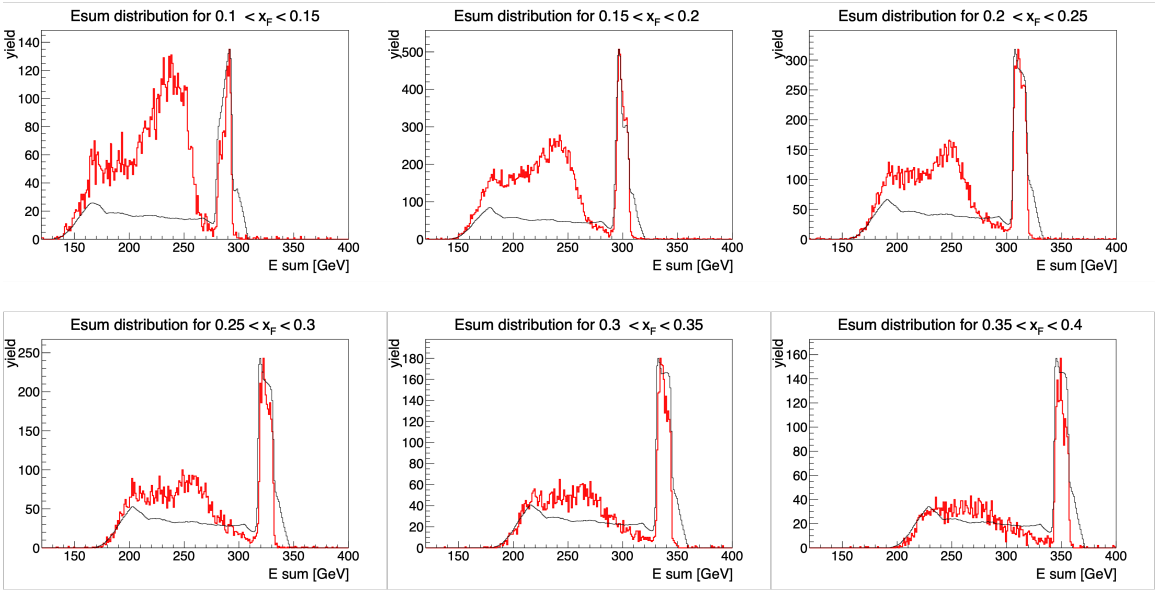

Figure 5.13: Mixed event energy sum background study results for six EM-jet x_F regions ($0.1 < x_F < 0.15$ (top left); $0.15 < x_F < 0.2$ (top middle); $0.2 < x_F < 0.25$ (top right); $0.25 < x_F < 0.3$ (bottom left); $0.3 < x_F < 0.35$ (bottom middle); $0.35 < x_F < 0.4$ (bottom right)) for the Run 17 dataset.

x_F	Fraction of background (%)
0.2 - 0.25	1.3
0.25 - 0.3	1.3
0.3 - 0.35	2.1
0.35 - 0.4	2.0
0.4 - 0.45	2.7

Table 5.8: Fraction of the accidental coincidence events (background) for each EM-jet x_F region for the Run 15 dataset.

x_F	Fraction of background (%)
0.1 - 0.15	26.3
0.15 - 0.2	33.5
0.2 - 0.25	44.8
0.25 - 0.3	49.9
0.3 - 0.35	64.0
0.35 - 0.4	88.1

Table 5.9: Fraction of the accidental coincidence events (background) for each EM-jet x_F region for the Run 17 dataset.

the Run 15 dataset, the fraction of background in the Run 17 dataset is significantly higher. It has a substantial impact on the results of the semi-exclusive measurements. One of the reasons for such behavior is related to the higher luminosity collisions during the Run 17 period. In this situation, minimizing the effect of the accidental coincidence events on the results for the semi-exclusive events in the Run 17 dataset is challenging and still ongoing. Therefore, in this dissertation, the study of the semi-exclusive EM-jet A_N measurement for the Run 17 dataset is halted until a better solution to reduce the background is found.

5.3 Systematic Uncertainty Study

The systematic uncertainty of A_N for semi-exclusive events includes BBC West veto cuts, energy sum cuts, the Ring of Fire, the accidental coincidence background, and the polarization uncertainty. The method of studying the systematic uncertainty for the

Ring of Fire is the same as mentioned in Sec. 3.4.2. The contributions of the accidental coincidence background are shown in Sec. 5.2, where the fraction of accidental coincidence events in semi-exclusive events is assigned as a systematic uncertainty. The final systematic uncertainty for the A_N of the semi-exclusive events is calculated individually for every x_F bin, and they are calculated as $\sqrt{\sum_i \sigma_i^2}$, where i is each term for systematic uncertainty. The polarization uncertainty is studied using the same approach as that for the single diffractive events, as mentioned in Sec. 3.4.3.

In this section, only the systematic uncertainty for the Run 15 dataset is mentioned.

5.3.1 Systematic Uncertainty for the BBC West Veto cuts

The systematic uncertainties for studying the small BBC west cuts and large BBC west cuts are explored using the Bayesian method as well as the Barlow check, as mentioned in Sec. 3.4.1. The cut values changed for studying the systematic uncertainty for the small BBC west ADC sum cut and the large BBC west ADC sum cut are listed as follows:

- Small BBC West ADC sum cut for the Run 15 dataset: choose four different cut values: < 60, < 70, < 90, < 100.
- Large BBC West ADC sum cut for the Run 15 dataset: choose four different cut values: < 40, < 50, < 70, < 80.

EM-jet x_F	E_{sum} cut (-10 GeV)	E_{sum} cut (-5 GeV)	E_{sum} cut (+5 GeV)	E_{sum} cut (+10 GeV)
0.2 - 0.25	$E_{sum} < 100$ GeV	$E_{sum} < 105$ GeV	$E_{sum} < 115$ GeV	$E_{sum} < 120$ GeV
0.25 - 0.3	$E_{sum} < 100$ GeV	$E_{sum} < 105$ GeV	$E_{sum} < 115$ GeV	$E_{sum} < 120$ GeV
0.3 – 0.35	$E_{sum} < 105$ GeV	$E_{sum} < 110$ GeV	$E_{sum} < 120$ GeV	$E_{sum} < 125$ GeV
0.35 – 0.4	$E_{sum} < 105$ GeV	$E_{sum} < 110$ GeV	$E_{sum} < 120$ GeV	$E_{sum} < 125$ GeV
0.4 – 0.45	$E_{sum} < 110$ GeV	$E_{sum} < 115$ GeV	$E_{sum} < 125$ GeV	$E_{sum} < 130$ GeV

Table 5.10: Energy sum cuts for semi-exclusive events in studying the systematic uncertainty for the Run 15 dataset.

5.3.2 Systematic Uncertainty for the Energy Sum cut

The systematic uncertainties for studying the energy sum cuts are explored using the Bayesian method as well as the Barlow check, as mentioned in Sec. 3.4.1. The energy sum cut per x_F bin is varied by the following terms: $+10$ GeV, $+5$ GeV, -5 GeV, and -10 GeV. Table 5.10 shows all energy sum cut values for studying the energy sum cut systematic uncertainty for each EM-jet x_F region for the Run 15 dataset.

5.4 Transverse Single-spin Asymmetry for Semi-exclusive Events in $\sqrt{s} = 200$ GeV

In this dissertation, the results of the transverse single-spin asymmetry for semi-exclusive events are limited to the Run 15 dataset. The cross-ratio method is used to extract the A_N. After applying all the event selection criteria, the available statistics are low, and the majority of semi-exclusive events correspond to EM-jets with one- or two-photon multiplicity. Consequently, only these events are used to extract the A_N.

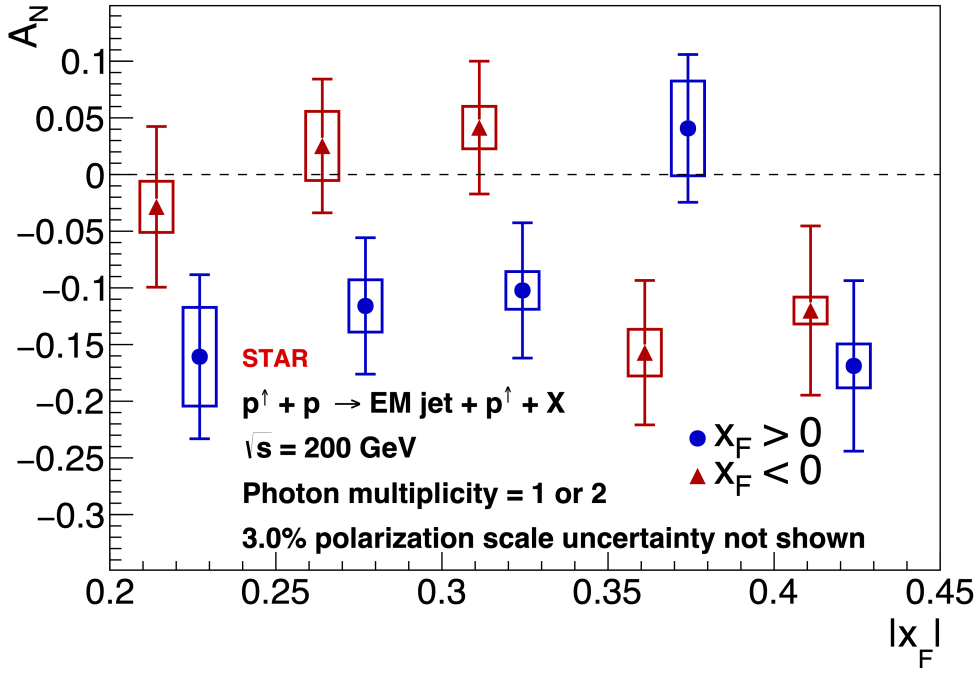

Figure 5.14: A_N for semi-exclusive events with one- or two-photon multiplicity EM-jets as a function of x_F in $p^{\uparrow}+p$ collisions at $\sqrt{s} = 200$ GeV. The blue points are for $x_F > 0$, while the red points are for $x_F < 0$, with shifting -0.005 along the x-axis.

Figure 5.14 shows the A_N for semi-exclusive events with one- or two-photon multiplicity EM-jet as a function of x_F in $p^{\uparrow}+p$ collisions at $\sqrt{s} = 200$ GeV. In the figure, five EM-jet x_F regions are considered, ranging from 0.20 to 0.45. The overall non-zero significant test is applied to semi-exclusive events with one- or two-photon multiplicity, using the constant fit for all points with either $x_F > 0$ or $x_F < 0$. The A_N for $x_F > 0$ is 3.1σ to be non-zero, while the A_N for $x_F < 0$ is 1.4σ to be non-zero. Interestingly, the semi-exclusive EM-jet A_N for $x_F > 0$ is negative on average, in contrast to the positive A_N observed in inclusive events and in single diffractive events. This difference in sign suggests a potentially distinct underlying mechanism, which requires further theoretical input.

Chapter 6

Conclusions and Outlook

The Transverse Single-spin Asymmetry (A_N) for proton-proton collisions is observed to be unexpectedly large in various experiments. Despite decades of theoretical effort, the underlying origin of this phenomenon remains unresolved. The A_N for the diffractive events is thought to be one of the potential sources, although no theoretical framework has yet established such a connection. This dissertation presents the first successful measurement of A_N in diffractive events in polarized proton-proton collisions, thereby providing crucial input toward developing a theoretical understanding of the role of diffraction in spin phenomena.

The STAR experiment at RHIC provides ideal opportunities to study the A_N for the diffractive events with the polarized proton-proton collisions at center-of-mass energies of 200 and 510 GeV. The Forward Meson Spectrometer (FMS), covering $2.6 < \eta < 4.2$, enables photon detection and EM-jet reconstruction. The Roman Pots (RP) detect slightly

scattered protons, while the Beam Beam Counter (BBC) ensures the rapidity gap condition for single diffractive events and helps suppress accidental coincidence backgrounds.

In this analysis, three types of diffractive or diffractive-like events are studied: single diffractive events, rapidity gap events, and semi-exclusive events. Multi-dimensional studies for the A_N are performed, with the dependency on EM-jet x_F, photon multiplicity, as well as the center-of-mass energy of the collisions. The A_N for single diffractive events and rapidity gap events shows a weak dependency on the EM-jet x_F and the center-of-mass energy of the collisions, but a strong dependency on the photon multiplicity. The EM-jets with one- or two-photon multiplicity show the strongest A_N. This behavior matches the studies of the A_N for inclusive events in the same dataset. The cross-section fraction study is conducted to determine the fraction of single diffractive events within inclusive events. Such a cross-section fraction is tiny ($0.672\% \pm 0.080\%$), providing evidence to understand single diffractive events in the forward region. The direct comparison across the A_N for inclusive events, single diffractive events, and rapidity gap events shows that the A_N for these three types of events are consistent with each other within uncertainty. These results conclude that the single diffractive events can not be a major source of the large A_N observed in inclusive events.

The A_N for semi-exclusive events in the polarized proton-proton collisions at $\sqrt{s} =$ 200 GeV shows a negative value, where its sign is opposite to the sign of the A_N for the inclusive events. Such a type of diffractive-like events disproves the contributions to the large A_N for the inclusive events. However, it remains unclear what the reason is for such a negative value of A_N for semi-exclusive events.

Looking ahead, further experimental studies are still required to understand the origin of the large A_N observed in inclusive events. The STAR experiment collected larger datasets using the STAR Forward Upgrade detectors, which allows further studies on the A_N in the forward region. The study of the A_N for rapidity gap events mentioned in this dissertation shed light on future measurements on A_N for rapidity gap events with the data collected using the STAR Forward Upgrade detectors, allowing us to have a better understanding on the contribution from the single diffractive events to the large A_N in the inclusive events.

Bibliography

[1] Francis Halzen and Alan D. Martin. *Quarks and Leptons: An Introductory Course in Modern Particle Physics*. John Wiley & Sons, New York, 1984.

[2] David J. Griffiths. *Introduction to Elementary Particles*. Wiley-VCH, Weinheim, 2nd rev. edition, 2008.

[3] M. Gell-Mann. A schematic model of baryons and mesons. *Physics Letters*, 8(3):214–215, 1964.

[4] G. Zweig. *An SU(3) model for strong interaction symmetry and its breaking. Version 2*, pages 22–101. 2 1964.

[5] J. D. Bjorken and E. A. Paschos. Inelastic electron-proton and γ-proton scattering and the structure of the nucleon. *Phys. Rev.*, 185:1975–1982, Sep 1969.

[6] David J. Gross and Frank Wilczek. Ultraviolet behavior of non-abelian gauge theories. *Phys. Rev. Lett.*, 30:1343–1346, Jun 1973.

[7] H. David Politzer. Reliable perturbative results for strong interactions? *Phys. Rev. Lett.*, 30:1346–1349, Jun 1973.

[8] Richard P. Feynman. Very high-energy collisions of hadrons. *Physical Review Letters*, 23(24):1415–1417, 1969.

[9] Davison E. Soper. Parton distribution functions. *Nuclear Physics B - Proceedings Supplements*, 53(1–3):69–80, February 1997.

[10] European Muon Collaboration. The spin asymmetry of the proton. *Physics Letters B*, 206(2):364–370, 1988.

[11] R.L. Jaffe and Aneesh Manohar. The g1 problem: Deep inelastic electron scattering and the spin of the proton. *Nuclear Physics B*, 337(3):509–546, 1990.

[12] M. S. Abdallah and all. Longitudinal double-spin asymmetry for inclusive jet and dijet production in polarized proton collisions at $\sqrt{s} = 200$ GeV. *Phys. Rev. D*, 103:L091103, May 2021.

[13] M. S. Abdallah and all. Longitudinal double-spin asymmetry for inclusive jet and dijet production in polarized proton collisions at $\sqrt{s} = 510$ GeV. *Phys. Rev. D*, 105:092011, May 2022.

[14] Elke-Caroline Aschenauer et al. The RHIC Cold QCD Program, 2 2023.

[15] C. Lorcé and B. Pasquini. Quark wigner distributions and orbital angular momentum. *Phys. Rev. D*, 84:014015, Jul 2011.

[16] G. L. Kane, J. Pumplin, and W. Repko. Transverse quark polarization in large-p_T reactions, e^+e^- jets, and leptoproduction: A test of quantum chromodynamics. *Phys. Rev. Lett.*, 41:1689–1692, Dec 1978.

[17] R. D. Klem, J. E. Bowers, H. W. Courant, H. Kagan, M. L. Marshak, E. A. Peterson, K. Ruddick, W. H. Dragoset, and J. B. Roberts. Measurement of Asymmetries of Inclusive Pion Production in Proton Proton Interactions at 6-GeV/c and 11.8-GeV/c. *Phys. Rev. Lett.*, 36:929–931, 1976.

[18] J. D. Skeens. Analyzing power in inclusive π^+, π^-, and Λ production at high x_F with 200-GeV polarized protons. *AIP Conf. Proc.*, 243:1008–1011, 1992.

[19] J. Adam and all. Measurement of transverse single-spin asymmetries of π^0 and electromagnetic jets at forward rapidity in 200 and 500 gev transversely polarized proton-proton collisions. *Phys. Rev. D*, 103:092009, May 2021.

[20] J. Adam and all. Comparison of transverse single-spin asymmetries for forward π^0 production in polarized pp, pAl and pAu collisions at nucleon pair c.m. energy $\sqrt{s_{\rm NN}} = 200$ GeV. *Phys. Rev. D*, 103:072005, Apr 2021.

[21] M. H. Kim and all. Transverse single-spin asymmetry for very forward neutral pion production in polarized p+p collisions at $\sqrt{s} = 510$ GeV. *Phys. Rev. Lett.*, 124:252501, Jun 2020.

[22] N. J. Abdulameer and all. Transverse single-spin asymmetry of charged hadrons at forward and backward rapidity in polarized $p + p$, $p +$ Al, and $p +$ Au collisions at $\sqrt{s_{NN}} = 200$ GeV. *Phys. Rev. D*, 108:072016, Oct 2023.

[23] Elke-Caroline Aschenauer et al. The RHIC Cold QCD Plan for 2017 to 2023: A Portal to the EIC. 2 2016.

[24] The STAR Colaboration. The star forward calorimeter system and forward tracking system. 2017.

[25] Stanley J. Brodsky, Dae Sung Hwang, and Ivan Schmidt. Initial-state interactions and single-spin asymmetries in drell–yan processes. *Nuclear Physics B*, 642(1–2):344–356, October 2002.

[26] Daniël Boer, Stanley J. Brodsky, and Dae Sung Hwang. Initial-state interactions in the unpolarized drell-yan process. *Physical Review D*, 67(5), March 2003.

[27] R. Angeles-Martinez et al. Transverse Momentum Dependent (TMD) parton distribution functions: status and prospects. *Acta Phys. Polon. B*, 46(12):2501–2534, 2015.

[28] A. Accardi and all. Electron ion collider: The next qcd frontier - understanding the glue that binds us all, 2014.

[29] Matthias Grosse Perdekamp and Feng Yuan. Transverse spin structure of the nucleon. *Annual Review of Nuclear and Particle Science*, 65(1):429–456, October 2015.

[30] Dennis Sivers. Single-spin production asymmetries from the hard scattering of pointlike constituents. *Phys. Rev. D*, 41:83–90, Jan 1990.

[31] Stanley J. Brodsky, Dae Sung Hwang, and Ivan Schmidt. Final-state interactions and single-spin asymmetries in semi-inclusive deep inelastic scattering. *Physics Letters B*, 530(1–4):99–107, March 2002.

[32] S. J. Brodsky, D. S. Hwang, and I. Schmidt. Final-state interactions and single-spin asymmetries in semi-inclusive deep inelastic scattering. *Phys. Lett. B*, 530:99–107, 2002.

[33] R. Aghasyan and others (COMPASS Collaboration). First measurement of the drell-yan transverse spin asymmetries in proton-proton collisions at the compass experiment. *Phys. Rev. Lett.*, 119:112002, 2017.

[34] John Collins. Fragmentation of transversely polarized quarks probed in transverse momentum distributions. *Nuclear Physics B*, 396(1):161–182, 1993.

[35] A. Airapetian and all. Effects of transversity in deep-inelastic scattering by polarized protons. *Physics Letters B*, 693(1):11–16, September 2010.

[36] M. S. Abdallah and all. Azimuthal transverse single-spin asymmetries of inclusive jets and identified hadrons within jets from polarized pp collisions at $\sqrt{s} = 200$ GeV. *Phys. Rev. D*, 106:072010, Oct 2022.

[37] Jian-Wei Qiu. Transverse single-spin asymmetries. In *Proceedings of DIS2012*. DESY, 2012.

[38] Jianwei Qiu and George Sterman. Single transverse spin asymmetries. *Phys. Rev. Lett.*, 67:2264–2267, Oct 1991.

[39] A.V. Efremov and O.V. Teryaev. Qcd asymmetry and polarized hadron structure function measurement. *Physics Letters B*, 150(5):383–386, 1985.

[40] Xiangdong Ji, Jian-Wei Qiu, Werner Vogelsang, and Feng Yuan. Unified picture for single transverse-spin asymmetries in hard-scattering processes. *Phys. Rev. Lett.*, 97:082002, Aug 2006.

[41] R. L. Workman et al. Review of Particle Physics. *PTEP*, 2022:083C01, 2022.

[42] VN Gribov. A reggeon diagram technique. *Sov. Phys. JETP*, 26(2):414–423, 1968.

[43] The H1 and ZEUS Collaborations. Combined inclusive diffractive cross sections measured with forward proton spectrometers in deep inelastic ep scattering at hera. *The European Physical Journal C*, 72(10):2175, 2012.

[44] V. Khachatryan and all. Measurement of diffractive dissociation cross sections in pp collisions at $\sqrt{s} = 7$ TeV. *Phys. Rev. D*, 92:012003, Jul 2015.

[45] Latiful Kabir. Transverse Single-Spin Asymmetries for π^0 and Electromagnetic Jets at Forward Rapidities in p↑+p Collisions at $\sqrt{s} = 200$ GeV and 500 GeV at STAR. *JPS Conf. Proc.*, 37:020119, 2022.

[46] I Alekseev et al. Polarized Proton Collider at RHIC. *Nucl. Instrum. Meth. A*, 499:392–414, 2003.

[47] M. Harrison, T. Ludlam, and S. Ozaki. RHIC project overview. *Nucl. Instrum. Meth. A*, 499:235–244, 2003.

[48] Thomas Ludlam and Larry McLerran. What have we learned from the relativistic heavy ion collider? *Physics Today*, 56(10):48–54, 10 2003.

[49] H. Hahn et al. The RHIC design overview. *Nucl. Instrum. Meth. A*, 499:245–263, 2003.

[50] A. Zelenski, G. Atoian, D. Raparia, J. Ritter, and D. Steski. The rhic polarized h ion source. *Review of Scientific Instruments*, 87(2):02B705, 10 2015.

[51] L.H. Thomas. I. the kinematics of an electron with an axis. *The London, Edinburgh, and Dublin Philosophical Magazine and Journal of Science*, 3(13):1–22, 1927.

[52] V. Bargmann, Louis Michel, and V. L. Telegdi. Precession of the polarization of particles moving in a homogeneous electromagnetic field. *Phys. Rev. Lett.*, 2:435–436, May 1959.

[53] Ya. S. Derbenev, A. M. Kondratenko, S. I. Serednyakov, A. N. Skrinsky, G. M. Tumaikin, and Yu. M. Shatunov. RADIATIVE POLARIZATION: OBTAINING, CONTROL, USING. *Part. Accel.*, 8:115–126, 1978.

[54] H. Okada et al. Absolute polarimetry at RHIC. *AIP Conf. Proc.*, 980(1):370–379, 2008.

[55] I. Nakagawa et al. Polarization measurements of RHIC-pp RUN05 using CNI pC-polarimeter. *AIP Conf. Proc.*, 915(1):912–915, 2007.

[56] H. Okada et al. Measurement of the analyzing power A(N) in pp elastic scattering in the CNI region with a polarized atomic hydrogen gas jet target. 1 2006.

[57] M. Anderson et al. The Star time projection chamber: A Unique tool for studying high multiplicity events at RHIC. *Nucl. Instrum. Meth. A*, 499:659–678, 2003.

[58] M. Beddo et al. The STAR barrel electromagnetic calorimeter. *Nucl. Instrum. Meth. A*, 499:725–739, 2003.

[59] C. E. Allgower et al. The STAR endcap electromagnetic calorimeter. *Nucl. Instrum. Meth. A*, 499:740–750, 2003.

[60] J. Adam and all. Longitudinal double-spin asymmetries for π^0s in the forward direction for 510 gev polarized *pp* collisions. *Phys. Rev. D*, 98:032013, Aug 2018.

[61] J. KIRYLUK. Local polarimetry for proton beams with the star beam beam counters. In *Spin 2004*, page 718–721. WORLD SCIENTIFIC, August 2005.

[62] W.J. Llope and all. The star vertex position detector. *Nuclear Instruments and Methods in Physics Research Section A: Accelerators, Spectrometers, Detectors and Associated Equipment*, 759:23–28, 2014.

[63] C Adler, A Denisov, E Garcia, M Murray, H Stroebele, and S White. The rhic zero degree calorimeters. *Nuclear Instruments and Methods in Physics Research Section A: Accelerators, Spectrometers, Detectors and Associated Equipment*, 470(3):488–499, September 2001.

[64] F.S. Bieser *et al.* The star trigger. *Nuclear Instruments and Methods in Physics Research Section A: Accelerators, Spectrometers, Detectors and Associated Equipment*, 499(2):766–777, 2003. The Relativistic Heavy Ion Collider Project: RHIC and its Detectors.

[65] L. Adamczyk and all. Single spin asymmetry an in polarized proton–proton elastic scattering at s=200 gev. *Physics Letters B*, 719(1):62–69, 2013.

[66] C. J. Dilks. *Longitudinal double-spin asymmetry of forward neutral pions from $\sqrt{s}$ = 510 GeV polarized proton-proton collisions at STAR.* PhD thesis, Penn State University, 2018.

[67] S. Bultmann et al. The PP2PP experiment at RHIC: Silicon detectors installed in Roman Pots for forward proton detection close to the beam. *Nucl. Instrum. Meth. A*, 535:415–420, 2004.

[68] J. Adam and all (The STAR collaboration). Measurement of the central exclusive production of charged particle pairs in proton-proton collisions at $$ \sqrt{s} $$= 200 gev with the star detector at rhic. *Journal of High Energy Physics*, 2020(7):178, 2020.

[69] T. Zimmerman, M. Sarraj, R. Yarema, I. Kipnis, S. Kleinfelder, L. Luo, and O. Milgrome. The svx2 readout chip [si strip detector]. *IEEE Transactions on Nuclear Science*, 42(4):803–807, 1995.

[70] J. Adam and all. Results on total and elastic cross sections in proton–proton collisions at s=200 gev. *Physics Letters B*, 808:135663, 2020.

[71] M. I. Abdulhamid et al. Results on elastic cross sections in proton–proton collisions at s=510 GeV with the STAR detector at RHIC. *Phys. Lett. B*, 852:138601, 2024.

[72] Joanna Kiryluk and STAR Collaboration. Relative luminosity measurement in star and implications for spin asymmetry determinations. *AIP Conference Proceedings*, 675(1):424–428, 07 2003.

[73] C. A. Whitten. The beam-beam counter: A local polarimeter at STAR. *AIP Conf. Proc.*, 980(1):390–396, 2008.

[74] Chong Kim. New fms calibration, 2019.

[75] Minghui Zhao. Run17 fms calibration note, 2021.

[76] Gavin P. Salam. Towards jetography. *The European Physical Journal C*, 67(3–4):637–686, May 2010.

[77] Z. Zhu. *Measurement of Transverse Single Spin Asymmetry for π^0 at Forward Direction in 200 and 500 GeV Polarized Proton-Proton Collisions at RHIC-STAR*. PhD thesis, Shandong University, 2019.

[78] Matteo Cacciari, Gavin P. Salam, and Gregory Soyez. Fastjet user manual: (for version 3.0.2). *The European Physical Journal C*, 72(3), March 2012.

[79] B. Abelev and all. Charged jet cross sections and properties in proton-proton collisions at $\sqrt{s} = 7$ TeV. *Phys. Rev. D*, 91:112012, Jun 2015.

[80] Torbjörn Sjöstrand, Stephen Mrenna, and Peter Skands. Pythia 6.4 physics and manual. *Journal of High Energy Physics*, 2006(05):026–026, May 2006.

[81] Peter Z. Skands. Tuning monte carlo generators: The perugia tunes. *Physical Review D*, 82(7), October 2010.

[82] R. Brun, F. Bruyant, M. Maire, A. C. McPherson, and P. Zanarini. GEANT3. 9 1987.

[83] Roger Barlow. Systematic errors: Facts and fictions. In *Conference on Advanced Statistical Techniques in Particle Physics*, pages 134–144, 7 2002.

[84] Run 15 polarization. `https://wiki.bnl.gov/rhicspin/Run_15_polarization`.

[85] Run 17 polarization. `https://wiki.bnl.gov/rhicspin/Run_17_polarization`.

[86] W. B. Schmidke. Rhic polarization for runs 9–17. Technical Report BNL-209057-2018-TECH, Brookhaven National Laboratory, 2018.

[87] An example calculation for the fill-to-fill uncertainty for a star analysis. `https://wiki.bnl.gov/rhicspin/upload/1/1c/ExampleFillToFill.pdf`.

[88] Torbjörn Sjöstrand, Stefan Ask, Jesper R. Christiansen, Richard Corke, Nishita Desai, Philip Ilten, Stephen Mrenna, Stefan Prestel, Christine O. Rasmussen, and Peter Z. Skands. An introduction to pythia 8.2. *Computer Physics Communications*, 191:159–177, June 2015.

[89] Leszek Adamczyk. Measurement of charged-particle production in single diffractive proton-proton collisions with the STAR detector. *SciPost Phys. Proc.*, page 081, 2022.

[90] K.H. Ackermann *et al.* Star detector overview. *Nuclear Instruments and Methods in Physics Research Section A: Accelerators, Spectrometers, Detectors and Associated Equipment*, 499(2):624–632, 2003. The Relativistic Heavy Ion Collider Project: RHIC and its Detectors.

[91] J.D. Brandenburg, Y. Chang, J. Dong, Y. He, Y. Hu, B. Huang, H. Huang, T. Huang, H. Li, M. Nie, R. Sharma, X. Sun, P. Tribedy, F. Videbæk, G. Visser, G. Wilks, P. Wang, G. Xie, G. Yan, Z. Ye, L. Yi, Y. Yang, S. Zhang, and Z. Zhang. The star forward silicon tracker. *Nuclear Instruments and Methods in Physics Research Section A: Accelerators, Spectrometers, Detectors and Associated Equipment*, 1072:170202, 2025.

[92] Y. Shi, C. Yang, and Q. Yang. The sTGC prototyping and performance test for the STAR forward upgrade. *JINST*, 15(09):C09021, 2020.

[93] Xin-Nian Wang and Miklos Gyulassy. Hijing: A monte carlo model for multiple jet production in p p, p a and a a collisions. *Physical Review D*, 44:3501–3516, 1991.

[94] S. Navas et al. Review of particle physics. *Phys. Rev. D*, 110(3):030001, 2024.

Appendix A

π^0 Reconstruction for STAR Forward Upgrade Electromagnetic Calorimeter

A.1 Introduction

The STAR Forward Upgrade program is motivated by studies of the cold QCD physics in the very high or low regions of Bjorken x, as well as explorations of the initial state of the heavy-ion collisions [24]. The STAR Forward Upgrade program includes the Forward Calorimeter System (FCS) and the Forward Tracking System (FTS). The FCS consists of the Electromagnetic Calorimeter (ECal) and the Hadronic Calorimeter (HCal). The FTS includes the Forward Silicon Tracker (FST) [91] and the small-strip Thin Gap Chambers (sTGC) [92].

The STAR FCS ECal is a Lead (Pb) / Scintillator (Si) sampling calorimeter, located about 738 cm west of the STAR interaction point. The full system is divided into two halves, placed symmetrically on the north and south sides of the beam pipe. Each half contains 748 towers, arranged in 34 rows by 22 columns, with each tower approximately about 5.5 cm in width. The calorimeter depth is approximately 18 radiation lengths, ensuring that incident photons deposit their full energy. The readout is provided by Silicon Photomultipliers (SiPMs). The energy of each tower is calculated from the integrated ADC signal within the event time window, scaled by a gain factor, which is a central focus of the studies presented in this chapter.

This chapter discusses both the prototype FCS ECal and the full FCS ECal, to which the author has made significant contributions. The prototype FCS ECal was built and tested in 2019. The gain factor was studied initially using data collected with the prototype FCS ECal. The full FCS ECal was constructed in early 2021. Then, the commissioning of the FCS ECal was completed in mid-2021. The FCS ECal began taking data in 2022 in the STAR Run 22 period. Methods for calibration are presented in detail in this chapter.

A.2 Gain Factor Study for the Prototype FCS ECal

The prototype FCS ECal was installed in 2019 and collected data from Au+Au collisions at $\sqrt{s} = 200$ GeV. This prototype detector only consist of 64 towers, arranged in 8 rows by 8 columns, with the minimum bias trigger applied.

The gain factor study is performed by comparing the data-taking and simulation results. The initial gain factor for the data taking is set to 0.02 GeV. The Heavy Ion

Jet Interaction Generator (HIJING) [93] is applied for the simulation. Energy spectra for all the prototype FCS ECal towers are plotted for both the data samples and the simulation samples. Then, the exponential function is fitted to each energy spectrum, and the decay rate from the exponential function is recorded accordingly for both the data and the simulation. Then, the corrected gain factor is calculated based on the ratio of the decay rate obtained from the data and the simulation, as shown in Eq. A.1. After the calculation, the corrected gain factor is 0.00086 GeV.

$$corrected\,gain\,factor = \frac{decay\,rate\,for\,data}{decay\,rate\,for\,simulation} \times 0.02\,GeV \tag{A.1}$$

After that, the corrected gain factor is used for the data for the π^0 reconstruction study. The π^0 decays to two photons with the branch fraction of more than 98% [94]. Two photons are used to reconstruct the π^0 meson. The FCS cluster is used as a photon candidate, where the concept of the FCS cluster is similar to that of the FMS cluster, as detailed in [77]. The event selection criteria are listed as follows:

- Each cluster energy $E_!$ $(E_2) > 1$ GeV
- The energy asymmetry $Z_{\gamma\gamma} = \frac{|E_! - E_2|}{E_! + E_2} < 0.7$

E_1 and E_2 represent the energy of the two FCS clusters as a pair. Furthermore, only the events with the number of hits in Time Of Flight (TOF) less than the threshold are accepted. For each accepted event, only the pair of FCS clusters with the highest sum of cluster energy is selected for the π^0 reconstruction. The invariant mass of the selected

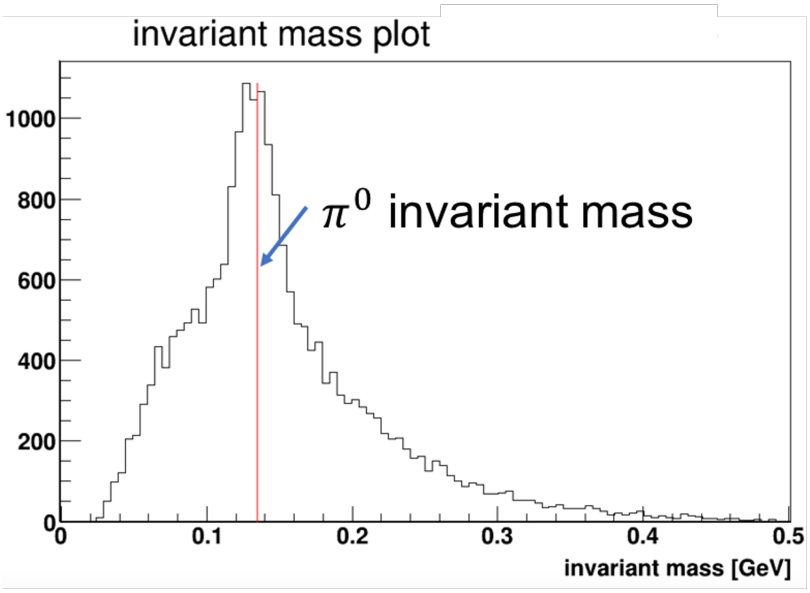

Figure A.1: Invariant mass plot for the data taken with the prototype FCS ECal. The vertical red line indicates the position of the π^0 invariant mass.

FCS cluster pair is calculated. Figure A.1 shows the invariant mass plot for all events in the data. It shows that the invariant mass peak is right at the π^0 invariant mass.

A.3 Calibration for the Full FCS ECal

Accurate calibration of the FCS ECal is crucial for extracting reliable physics results during data-taking periods. The primary method of calibration is based on π^0 reconstruction.

Photon candidates are identified from FCS clusters, which are then used in the π^0 reconstruction. The energy deposited in each tower is defined as the sum of ADC values within the event time window, multiplied by a fixed gain and a tower-dependent gain correction factor. With the large sample size of the dataset, it is possible to determine

the gain factor for every tower, thereby providing a precise conversion between ADC values and deposited energy. Initially, this tower-dependent gain correction factors are set to 1.

The π^0 reconstruction is performed for the entire dataset using event selection criteria mentioned in the Chpt. A.2. After selecting the only FCS cluster pair for the event, the tower with the highest energy within the cluster (highest energy tower) is found. The invariant mass of the cluster pair is then filled into the invariant mass spectrum associated with the highest energy tower. Then, a Gaussian function is used to fit the signal peak for each tower's invariant mass spectrum, while the background is modeled with a power-law function multiplied by an exponential. The mean of the Gaussian fit provides the invariant mass peak position for that tower. An example of such a distribution, including both signal and background fits, is shown in Fig. A.2.

After obtaining the invariant mass peak for each tower, a quality check is performed evaluate both the peak position and the quality of the fit. The results are summarized in a tower status plot, an example of which is shown in Fig. A.3. In this plot, the tower with red indicates the invariant mass peak is within 10% different from π^0 invariant mass. The tower with yellow indicates the invariant mass peak is between 10% and 33% different from π^0 invariant mass. The tower with green color indicates either the invariant mass peak is more than 33% different from π^0 invariant mass or the width of the invariant mass peak is higher than 0.07. The tower with blue color indicates that the entries for the invariant mass spectrum for the tower are less than minimum entry requirement. Only the tower with invariant mass peak within 33% different from π^0 invariant mass and the number of entries for the corresponding tower invariant mass spectrum more than the minimum entry

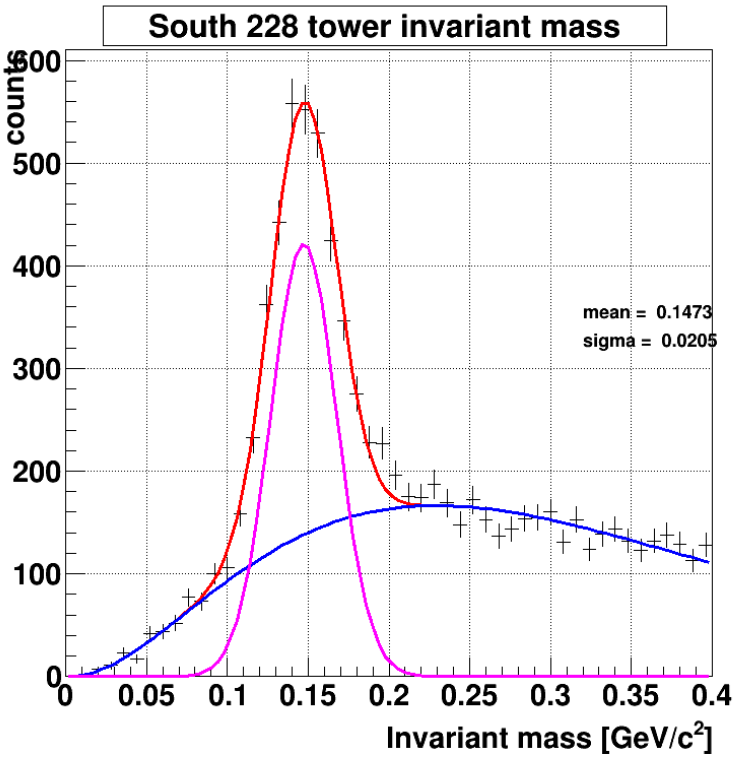

Figure A.2: Example of the tower invariant mass spectrum. The black points are the invariant mass spectrum. The magenta curve is the fit for the signal peak. The blue curve is the fit for the background. The red curve is the overall fit.

requirement, corresponding to the tower with either red or yellow color in the tower status plot, proceeds to calculate the corrected gain correction factor using Eq. A.2. The gain correction factor for the tower with other statuses remains unchanged.

$$new\ gain\ correction = original\ gain\ correction \times \frac{\pi^0\ invariant\ mass}{invariant\ mass\ peak} \tag{A.2}$$

The new gain correction for each tower is then applied, and the π^0 reconstruction procedure is repeated. Each iteration produces a new set of gain correction values. Typically, after two to three iterations, most towers converge such that their reconstructed invariant mass peaks lie close to the π^0 invariant mass. The left panel of Fig. A.3 shows the example of the invariant mass peak status plot before the π^0 reconstruction iteration. It shows that invariant pass peaks for couples of FCS ECal towers are away from the π^0 invariant mass. The right panel of Fig. A.3 shows the example of the invariant mass peak status plot after two iterations of π^0 reconstruction with the same dataset. It shows that the invariant mass peak for most of the towers is close to the π^0 invariant mass within acceptance, indicating successful calibration convergence.

Furthermore, the invariant mass plot for all di-photon pairs passing the event selection is prepared before the π^0 reconstruction iteration (the left panel of Fig. A.4) and after the π^0 reconstruction iteration (the right panel of Fig. A.4). With the π^0 reconstruction iteration, it is expected to see that the invariant mass peak is closer and matches with π^0 invariant mass. These results demonstrate the successful calibration using the π^0 reconstruction with iteration.

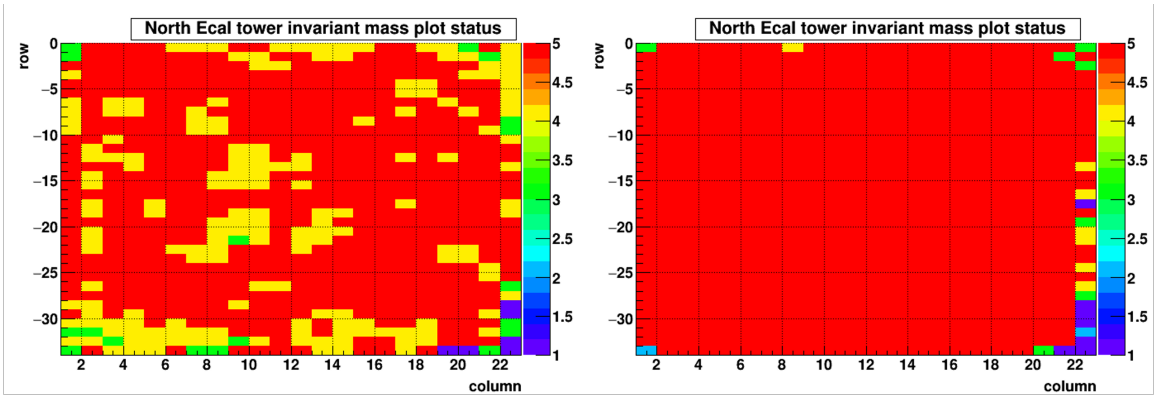

Figure A.3: Example of the invariant mass peak status plot for the north side FCS ECal tower before the π^0 reconstruction iteration (left) and after the π^0 reconstruction iteration for two iterations (right).

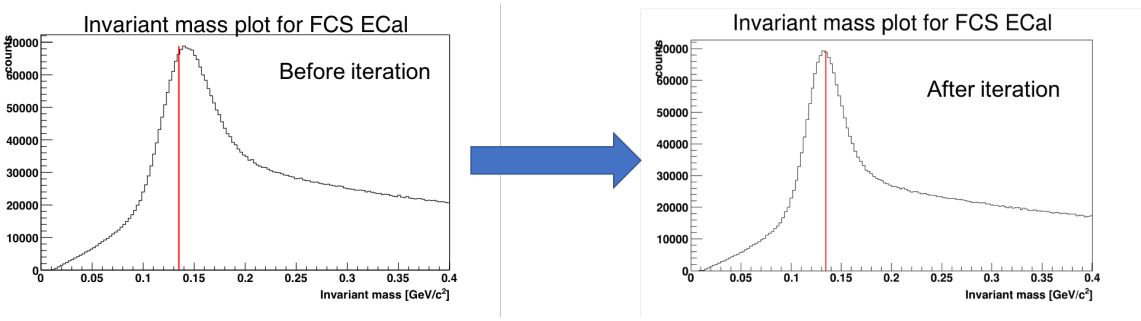

Figure A.4: Invariant mass plot before π^0 reconstruction iteration (left) and after (right) π^0 reconstruction iteration for two iterations.

The calibration using the π^0 reconstruction iteration has been applied successfully to the dataset for proton-proton collisions in the Run 22 (2022) and the Run 24 (2024).